Title
A Multidirectional Tribo-System: Wear of UHMWPE under Sliding, Rolling, and Rotation

Author
Patten, Elias Wolfgang

Publication Date
2012

Peer reviewed|Thesis/dissertation

A Multidirectional Tribo-System: Wear of UHMWPE under Sliding, Rolling, and Rotation

By

Elias Wolfgang Patten

A dissertation submitted in partial satisfaction of the

requirements for the degree of

Doctor of Philosophy

in

Engineering-Mechanical Engineering

in the

Graduate Division

of the

University of California, Berkeley

Committee in charge:

Professor Lisa A. Pruitt, Chair
Professor Kyriakos Komvopoulos
Professor Mohammad R. K. Mofrad

Spring 2012

A Multidirectional Tribo-System: Wear of UHMWPE under Sliding, Rolling, and Rotation

by Elias Wolfgang Patten

For Mi Morena,

you are the light within my soul

Abstract

A Multidirectional Tribo-System:
Wear of UHMWPE under Sliding, Rolling, and Rotation

by

Elias Wolfgang Patten

Doctor of Philosophy in Engineering-Mechanical Engineering
University of California, Berkeley
Professor Lisa A. Pruitt, Chair

Total knee replacements (TKR) have become a successful surgical procedure for addressing end-stage osteoarthritis, with ultra-high molecular weight polyethylene and cobalt chrome alloy (UHMWPE/Co-Cr) serving as the bearing materials of choice for decades. However, more than 10% of TKRs fail and require revision surgery. The predominant challenge with UHMWPE is the particulate debris generated through wear-mediated processes; wear debris from the UHMWPE tibial bearing surface leading to loosening is still the main cause for post-fifth-year revisions. UHMWPE wear in hip arthroplasty has been linked to microstructural evolution at the surface from multidirectional sliding in the hip joint but little is known about how the microstructure responds to clinically relevant sliding conditions in the knee. This is likely because wear tests are typically performed under basic motion parameters with simplified geometry (pin-on-disk tests) while the knee has more complex kinematics: it is neither a ball-and-socket joint nor a simple hinge joint, but has 2D sliding, rolling/slip motion, and rotation. There is also disagreement over how to best quantify cross-shear and how to model how much wear it will cause. A custom multidirectional tribo-system was used to investigate the individual and combined effects of the different motions in TKR: 2D sliding, rolling, and rotation, for a total of eight separate kinematic conditions. The trends in wear rates and wear factors for these different motions were compared with many different definitions for magnitudes and ratios of cross-shear. Additionally, the wear surfaces were examined for wear mechanism and the microstructural changes in lamellae orientation for the different motions were analyzed.

To mimic the tribological conditions of a condyle in a TKR, polished Co-Cr spheres were articulated against flat, smooth UHMWPE disks with physiologically relevant loading, speed, and lubrication conditions. The motion parameters were selected based on the lowest and highest reasonable amounts of cross-shear that each motion type would generate during a realistic gait cycle: a reciprocating line or a “figure 8” with a 15° crossing angle, no rolling or a 0.4 slide-to-roll ratio, and no rotation or a 1°/mm of rotation. The amount of wear was measured with optical profilometry of the cross-section at the middle of the wear scar, after allowing for a resting period for the material creep to recover. To calculate the amount of cross-shear at this cross-

section, the sliding interface was simulated with a computer Matlab model. Multiple definitions of cross-shear were used, including the traditional, cycle-based approaches and newer, memory-based approaches. The wear surfaces were examined using optical microscopy and scanning electron microscopy (SEM). The lamellar microstructure at the wear surface and below the wear surface was examined using an oxidizing etch to remove the amorphous phase. The remaining lamellae were imaged using SEM and their orientations and alignment was quantified using an image analysis code.

Wear factors were between 0.3 and 8.7 $\frac{\mu m^2}{Nm/mm}$. The higher values corresponded to increasing motion complexity and cross-shear, with the "figure 8" sliding path having the greatest effect. Volumetric wear rates correlated linearly with the total amount of cross-shear, while wear factors correlated linearly with ratios of cross-shear. The best predictors of the wear factor were the normalized crossing intensity and normalized, memory-based cross-shear ratios, with R^2 values of 0.98 and 0.97, although many of the cross-shear ratios also had a good linear fits with wear factor. The kinematic parameters in this experiment did not differentiate the various cross-shear parameters enough to conclusively determine which are most appropriate, although some have a stronger theoretical foundation than others. SEM analysis of the wear scar surface revealed slight scratching and instances of rippling and surface cracking perpendicular to the primary sliding directions. These are consistent with abrasive wear, plastic flow and adhesive wear, and fatigue wear mechanisms reported in other *in vitro* and *in vivo* wear studies. The orientations of the lamellae at the wear surfaces were not discernibly different from the lamellae of an unworn section of the disk surface. Similarly, the near-surface regions of the disk cross-section were not discernibly different from the subsurface regions. Previous studies have demonstrated orientation of the microstructure during wear using transmission electron microscopy, X-ray scattering, and Fourier transform infrared spectroscopy techniques, and such methods may be necessary for texture characterization.

These results demonstrate that knee kinematics have a significant effect on the cross-shear and wear of UHMWPE and should not be neglected when designing TKR. A better theoretical understanding of how kinematics contribute to wear can lead to better UHMWPE formulations, improved computer simulations of wear, and optimized TKR designs with longer life-spans.

Table of Contents

List of Figures

List of Tables

Acknowledgements

These past six years would not have been as enjoyable, as educational, as memorable, or even possible without the support of many, many people and I would like to express my deepest gratitude and appreciation. Specifically, to the members of dissertation and qual committees: first and foremost, Lisa Pruitt for her mentorship, encouragement, and support in research, teaching, and personal and professional development – you were more than just a research advisor and helped me develop to my fullest potential; Tony Keaveney for instilling a passion for technical communication and a foundation of critical thinking about research; Kyriakos Komvopoulos for his tribology expertise; Mike Ries for providing a clinical perspective and his medical expertise, as well as important case studies; Mohammed Mofrad for serving as the outside reader on my dissertation; and Richard Norgaard for expanding my horizons into energy and environmental economics. The many other professors and collaborators I've worked with: Doug Van Citters for his critical insight and expertise about tribology in orthopaedics; George Anwar for his willingness to provide his LabVIEW expertise; Tom Norris and Steve Gunther for their clinical expertise and collaboration on retrieval studies; Robert Full and everyone at CiBER for the excellent interdisciplinary training and experience and for inspiring me to ask the critical questions and always keep the big picture in mind; and the research group at Clemson for their perspective and collaboration. The expertise, patience, and guidance of all the ME staff: Elvis would just be a pile of metal without the design feedback and machining guidance of everyone in the student machine shop, especially Mic and Gordon; the only practical experience students would have with aerodynamics would be sticking their hand out the car window if it had not been for the help of everyone in the Hesse shop (Scott, Mike, Alex, and Pete) when building the wind tunnel; Tom and Rene for their help with everything computer and electrical; and of course everyone in the student services offices.

The Medical Polymer Group would not be the great place to work that it is if it weren't for the awesome lab mates: Thanks to Sheryl, Jevan, and the other graduate students who were here when I first started for welcoming into the lab; Matt Carney for teaching me so much about design and machining and all the hard work and attention to detail and presentation on our Master's project; Sara Atwood for her leadership, mentorship, and inspiring dedication; and to Farzana and Cynthia for the energy and great attitudes they bring into lab – I leave knowing the lab is in great hands. I would still have years to go if it weren't for the hard work and dedication of the many undergraduate researchers that have helped me build Elvis and run tests: Mike, Perry, Tim, Robyn, AJ, Matt, and Nolan. And thanks also to all the other undergraduates I've had the opportunity to mentor and work with on other MPG projects: Ingrid, Cynthia, Salar, Amir, Iris, Nicole, RJ, Amelia, Erin, JiHye, Austin, Raymond, Suzanne, Lila, Carol, Jennifer, and Andrew. It's been a pleasure and an honor to work with all you and call MPG my second home.

Most of all a special thank you to my friends and family: all my friends from WSU (go Cougs!) and Berkeley (go Bears!) for making these past 11 years of higher education a great

experience; my dad for being an excellent role model for work ethic, self-improvement, and interpersonal skills – the first academic research talks I went to were when I was 10 years old, standing in the back of the room as he presented the latest in pesticides and crop management to the farmers for the field days at the cranberry research center; my mom for instilling a DIY attitude, mechanical knack, and attention to resource conservation; my sisters for their great energy and keeping me in line; and my wife for her unwavering support and commitment, endless patience and understanding, the warm smiles and enduring love that brighten my day, and for walking with me when I could no longer run and carrying me when I could no longer walk–thank you for being my co-pilot on this spaceship called Earth.

Chapter 1: Introduction

1.1 - Background

Total joint replacements

The natural synovial joint, such as the knee, is an intricate and remarkable system, capable of providing support while loaded with forces several times body weight and allowing movement with low friction for more than a hundred million walking cycles. Unfortunately, it does not always function perfectly and many people, mostly elderly, suffer from joint pain and loss of functionality due to osteoarthritis and other diseases. To alleviate these ailments, total joint arthroplasties (TJA) have become increasingly prevalent, especially for the knee – 750,000 primary total knee arthroplasty (TKA) surgeries are predicted to be performed this year (2012) in the US (Kurtz, Ong, Lau, et al. 2007). This number is expected to continue to increase as the baby boomer population ages and people get their joints replaced at a younger age. Their high activity level also increases the importance of durable implants that can last for the remainder of the patient's life.

Modern TJAs, such as what is used in the knee, are typically composed of a cobalt-chrome (CoCr) metal bearing surface and an ultra-high-molecular-weight-polyethylene (UHMWPE) counter-bearing surface (Figure 1). In a total knee replacement (TKR), the CoCr bearing component is secured to the femur and the UHMWPE component is secured to the tibia through a mechanical locking mechanism with a titanium, or occasionally CoCr, tray. The patella bearing surface is typically also replaced with an UHMWPE component. During surgery, the surgeon removes the damaged cartilage tissue and shapes the underlying bone to provide a good fit with the mating components, which are secured in place either with bone cement (PMMA) or through bony in-growth with a porous titanium coating. The surgery usually takes about 1.5 hours and patients are typically walking with crutches within days and return to full activity in 4-6 weeks.

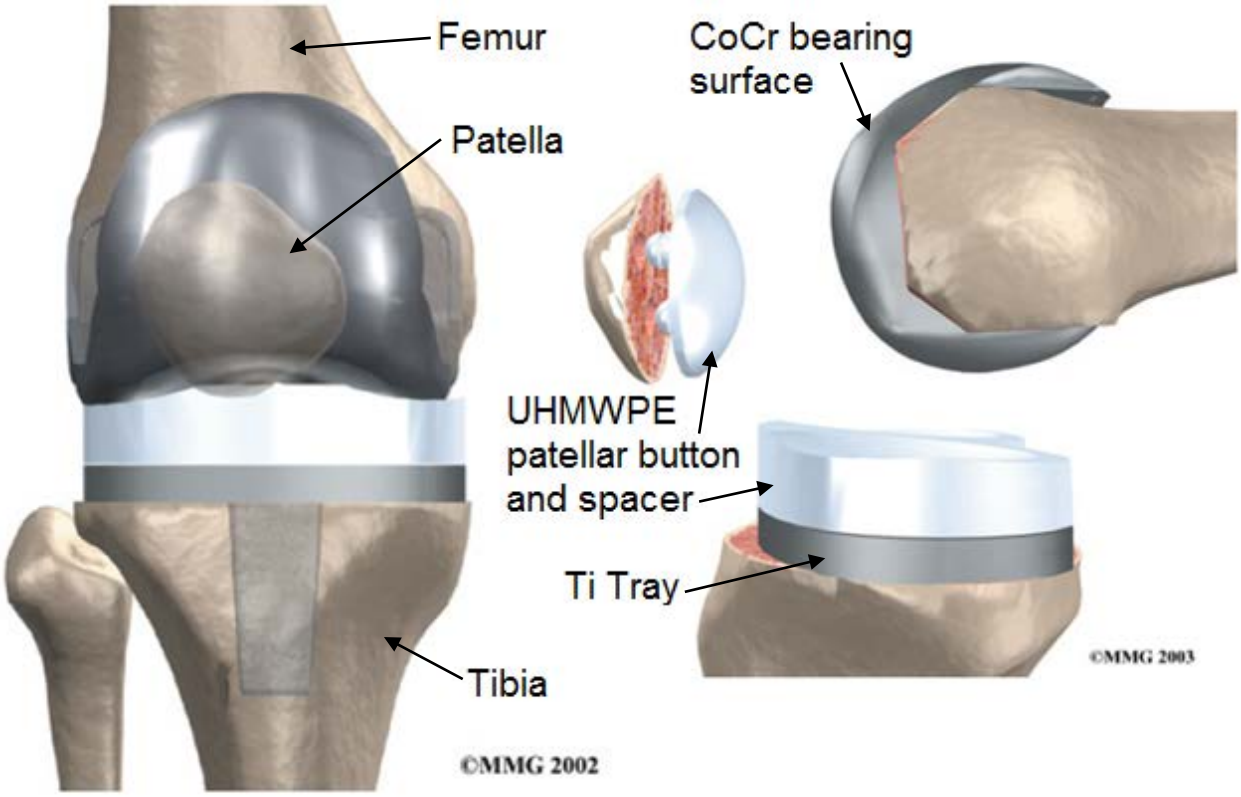

Figure 1: Components of a total knee replacement (eOrthopod 2003)

Although TJAs have become one of the most numerous and successful surgeries performed in the US, they are not yet as good as a healthy natural joint, and about 9% of TKAs will require revision surgeries (Kurtz, Ong, Lau, et al. 2007). These revision surgeries are projected to total almost three billion dollars in 2012 (Kurtz, Ong, Schmier, et al. 2007), not to mention the resulting decrease in patient outcomes, increase in mortality, and increase in hospital surgery burden. The largest single cause of TKR revision is infection (25%), but another common mode of failure is caused by UHMWPE wear particle generation (Bozic et al. 2010). These wear particles instigate osteolysis, an inflammatory response leading to bone resorption and implant loosening (Gupta et al. 2007). Bearing surface wear and the related periprosthetic osteolysis and mechanical loosening account for 24-30% of TKR revisions (Bozic et al. 2010; Gupta et al. 2007) and loosening is the main cause for revision after 5 years. Understanding the fundamental science behind this wear particle generation is crucial to improving UHMWPE performance, decreasing the number of revision procedures, and designing joint replacements that will allow younger and more active people to have successful joint replacements.

Ultra-high molecular weight polyethylene

Polyethylene $(C_2H_2)_n$ is simply many ethylene monomers (C_2H_2) that have been combined in an addition reaction to yield a long chain of covalently bonded carbon atoms with two hydrogen atoms attached to each carbon (Figure 2). Low-density polyethylene (LDPE) has short chains, around 2,000-3,000 carbon atoms long, and are commonly used in packaging

applications. High-density polyethylene (HDPE) is composed of longer chains, around 15,000-40,000 carbons long, more robust, and commonly used for milk jugs, children's toys, and even artificial tendons (Pruitt & Chakravartula 2011). Ultra-high molecular weight polyethylene (UHMWPE), on the other hand, can have 300,000-400,000 carbon atoms in a single, linear molecular chain and a molecular weight ranging from 4-6 million g/mol (Pruitt & Chakravartula 2011). This ultra-high chain length is achieved through a Ziegler-Natta catalyst reaction and is responsible for the high energetic toughness (Table 1) and resistance to wear and fatigue that has led to the ubiquity of UHMWPE in joint replacements.

A quick note on terminology: for this introduction chapter, the term "polyethylene" will be used to discuss this family of polymers as a whole, "UHMWPE" will be used for ultra-high molecular weight polyethylene in general, the terms "conventional" or "virgin" will be used with UHMWPE to refer to material that has not been crosslinked or has only received a small amount of crosslinking radiation for sterilization purposes, and "crosslinked" will be used with UHMWPE to refer to material that has been processed for additional crosslinking. For all following chapters, the term "polyethylene" will be used for easier readability and refer solely to UHMWPE.

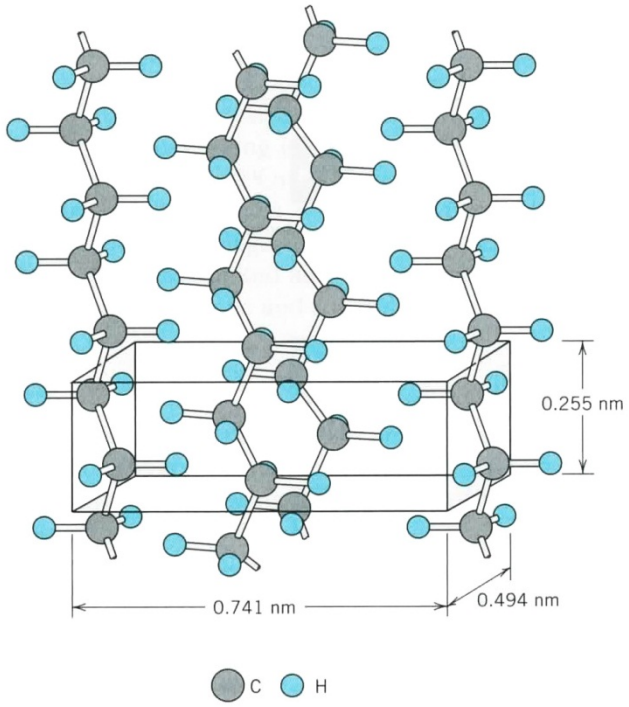

Figure 2: Chains of polyethylene in a unit cell of the crystalline region (Callister 2003).

UHMWPE is a semi-crystalline polymer, meaning these long molecular chains arrange themselves into crystalline and amorphous regions to form the bulk material (Figure 3A). UHMWPE is typically between 40 and 60% crystalline, although some high pressure processing techniques can reach a crystal volume fraction of up to 70%. In the crystalline regions, the polyethylene chains fold back and forth on themselves to form plate-like lamellae tens of nanometers (approximately 80 carbons) thick and several hundreds of nanometers long (Figure

3B, Figure 4). In the space between these lamellae the molecules are amorphous, with chains entangled around each other in no long-range order. Tie molecules have part of their chain in a crystalline region and part in the amorphous region. Tie molecules connect lamellae to each other and to the amorphous phase and play an important role in the plasticity of UHMWPE (Lin & Argon 1994).

Table 1: Minimum mechanical performance requirements of UHMWPE fabricated for surgical implants from type 2 resin (GUR 1050) according to ASTM Standard F648 (ASTM 2006).

Property	Requirements	Units
Density	827-944	kg/m^3
Tensile Strength (23°C)		
Ultimate	40	MPa
Yield	19	MPa
Elongation	340	%
Izod Impact Strength	73	kJ/m^2
Charpy Impact Strength	90	kJ/m^2

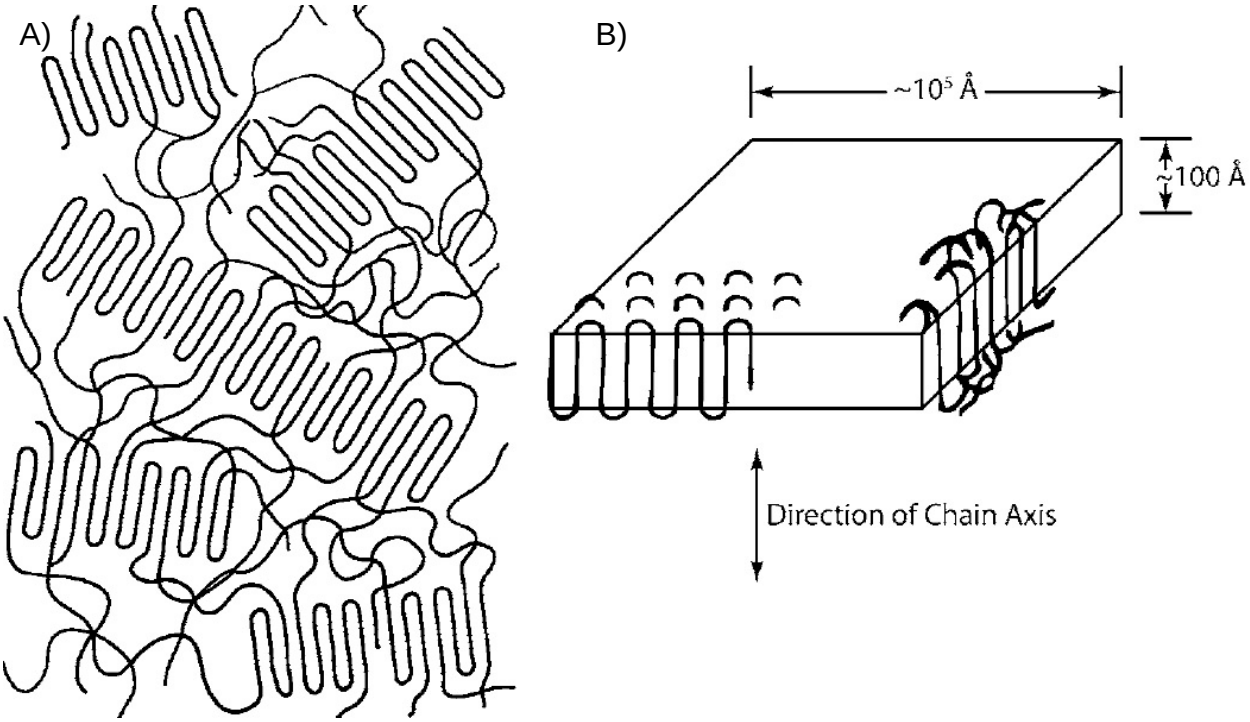

Figure 3: A) The microstructure of UHMWPE comprises crystalline and amorphous regions, with tie molecules connecting the two. B) A lamellae of the crystalline region with representative dimensions. The chain axis is aligned in the thickness direction. (Pruitt & Chakravartula 2011)

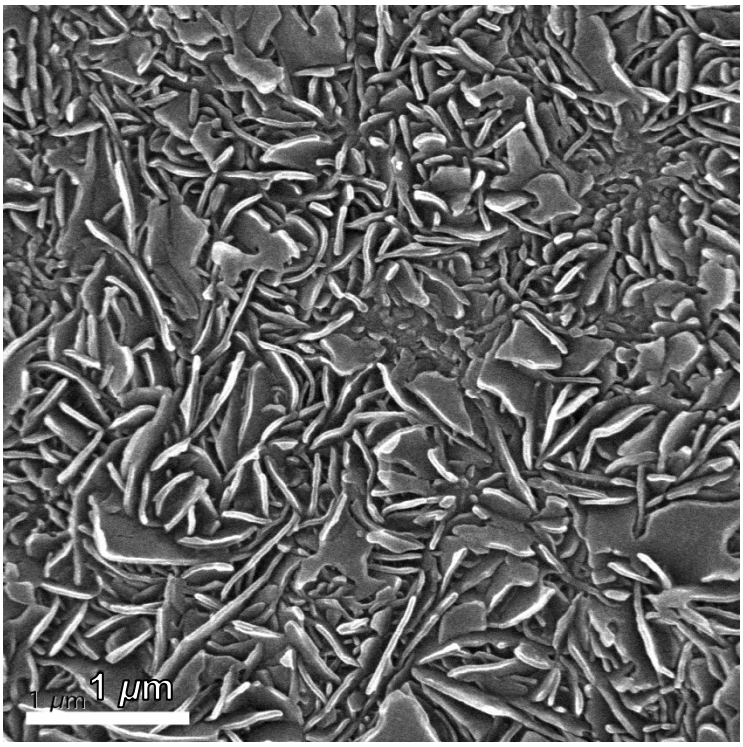

Figure 4: SEM micrograph showing crystalline lamellae of UHMWPE following removal of the amorphous region with an acidic etching procedure.

While the chains in the crystalline and amorphous regions are only bonded to each other with weak van der Waals forces, the backbone of the chain uses very strong covalent bonding. Under plastic deformation, the secondary bonds continuously break and reform as the primary chains in the crystalline and amorphous regions shear and rearrange themselves to take the majority of the load (Figure 5a-c, Figure 6) (A. Galeski et al. 1992; Oleinik 2003). At high levels of plastic strain, screw dislocations can initiate in the polymer lamellae and propagate through the crystalline structure, slowing breaking apart the lamellae (Figure 5d-e) (Séguéla 2002; Shadrake & Guiu 1979). However, recent studies have shown that UHMWPE lamellae do not reach this final stage of disintegration but rotate and bend into V-shapes to an approximate angle of 65° from the loading axis (Argon et al. 2005; Boontongkong et al. 1998; Oleinik 2003).

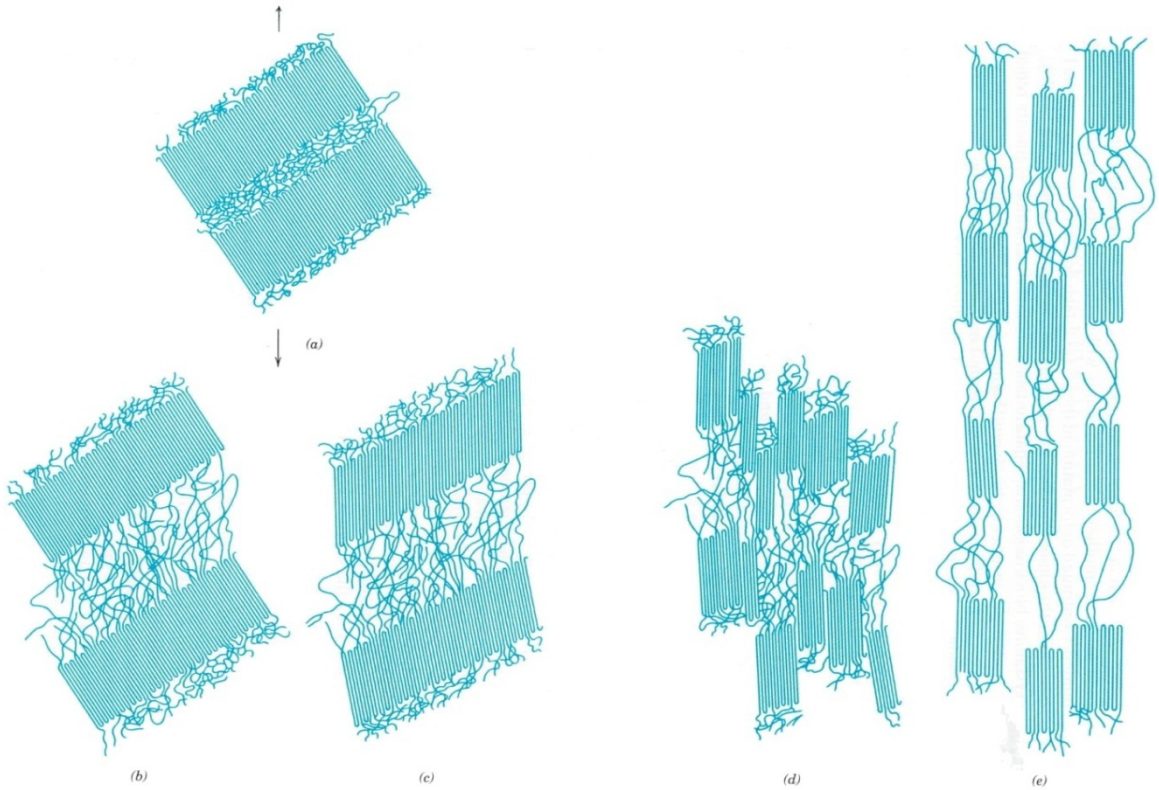

Figure 5: Stages in the deformation of a semicrystalline polymer. (a) Two adjacent chain-folded lamellae and interlamellar amorphous material before deformation. (b) Elongation of amorphous tie chains during the first stage of deformation. (c) Tilting of lamellar chain folds during the second stage. (d) Separation of crystalline block segments during the third stage. (e) Orientation of block segments and tie chains with the tensile axis in the final deformation stage. (Callister 2003)

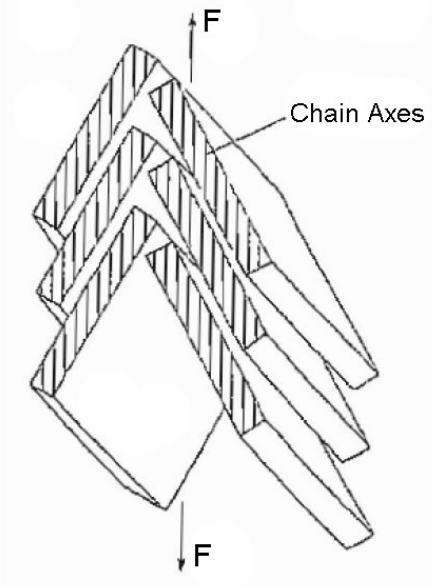

Figure 6: A sketch of the deformation process showing how both the lamellae and the chain axis in the lamellae shear and rotate to align with the loading direction. The lamellae stack and align with each other and reach a maximum alignment of about 65° from tensile force. (Oleinik 2003)

The evolution and alignment of the microstructure, also called texture development, gives UHMWPE its strain hardening abilities. It also leaves the material anisotropic and subject to strain softening in the direction opposite of loading. This is the foundation for the theories that explain UHMWPE's decreased wear resistance under multidirectional sliding, which will be discussed more in later sections.

Tribology of joint replacements

The millions of cycles of articulation that take place in a joint lead to wear (material removal) and damage (change in texture or appearance) of the bearing surfaces, and can ultimately lead to the failure of the implant and need for a revision surgery. Tribology is a complex topic and the intersection of many different fields: contact mechanics, materials science, fluid dynamics, surface physics, chemistry, biology, and others. Three main concepts that are important in studying tribology are wear mechanisms, surface roughness, and lubrication.

Wear of UHMWPE in joint replacements take place primarily through three wear mechanisms: adhesion, abrasion, and fatigue (Figure 7) (McKellop 2007). Adhesive wear occurs when small asperities in the two materials directly contact each other and the force of chemical adhesion is greater than the strength of weaker asperity, breaking it off and transferring it to the other bearing surface. Abrasive wear is when the asperities of harder material, either the metal or ceramic bearing surface or a 3rd-body particle, is physically pushed into the softer one and dragged across the bearing surface. This can remove material by shear or cutting, and damage the material by gouging and scratching. With fatigue wear, the contact stress and friction forces create a subsurface plastic shear stress and deformation. After many cycles of plastic deformation, cracks are generated below the surface and grow parallel to the surface, eventually meeting other cracks or reaching the surface and producing sheets of wear particles. (Kato & Adachi 2001; Pruitt & Chakravartula 2011; Suh 1977).

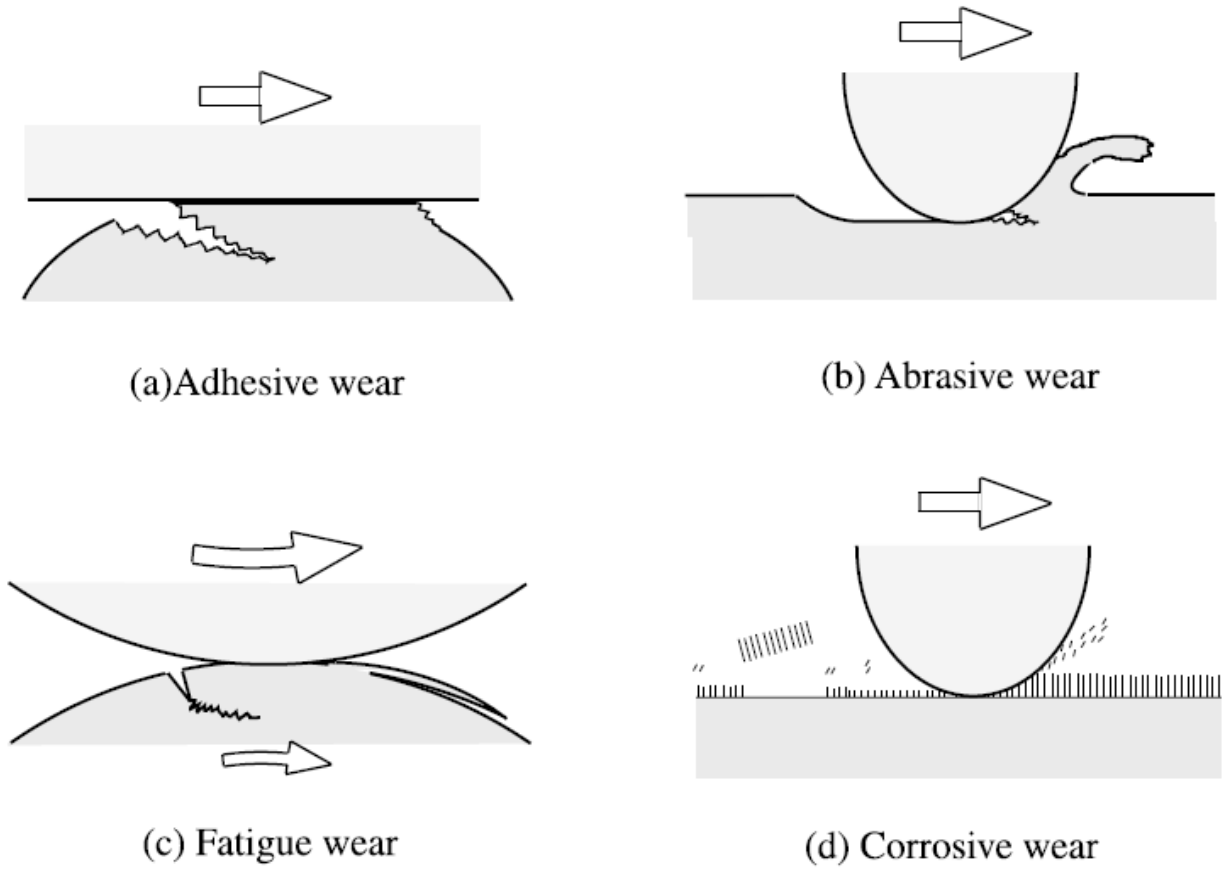

Figure 7: Four of the main wear mechanisms illustrated at the asperity level. Adhesive, abrasive, and fatigue wear are prominent in UHMWPE in joint replacements, while corrosive is generally only seen at metal-metal interfaces such as fretting on a Morse taper. (Kato & Adachi 2001)

The amount of wear debris generated by each of these wear mechanisms is highly dependent on the interaction of the asperities of surfaces, and so it is important to be able to measure the roughness of the surfaces used in wear studies. There are many parameters that can quantify different aspects of the roughness that can relate to the amplitude of the asperities, the spacing of the asperities, or both. Amplitude parameters are the simplest to describe and therefore the most common, and average surface roughness, R_a, is the simplest and most common amplitude parameter:

$$R_a = \frac{1}{L}\int_0^L |z(x) - \bar{z}|dx \,, \qquad \text{eq. 1}$$

where L is the length of the profile, $z(x)$ is the height along the profile, and $\bar{z}$ is the average height of the profile. Other amplitude parameters (Figure 8) can be height parameters, such as the maximum deviation from a mean surface (maximum peak height or valley depth), shape parameters, such as whether there are more peaks or more valleys (skew), and parameters used to make a bearing area curve, which describes what percentage of the surface is at a certain height. Spatial parameters describe how many peaks there are, such as summit density or the number of zero crossings, the distance between asperities, such as average wavelength or mean peak

spacing, and how quickly the surface fluctuates, such as in a autocorrelation analysis. Hybrid parameters are a function of both the spacing and the size of the asperities and include parameters such as the mean asperity slope and tip radius. (Bhushan 2001; Sherrington 1998; Hall et al. 1996) The reason for having so many different roughness parameters is the infinite number of variations of surface landscape; many different surface profiles can all have the same measurement of average roughness (R_a) yet be quite different in many other respects, which could lead to very different effects on wear.

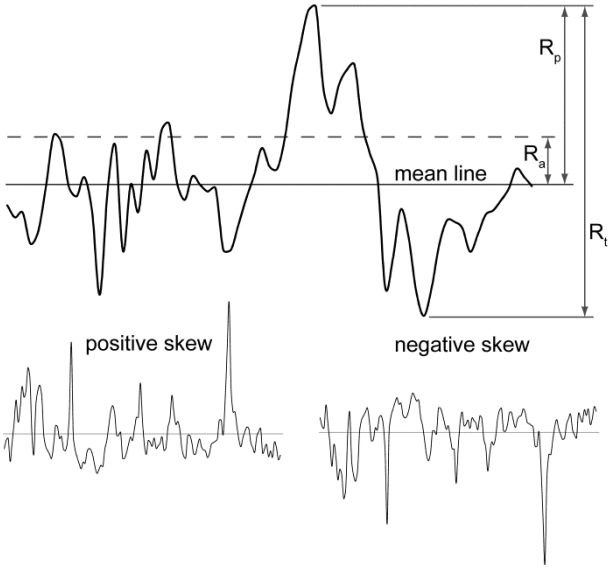

Figure 8: Schematic illustrations describing the roughness parameters used to describe the topography of the femoral head surface. Average roughness (R_a) is the average deviation from the average surface level. Total roughness (R_t) is the height difference between the highest peak and lowest valley within one sample. Peak height (R_p) is the highest point within one sample. Skew (R_{sk}) is a measure of how many peaks there are compared to valleys. (Patten et al. 2010)

How the surface roughness is measured is as important as the parameter used to quantify it. The most common methods are either mechanical or optical. For the mechanical method, a small stylus is lightly loaded against the measurement surface and then its vertical displacement is measured as it travels across the surface. There are many variations of optical methods but a common one is optical interferometry, which measures the interference fringe pattern of parallel light beams reflected off the surface to calculate what the surface topography is. For all methods, the filtering parameters and sample size must be carefully chosen to ensure that a relevant scale of roughness is measured (long length waviness vs. the short length variation within asperities). (Bhushan 2001)

Another factor that affects how the asperities interact is lubrication. Lubricating fluids can separate the two wear surfaces, decreasing direct asperity contacts and thus wear and friction. The level of asperity contact determines whether the surfaces are under boundary, mixed, elastohydrodynamic, or hydrodynamic lubrication. These different regimes of lubrication can be visualized with a Stribeck curve and depend on the lubricant viscosity, η, sliding velocity, v, and applied load, L (Figure 9). In joints, the load and sliding velocity (and hence viscosity, as

synovial fluid is a shear thinning fluid) varies throughout a walking cycle, and therefore the lubrication mechanisms in joints varies between boundary, mixed, and elastohydrodynamic modes (Neu et al. 2008).

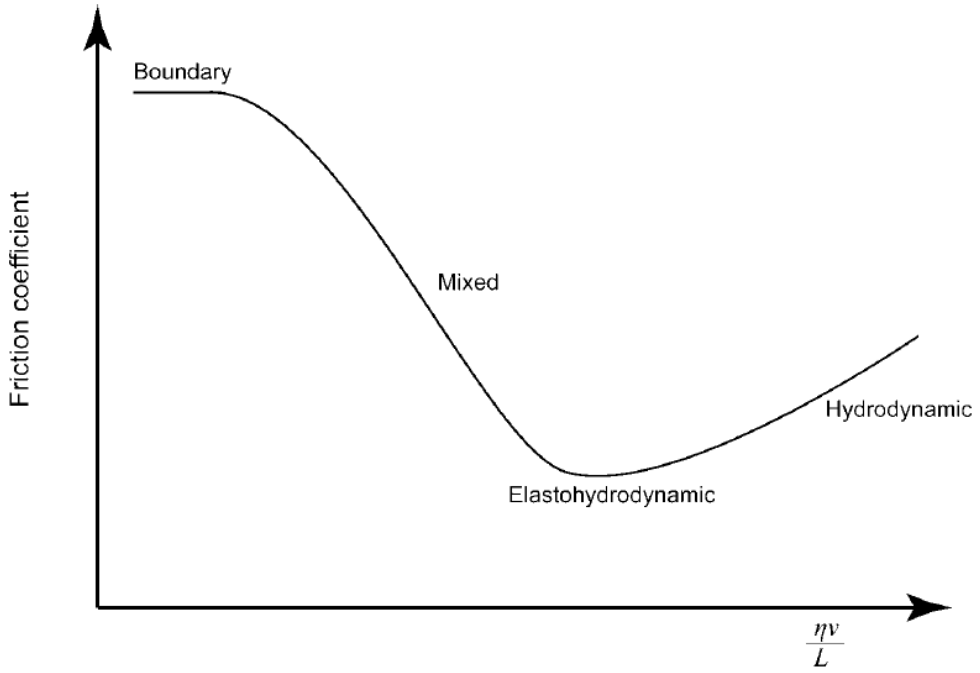

Figure 9: A Stribeck curve shows how the coefficient of friction varies in the different lubrication regimes as the asperity contact changes due to the lubricant viscosity, sliding velocity, and load. The film thickness and surface separation increases as the quantity on the x-axis (the Hersey number) increases, minimizing wear. (Pruitt & Chakravartula 2011)

The simplest way to quantify wear for a certain combination of wear mechanism, roughness, and lubrication regime is by using a wear rate that normalizes the volume, V, depth, δ, or cross-sectional area, A_w, of a wear scar by either the total sliding distance, s, or the number of cycles, N_c. For example:

$$\dot{V}_w = \frac{V}{s}, \qquad \text{eq. 2}$$

$$\dot{A}_w = \frac{A_w}{N_c}. \qquad \text{eq. 3}$$

These are best for comparing the absolute amount of wear under different scenarios, but it can't be easily generalized and applied to other situations. For this, the classic wear model, developed by F. Archard in 1953 (Archard 1953), characterized the wear between metal surfaces using a wear coefficient, k:

$$k = \frac{VH}{Ls}, \qquad \text{eq. 4}$$

where H is the hardness of the metal and L is the normal load. It is debatable whether this model is appropriate for UHMPWE (see section on *Other factors that affect wear of UHMWPE*), but a similar model is still commonly used in the literature. Since the hardness is not as consistent in

polymers as it is in metals, and is not a large factor in polymer wear, most researchers characterize the wear of UHMWPE in terms of a wear factor, k', based only on the wear volume, load, and total sliding distance. This wear factor can also be used to analyze the wear of a finite contact area, dA, within the larger wear surface. It is then in terms of the wear depth at that location, δ, and the local contact pressure, P:

$$k' = \frac{V}{Ls} = \frac{\delta\, dA}{P\, dA\, s} = \frac{\delta}{Ps}\,. \qquad \text{eq. 5}$$

The denominators in eq. 5 are also known as the tribological intensity, τ. For a varying load or complex motion, the total tribological intensity is calculated by integrating the load (or pressure for a differential element), multiplying by the magnitude of the instantaneous slip velocity vector, $\vec{v}$, for one cycle (with period, T), and then multiplying by the total number of cycles, N_c:

$$Ps \overset{\text{def}}{=} \tau = N_c \tau_c = N_c \int_0^T P|\vec{v}|\, dt\,. \qquad \text{eq. 6}$$

For certain types of wear paths, it is convenient to analyze the wear using the cross-section of the wear scar and put the parameters in eq. 5 in terms of per-unit-length of sliding distance in one cycle, x. To find the volume of material worn away per unit length, the profile of the wear scar is integrated to find the wear area, A_w. The tribological intensity is also integrated across the width of the wear scar, $2a$, to get the tribological intensity per unit length and cycle, τ_l. Plugging this into eq. 5:

$$k' = \frac{\int_{-a}^{a} \delta\, dw}{N_c \int_{-a}^{a}\int_0^T P|\vec{v}|\, dt\, dw} = \frac{A_w}{N_c \tau_l} \approx \dot{A}_w \Big/ \frac{L}{2a} s\,. \qquad \text{eq. 7}$$

The total wear volume would be found by multiplying this wear factor by the tribological intensity input per cycle, the sliding distance per cycle (if the wear factor is constant along the wear path), and the total number of cycles.

A quick note on units for a wear area based approach: the classic definition of wear rate is based on volume per distance or cycle ($\frac{\mu m^3}{m}$ or $\frac{\mu m^3}{cycle}$), whereas a cross-section wear scar analysis would use a per-unit-length-of-wear-track approach with the area ($\frac{\mu m^2}{m}$ or $\frac{\mu m^2}{cycle}$). Similarly for the tribological intensity, instead of load and sliding distance per cycle ($N\, m/cycle$) the units would be based on load per contact length or contact pressure times contact width (Nm/mm or *MPa*m*mm*). The wear factor based on an area approach can be found by extension, and when simplified yield the same units as a volume-based approach would:

$$[k] = \frac{\frac{\mu m^2}{cycle}}{N\frac{m}{cycle}/_{mm}} = \frac{\mu m^2}{Nm/_{mm}} = \frac{\mu m^3}{Nmm}\,. \qquad \text{eq. 8}$$

To make it clear which approach was used and to express results without needed scientific notation, these main units will be used throughout the report:

tribological intensity and frictional work: $\frac{Nmm}{mm}$

frictional power: $MPa\frac{mm}{s}$

wear rate: $\frac{\mu m^2}{cyc}$ or $\frac{mm^2}{Mcyc}$

wear factor: $\frac{\mu m^2}{Nm/mm}$

Studies showing that the wear rate is not linearly dependent on load (wear factor for UHMWPE is not a constant across all contact pressures) and is instead linearly dependent on apparent contact area, A_c, have led some researchers (Liu et al. 2011; Mazzucco & Spector 2003) to express wear performance using an area wear coefficient, C:

$$C = \frac{V}{A_c s}. \quad \text{eq. 9}$$

For more complex situations when wear is analyzed per-unit-length, the area wear coefficient is the average wear depth at the cross-section divided by the average total relative sliding distance:

$$C = \frac{\frac{1}{2a}\int_{-a}^{a} \delta \, dw}{\frac{1}{2a}N_c \int_{-a}^{a}\int_{0}^{T} |\vec{v}| \, dt \, dw}. \quad \text{eq. 10}$$

1.2 - State of the literature

Tribologically induced texture development of UHMWPE

Ultimately, wear is a function of the asperity loads and the stress state in the top layer of UHMWPE since it is these loads and this stress state which will deform material and break the primary and secondary bonds that lead to wear debris liberation. The mechanical behavior of a polymer and its response to loading is highly dependent on how the long chains in the material are arranged – whether they are oriented in long fibers parallel to the load, packed in crystals with a high density of secondary bonding, or randomly distributed in an amorphous network. Under high enough loads the chains can slide past each other and rearrange themselves. For UHMWPE especially, the history of the magnitude and orientation of the tribologically induced stress state can change the microstructure and lead to texture development, making the material either more or less resistant to wear, depending on the sliding directions.

The importance of multidirectional sliding on the wear of UHMWPE was first discovered in the mid-1990s (Bragdon et al. 1996; Wang, Polineni, et al. 1997). One of the first papers that developed the theory behind this effect looked at the role of orientation softening in wear by testing the strength of dogbone samples that had been plastically deformed (pre-stretched) either parallel or perpendicular to the sample axis (Wang, Sun, et al. 1997). Samples that had been pre-stretched parallel to their final direction of elongation had a 60-120% increase in rupture

strength, while samples that had been pre-stretched perpendicular to their final direction of elongation had a 30-60% *decrease* in rupture strength. This, combined with microstructure examination of the wear debris, led to the theory that sliding stresses will plastically deform the top layer of material and align the lamellae in the sliding direction. The rupture strength of the material in this direction increases, but perpendicular to this direction the material is now much weaker. Any sliding in this perpendicular direction will rupture fibrils and generate wear debris at a much higher rate than will sliding in the principal direction. Crosslinking the polyethylene chains has been shown to greatly reduce the amount of orientation that occurs. Details on crosslinking and a summary of its effect on other material properties will be discussed in the next section.

More evidence for the role of surface plastic deformation in the wear process was demonstrated by A. Edidin et al. in acetabular liners from joint simulator studies (Edidin et al. 1999) and in retrievals of crosslinked and non-crosslinked tibial inserts (Kurtz et al. 2000). Non-crosslinked and crosslinked UHMWPE acetabular liners were wear-tested in a standard hip joint simulator. After 3 million cycles the test was stopped and 65-nm-thick layers were sectioned parallel to the wear-surface of cores taken through the liner thickness. The sections were stained and then imaged using transmission electron microscopy (TEM) to observe the changes in microstructure. Clear alignment from plastic deformation was seen in the near-surface layer while random orientation was observed in the sub-surface layer. The depth of the near-surface layer was reported to be about 9 μm for non-crosslinked UHMWPE but only 4 μm for crosslinked UHMWPE, which corresponded to a significant decrease in wear rate (Figure 10). Lamellae alignment parallel to the sliding direction (and perpendicular to the wear surface) has also been shown in uni-directional pin-on-disk wear tests for a range of contact pressures and sliding velocities (Crane 1998). Further pin-on-disk studies have shown that the depth of alignment increases with contact pressure (Klapperich et al. 1999). Some studies report conflicting directions of alignment (Zhou et al. 2004; Davey et al. 2004).

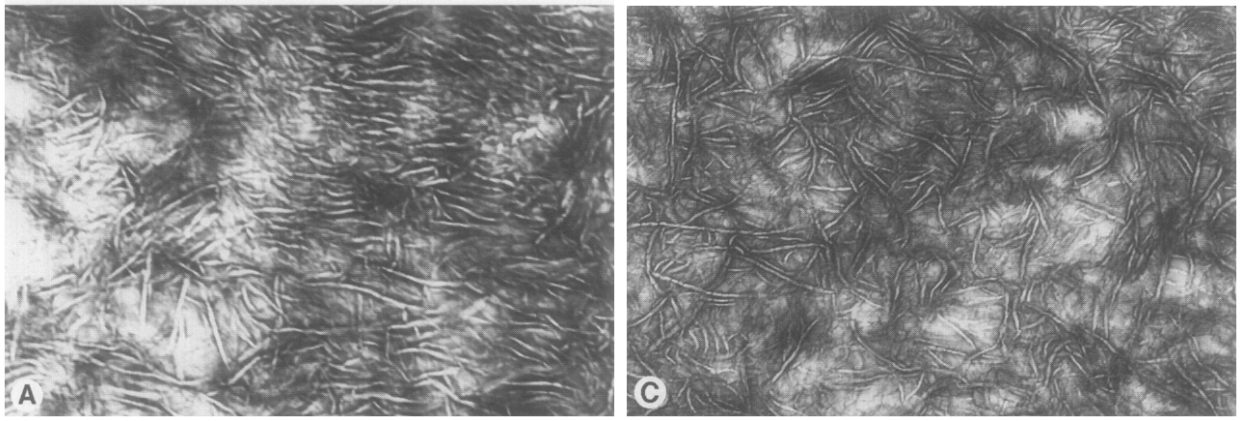

Figure 10: After wear testing of non-crosslinked UHMWPE, clear lamellae alignment was seen in TEM images of the near-surface layer (A: depth of 1.3 to 2.0 μm) while the lamellae in the subsurface regions were random and isotropic (C: depth of 9 μm). (Edidin et al. 1999)

More insight into the microstructure evolution was given by research performed by Zhou, who looked at the surface texture development of UHMWPE pins during reciprocating wear testing. SEM images of the wear surfaces displayed regularly spaced folds perpendicular to the sliding direction and a short, 1-minute permanganate etch of the wear surface revealed a greater amount of material etched away from the valley regions between the folds than from the folds themselves (Zhou & Komvopoulos 2005). Since the etchant preferentially removes the amorphous regions of the UHMWPE, these lamellae deficient regions hint at how the crystalline and amorphous regions deform and move under shear loading during wear. Lamellae group together in the folds as the amorphous regions diffuse downward, leaving a weaker near-surface layer that can more easily lead to delamination and debris generation (Figure 11).

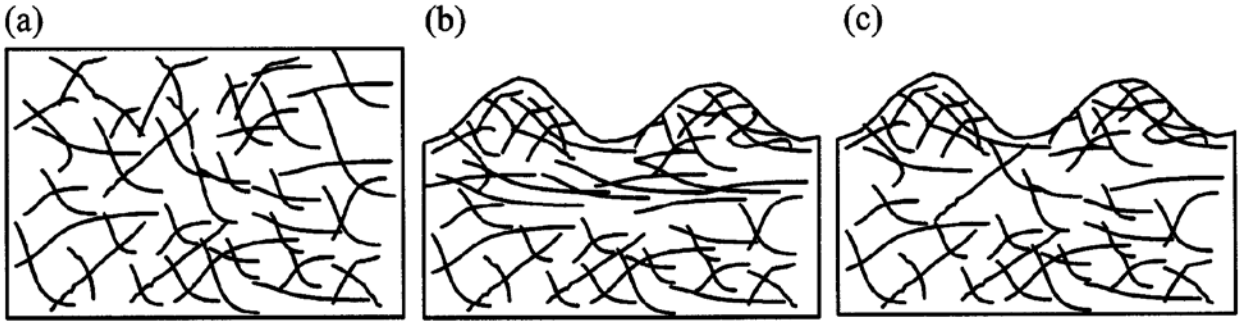

Figure 11: Schematic illustration of the deformation process leading to the formation of regularly spaced and parallel folds on UHMWPE sliding surfaces: (a) original microstructure with randomly distributed crystalline lamellae, (b) surface folding due to plastic shear and lamellae alignment adjacent to the surface, and (c) lamellae at the crests of folds revealed after etching the amorphous phase. (Zhou & Komvopoulos 2005)

Molecular orientation of UHMWPE can also be studied using X-rays. Sambasivan et al. tested non-crosslinked and crosslinked UHMWPE pins under unidirectional, reciprocating, and cross-shear sliding against CoCr disks and measured the resulting alignment of the carbon backbones near the surface (3-5 nm) of the material using near-edge X-ray-absorption spectroscopy. They found a greater amount of carbon-carbon bonds aligned in the sliding direction than perpendicular with the sliding direction. Also, the degree of alignment was found to be the greatest for unidirectional sliding and the least for cross-shear sliding. However, they do not explain the effect of this alignment on the actual microstructure. Since the carbon backbone is snaked back and forth within a crystal and is aligned perpendicular to the main plane of the lamellae, alignment due the crystalline regions would imply that the lamellae were aligned perpendicular to the sliding surface and perpendicular to the sliding direction. This is not what the previous studies have found, so the alignment here likely is either measuring the chains in the amorphous phase, or the shear stress has rotated the chains within the lamellae such that they are no longer perpendicular to the lamellar disk (Figure 6).

Crosslinked UHMWPE

Crosslinking UHMWPE significantly decreases the amount of alignment and plastic strain that occurs and this has led to the greatest advancement in decreasing the wear rate of joint

replacements. Gamma or e-beam radiation are commonly used to sterilize UHMWPE implants, typically between 25 and 40 kGy, and highly crosslink the material for increased wear resistance, typically at 100 kGy (Kurtz 2009). The radiation breaks off hydrogen side groups from the carbon backbone and generates free-radicals that can initiate direct covalent bonding between carbons in adjacent chains in the amorphous phases. These crosslinks limit the mobility of the chains, enhancing resistance to plastic flow (Yim et al. 1999; Ries & Pruitt 2005; McKellop, F. W. Shen, et al. 1999). The resulting wear rate can drop by more than an order of magnitude (Figure 12). Although crosslinking UHMWPE does decrease the total volume of wear debris, the sizes of the individual wear particles can be smaller and have a greater potential for osteolysis (Williams et al. 2007).

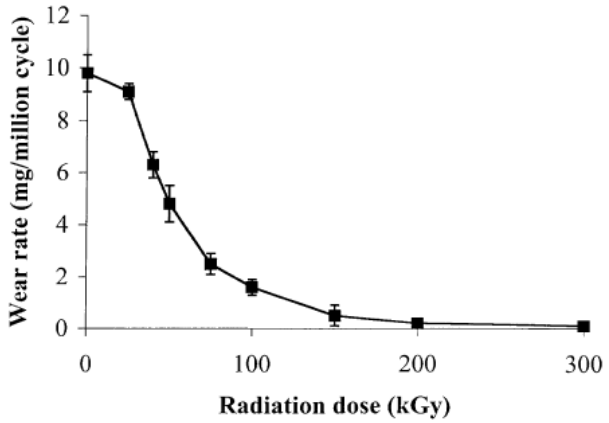

Figure 12: Wear rates of cold irradiated and subsequently melt-annealed UHMWPE pins on CoCr disks under bi-directional sliding and variable loading showing how wear rate can be significantly decreased by crosslinking (Muratoglu et al. 1999).

Crosslinking can leave UHMWPE with two important weaknesses: oxidation and decreased fatigue performance. Not all of the free-radicals generated during the radiation sterilization or crosslinking process will be extinguished by new covalent bonds and in the presence of oxygen they can lead to chain scission. This oxidative degradation decreases the ultra-high chain length that gives UHMWPE its excellent mechanical properties and greatly increases the risk of fracture and delamination wear (Premnath et al. 1996; J. H. Currier et al. 1998). Since it was discovered that gamma radiation in air was leading to increased failure rates, radiation treatments now only take place in a vacuum or inert environment and are now barrier packaged so they can be stored in an oxygen-free environment (Kurtz 2009). To ensure the free radicals have been fully annihilated, most UHMWPE implants are now also heat treated with either a sub-melt anneal or remelt process (Muratoglu, Bragdon, D. O. O'Connor, Jasty, et al. 2001; McKellop, F. W. Shen, et al. 1999; Jacobs et al. 2007). However, there still remain questions about long-term oxidation resistance of crosslinked UHMWPE *in vivo* (B. H. Currier et al. 2007). Additionally, crosslinking deceases UHMWPE's toughness and resistance to fatigue crack propagation (Pruitt 2005). Crosslinked UHMWPE that has been remelted can have even less resistance to fatigue crack propagation (Figure 13) because deceased mobility during

recrystallization results in smaller lamellae sizes (Atwood et al. 2011), and recent case studies have reported fatigue fractures in crosslinked acetabular liners (Furmanski et al. 2009).

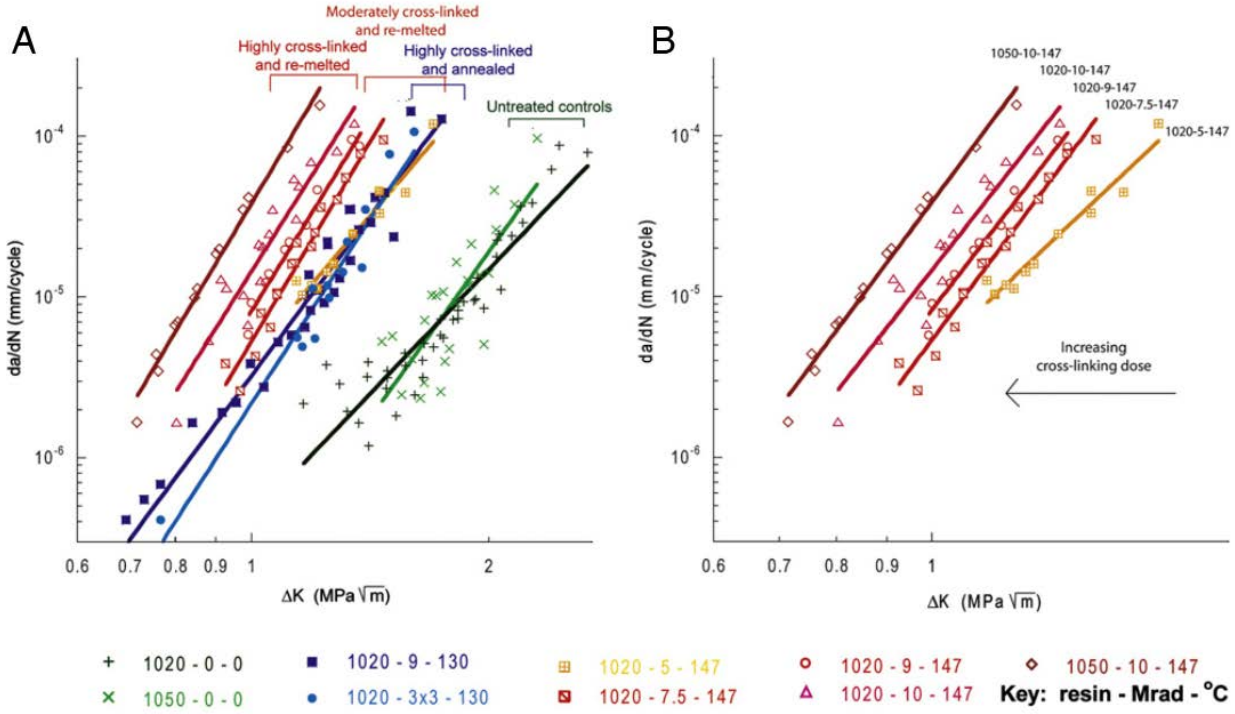

Figure 13: Fatigue crack propagation data showing (A) fatigue resistance of moderately crosslinked remelted and highly crosslinked annealed materials is increased compared to highly crosslinked remelted materials, but decreased compared to untreated controls, and (B) within remelted materials, fatigue resistance decreased with increasing radiation dose. Key: resin — radiation dose (Mrad) — subsequent thermal treatment (°C). (Atwood et al. 2011)

In the hip, which has a higher level of cross-shear and much lower contact stresses than the knee, the benefit of reduced wear from crosslinking seems to outweigh the disadvantages of reduced mechanical performance. Almost all of the current total hip replacement designs use crosslinked UHMWPE (Kurtz 2009), and the latest clinical follow-up reports have been favorable (Michael Doerner, BA et al. 2012; Kurtz et al. 2012; Grimm et al. 2012), aside from a report of delamination in a crosslinked hip liner associated with a roughened CoCr femoral head (Patten et al. 2010) and the aforementioned rim fractures. It is unclear whether these advantages will be seen with crosslinked UHMWPE in total knee replacements and more clinical trials and long-term follow-up is needed (Jasty et al. 2005; Ries 2005; Muratoglu, Mark, Vittetoe, et al. 2003; Lachiewicz & Geyer 2011; MacDonald et al. 2012).

Kinematics in fixed TKR designs and quantifying cross-shear

The design of the tibial spacer for total knee replacements is a complex and multi-faceted challenge and multiple factors must be taken into account: joint contact forces from patient loads; a wide range of loading activities; resistance to fracture, loosening, and wear; contact stresses; stress shielding; material properties; sterilization method; manufacturability; ease of implantation and other surgeon factors; knee kinematics; joint stability; sacrifice or retention of

the posterior cruciate ligament; and more. There are many variables in just the geometry of the tibial bearing surface itself (Figure 14), and these must be balanced to reproduce natural knee kinematics, allow an acceptable range of motion, and maintain stability, all while ensuring that contact stresses in the UHMWPE and bone are acceptable and minimize long-term wear and the risk of osteolysis (Goodfellow & J. O'Connor 1978; Willing & I. Y. Kim 2011; Banks & W. A. Hodge 2004; Omori et al. 2009). The kinematics of a total knee replacement especially can have a significant effect on wear by changing the sliding distance per cycle and the amount of cross-shear present (McEwen et al. 2005; Willing & I. Y. Kim 2009b). An accurate and complete model for wear under realistic cross-shear is needed to properly evaluate different designs and optimize the tradeoffs.

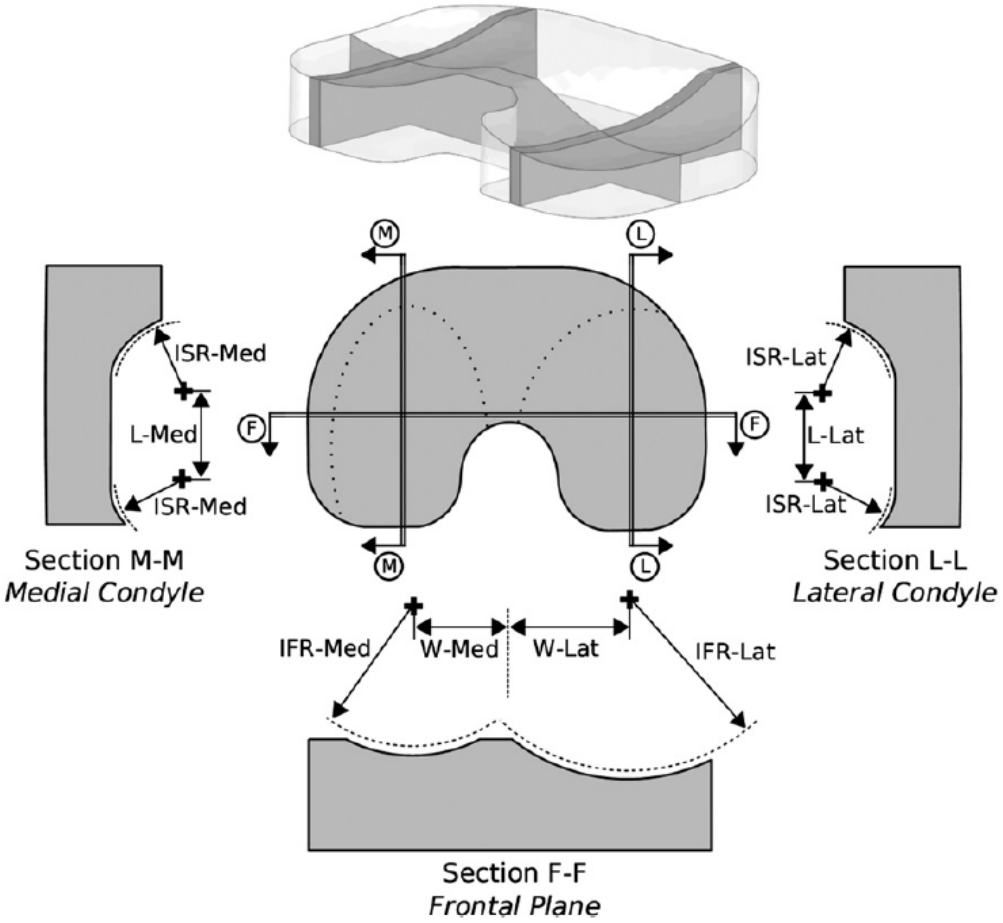

Figure 14: An example of design variables available for a tibial bearing surface of a fixed total knee replacement. "–Med" and "–Lat" denote medial and lateral parameters, respectively. (Willing & I. Y. Kim 2011)

In order to quantify the effect that cross-shear has on wear of UHMWPE, a method is needed to quantify the amount of shear at the sliding interface of the polymer component relative to the orientation of the microstructure. Over the last decade, several methods have been proposed. These methods can either be categorized as cycle based, in which information about the entire loading and path cycle is needed to calculate the cross-shear, or memory based, which bases the calculation of cross-shear only on the loading and path conditions of the previous

sliding increment. Three main fundamental concepts behind each of the cycle-based methods is the frictional force at the sliding interface, the direction of the relative slip velocity throughout the loading cycle, and a principle molecular orientation. The fundamental concept behind the memory based method is that the orientation of the surface microstructure at any given point in time can only be a function of the sliding that has already happened; the current direction of sliding is compared to the sliding direction over a previous length of the path, corresponding to a 'memory' related to how long it takes the polymer to completely re-orient itself. For calculating the cross-shear of complex geometry and sliding paths, all methods need to divide the polymer surface into many elements, and each finite area on the polymer bearing surface may experience a different amount of shear and cross-shear leading to certain level of wear at that location. The combined effect over the entire worn area will be related to the total UHMWPE wear volume.

A. Wang, in 2001, was the first to propose a model of UHMWPE wear based on cross-shear (Wang 2001). His model relates the amount of frictional work expended at the interface to the bond energy that must be overcome in order to break off a polymer fibril. Work is the product of the force used to move an object and the distance it slid (in the direction pushed). Instantaneous frictional work expended per unit surface area is a product of the contact pressure, P, the coefficient of friction, μ, and the magnitude of the instantaneous slip velocity vector, $\vec{v}$. To calculate the total frictional work expended per cycle, W, the rate of frictional work expended (frictional power) is integrated over one period of the cycle, T:

$$\dot{W}_T = \mu P|\vec{v}|\,; \qquad \text{eq. 11}$$

$$W_T = \int_0^T \mu P|\vec{v}|\,dt\,. \qquad \text{eq. 12}$$

Note that the frictional work expended is directly proportional to the tribological intensity in equation eq. 6 through the coefficient of friction.

The density of bonds aligned in the primary molecular orientation is much greater than the density of bonds perpendicular to this direction, so Wang proposed that for frictional work expended at an angle of θ, only the component perpendicular to the primary molecular orientation, $\bar{\theta}$, would be able to break off a fibril and generate wear debris. Therefore, the cross-shear basis of Wang's unifying wear model is $W_\perp$, the total frictional work expended perpendicular to the principle molecular orientation:

$$W_\perp = \int_0^T \mu P|\vec{v}|\sin^2(\theta - \bar{\theta})\;dt\,. \qquad \text{eq. 13}$$

Note that the sine term is squared because the perpendicular component of both the frictional force and the sliding velocity are needed. In his full model, Wang expresses the wear factor in terms of the coefficient of friction, diameter of the fibril wear particles, d, the bond energy of a crosslink bond, X_c, the density of the crosslinks, γ_c, the cross-shear ratio expressed in terms of the max rotation angle, α, of his rotating/sliding pin-on-disk tests used to validate the model, a proportionality constant, k', and experimentally determined constants μ_0 and X_0, representing a "critical" amount of friction and crosslink density, respectively:

$$k = k' \frac{d(\mu - \mu_0)}{2\gamma_c} \left(\frac{1}{X_c} - \frac{1}{X_0}\right)\left(1 - \frac{\sin 2\alpha}{2\alpha}\right). \quad \text{eq. 14}$$

Wang only uses a single primary molecular orientation for the entire polymer bearing surface and doesn't explicitly define it, but others have proposed that it should be the direction in which the most frictional work is expended or the angle perpendicular to the direction of minimum frictional work (Willing & I. Y. Kim 2009a). This orientation is defined between 0 and π radians relative to reference axis, since the slip directions θ and $\theta - \pi$ would produce the same orientation direction.

Turell et al. in 2003 were the first to introduce a cross-shear ratio when they analyzed their wear tests based on the wear factor, k (Turell et al. 2003), which is a function of the volumetric wear volume, V, normal load, L, and the total sliding distance per cycle. Based on Wang's model the wear volume should be proportional to $W_\perp$. Their wear tests consisted of a UHMWPE pin sliding along a rectangular path (of side lengths A and B, where $A \leq B$) without rotation and the sliding speed, coefficient of friction, and contact pressure were constant throughout the cycle. Therefore, the factor should be proportional to the ratio between the short side lengths of the rectangular path and the total perimeter of the rectangle:

$$k = \frac{V}{L(2A + 2B)} \approxeq \frac{\mu L(2A)}{L(2A + 2B)} \propto \frac{A}{A + B} \propto \frac{W_\perp}{W_T} = CS\,. \quad \text{eq. 15}$$

This cross-shear ratio, CS, is proportional to the ratio of the frictional work perpendicular to the principle orientation and the total frictional work, and ranges between 0 and 0.5.

Galvin et al. soon followed in 2006 and analyzed their wear results using cross-shear ratios based on the ratio of the perpendicular and parallel components of either the frictional force or frictional work (Galvin et al. 2006):

$$C_f = \frac{F_\perp}{F_\parallel} = \frac{\int_0^T \mu P \sin(\theta - \bar{\theta})\ dt}{\int_0^T \mu P \cos(\theta - \bar{\theta})\ dt}\ ; \quad \text{eq. 16}$$

$$C_w = \frac{W_\perp}{W_\parallel} = \frac{\int_0^T \mu P |\vec{v}| \sin^2(\theta - \bar{\theta})\ dt}{\int_0^T \mu P |\vec{v}| \cos^2(\theta - \bar{\theta})\ dt}\ . \quad \text{eq. 17}$$

However, in future work with Kang, they revert to simply defining the cross-shear using the perpendicular and total components of the frictional work, as described in eq. 15 (Kang, Galvin, Brown, Jin, et al. 2008). In a hip wear computer simulation they ran, calculated cross-shear ratios in the hip joint were between 0.1 and 0.5, with a median of approximately 0.15 (Kang, Galvin, Brown, Fisher, et al. 2008).

R. Willing, in 2009, expanded this line of cross-shear ratios by taking into account that the microstructure may not reach full alignment (Willing & I. Y. Kim 2009a). The fraction of the microstructure that is fully aligned would only be affected by the frictional work expended perpendicular to its orientation. The remaining fraction has a random alignment so on average half of the total frictional work would be perpendicular to the molecules and half would be aligned with them. Willing proposed that the ratio of aligned microstructure, β, would be equal to one minus the ratio between the actual and maximum possible amount of perpendicular

frictional work expended. The total wear volume would then be proportional to the combined effect on the aligned and random molecules, weighted by how much of each there were:

$$\beta = 1 - \frac{W_\perp}{W_{\perp max}} = 1 - \frac{W_\perp}{\frac{1}{2}W_T} \; ; \qquad \text{eq. 18}$$

$$V \propto \beta W_\perp + (1-\beta)\frac{1}{2}W_T = W_\beta \, . \qquad \text{eq. 19}$$

Note that Willing's ratio for cross shear, the crossing motion:

$$CM = 1 - \beta \, , \qquad \text{eq. 20}$$

is equivalent to Kang's cross-shear ratio, CS (eq. 15), except scaled to fall between 0 and 1. For a clearer view of how this parameter for cross-shear differs from the traditional perpendicular frictional work, eq. 18 and eq. 19 can be rearranged to a simpler form:

$$W_\beta = (2 - CM)W_\perp \, . \qquad \text{eq. 21}$$

An approach similar to all these methods, yet distinctly different, was used by Hamilton in 2005 (Hamilton et al. 2005). Hamilton based his analysis on the tribological intensity described in eq. 6. For consistency with the other methods described here, Hamilton's work will be presented here in terms of frictional work, since it is proportionally equivalent for a constant coefficient of friction. Hamilton proposed that the most probable direction of molecular orientation would be the dominant orientation of the tribological intensity, $\bar{\theta}$, defined as the average slip direction over one cycle, weighted by the frictional work expended:

$$\bar{\theta} = \frac{\int_0^T \mu P|\vec{v}|\theta \; dt}{\int_0^T \mu P|\vec{v}| \; dt} \, . \qquad \text{eq. 22}$$

Instead of using the component of frictional work perpendicular to this orientation, Hamilton uses the crossing intensity, σ, which he defines as an RMS-error type average of the tribological intensity multiplied by the radians between the instantaneous slip direction and the dominant orientation of tribological intensity:

$$\sigma = \sqrt{\frac{1}{T}\int_0^T [\mu P|\vec{v}|(\bar{\theta} - \theta)]^2 \; dt} \qquad \text{eq. 23}$$

For a cross-shear ratio, Hamilton uses the same philosophy as Willing and divides this crossing intensity by the maximum possible crossing intensity, σ_0, yielding the normalized crossing intensity, σ^*, which can range from 0 to 1 and can reach 0.1 in knees (Figure 15). This maximum value is calculated using the same loading profile and sliding distance per cycle, but a constantly and uniformly changing slip direction:

$$\theta(t) = \frac{2\pi}{T}t \; ; \qquad \text{eq. 24}$$

$$\sigma_0 = 2\sqrt{\frac{1}{T}\int_0^{\frac{T}{2}} \left[\mu P|\vec{v}|\left(\frac{\pi}{2} - \frac{2\pi}{T}t\right)\right]^2 \; dt} = \sqrt{\tfrac{1}{12}}\pi W_T \; ; \qquad \text{eq. 25}$$

$$\sigma^* = \frac{\sigma}{\sigma_0} \, . \qquad \text{eq. 26}$$

Note that the integral is taken over just half of a full cycle and the result multiplied by two in order to account for the $0 \leq \theta \leq \pi$ constraint.

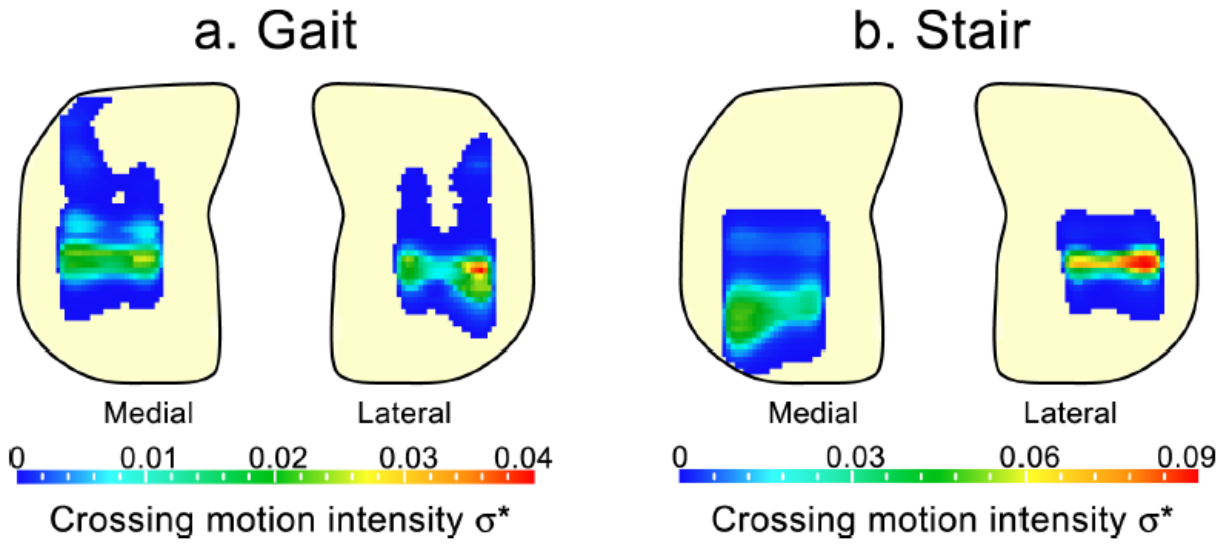

Figure 15: Normalized crossing intensity for (a) gait and (b) stair activities based on *in vivo* kinematic data (Sawyer et al. 2003).

All of these cycle-based methods suggest that the total wear volume should be proportional to some measure of perpendicular frictional work expended and hence that the wear factor should be proportional to some measure of a cross-shear ratio. However, all of them predict no wear under unidirectional sliding (no cross-shear); in most wear tests, volume loss is significantly reduced under unidirectional sliding but it is still present. Another weakness of these approaches is that the cross-shear, and hence the amount of wear, is averaged over one cycle and so cannot be modeled for an arbitrary or constantly changing loading and sliding path. These approaches also imply that a given path shape will have a single wear rate no matter its size, which doesn't make intuitive sense (for example, a square with 'ultra-long' sides should have a similar wear rate as a straight line, not a small square) and has evidence of path-size dependence has been shown in pin-on-disk tests (Dressler et al. 2011). Recently, two methods have been introduced that model the wear rate at any point in the path based on a 'memory' that the material retains of its recent history of sliding direction.

The method introduced by Petrella et al. modifies Archard's law by adding a wear volume term based on cross-shear to the wear term based on tribological intensity (Petrella et al. 2011). The cross-shear term is an average of the sine of the past sliding angles compared to the current sliding angles:

$$d\delta = k_0 d\tau + k^* \, m \, d\tau \; ; \qquad \text{eq. 27}$$

$$m = \frac{1}{S_c}\int_0^{S_c} |\sin[\theta(0) - \theta(\chi)]| \, d\chi \; ; \qquad \text{eq. 28}$$

$$W_m = \int_0^T mP|\vec{v}| \, dt \; ; \qquad \text{eq. 29}$$

where m is a measure of the alignment calculated for that instant of sliding and can vary between 0 and 1, χ is the distance backwards along the sliding path, and S_c is the distance required to

achieve full alignment. This approach is able to account for the non-linear trend in wear tests performed by other researchers (Turell et al. 2003). Note that Petrella presents these equations in summation notation where it is implied, though not explicitly stated, that the sine angle factors should be averaged over the sliding distance and not time. For a ratio parameter, they define a normalized cross-shear intensity, X^*, which is the percentage of maximum wear achieved:

$$X^* = \frac{\int_0^{T_f} P|\vec{v}|m\, dt}{\int_0^{T_f} P|\vec{v}|\, dt}, \quad \text{eq. 30}$$

where T_f is the total time of the wear scenario being modeled.

The other memory-based method is similar in approach, but does not include a linear sliding wear component and uses an exponential decay weighting factor for the sliding angle history instead of a simple distance average (Strickland et al. 2012):

$$d\delta = k_m \zeta P ds\ ; \quad \text{eq. 31}$$

$$\zeta = \frac{1}{S_c}\int_0^{\infty} e^{-\chi/Sc}|\sin[\theta(0) - \theta(\chi)]|\, d\chi\ ; \quad \text{eq. 32}$$

$$W_\zeta = \int_0^{T} \zeta P|\vec{v}|\, dt\ ; \quad \text{eq. 33}$$

where ζ is their alignment factor to account for cross-shear that they term a surface potential. Although they do not introduce a ratio for the cross-shear, a basic version could use the same approach as Petrella and normalize based on the tribological intensity:

$$\mathrm{Z}^* = \frac{\int_0^{T_f} P|\vec{v}|\zeta\, dt}{\int_0^{T_f} P|\vec{v}|\, dt}. \quad \text{eq. 34}$$

Strickland describes their approach not just as a wear model, but as a method that could be used for simulating other wear models as well. For example, it could also use this method to simulate a wear model in which the wear rate does not vary based on contact pressure. Like most of the wear models described here, this is also designed for numerical methods of computer simulation and so the equations were originally described in summation notation. Here though, the difference between the summation notation and the integral theoretical form is non-trivial. Instead of a using a linear incremental sliding distance, Δs, they suggest an exponential decay distance such that the change in wear depth for time step i is:

$$\Delta\delta_i = k_m \zeta_i P_i\left(1 - e^{-\Delta s_i/Sc}\right). \quad \text{eq. 35}$$

This is based on their experimental wear tests in which the wear rate for a pin on a square sliding path was shown to only be a function of the number of cycles and not the total sliding distance (Dressler et al. 2011). They suggest that the wear rate of a surface that is fully aligned is greatest immediately following a 90 degree turn and then decays as the polymer becomes aligned to the new sliding direction, until the wear rate is eventually negligible. This means there is a maximum wear depth that can take place for 90° turn, no matter how far it eventually ends up sliding in that direction. The amount of amount of alignment in a particular direction is therefore also a function of how far it has slid in that direction and how recent that sliding event took place. To account for this in their model, they propose a 'strength' array, λ_χ, that tracks how

much each sliding increment and angle is contributing to the current level of alignment. The angle of the most recent sliding increment has an effect equivalent to the percentage of the final wear depth reached in this sliding direction, and the effect of the past sliding increments is then decreased such that the total strength array always sums to 1:

$$\zeta_i = \sum_{\chi} \lambda_\chi \left|\sin\left(\theta_i - \theta_\chi\right)\right| \; ; \qquad \text{eq. 36}$$

$$\lambda_\chi = \left(1 - e^{-\Delta s_\chi / S_C}\right) \prod_{k=1}^{\chi-1} \left(e^{-\Delta s_k / S_C}\right) \; ; \qquad \text{eq. 37}$$

$$\mathrm{Z}^* = \frac{\sum_{j=1}^{N_w} \sum_{i=1}^{N_T} \zeta_{ij} P_{ij} \Delta\delta_i \, \Delta w}{\sum_{j=1}^{N_w} \sum_{i=1}^{N_T} P_{ij} \Delta\delta_i \, \Delta w} \; ; \qquad \text{eq. 38}$$

where the index χ is for tracking the sliding angle and distance of previous time steps, counting back from the current location (the current location being $\chi = 0$), and Π denotes product notation, which here is equal to 1 when $\chi = 1$. Although the summation in eq. 36 technically goes to $\chi = \infty$, the strength array decays such that going back through a distance of $5 \times S_C$ only yields about 0.5% error. One important thing to note about this proposed model is that the alignment is not considered to change with contact pressure. This means that the effect on alignment and future wear of a short side-step in an otherwise straight wear path would be the same even if the load during that side-step was much higher or much lower than the load on the rest of the wear path.

The introduction of these many different ways of quantifying cross-shear (Table 2 and Table 3) has usually been accompanied with wear testing data to validate the approach. However, no wear tests have been performed to vigorously compare them to each other and determine which works best under a wide range of scenarios.

Table 2: Summary of tribological and cross-shear parameters.

Variable	Name	Description
s_l	Sliding distance	Relative sliding distance from the perspective of a fixed element on the UHMWPE disk
F_T	Total Frictional Impulse	Frictional force (load times coefficient of friction) multiplied by the time interval applied
$F_\perp$	Perp. Frictional Impulse	Component of frictional force perpendicular to the PMO, multiplied by the time interval applied
τ_l	Tribological Intensity	Load multiplied by the relative sliding distance
W_T	Total Frictional Work	Frictional force multiplied by the relative sliding distance
$W_\perp$	Perp. Frictional Work	Component of frictional power perpendicular to the PMO
W_β	CM weighted Perp. Fr. Work	A CM-weighted combination of perp. frictional work and total frictional work to account for incomplete alignment
σ	Crossing Intensity	An RMS-type average of the frictional work multiplied by the angle between the PMO and the relative velocity vector
W_m	Cross-shear Intensity	The frictional work scaled by the perpendicular component, averaged over the previous sliding distance needed for full alignment, of the current sliding vector and the previous sliding vectors.
W_ζ	Crossing Surface Potential	The frictional work scaled by the perpendicular component, weighted with an exponential decay over the previous sliding distance needed for full alignment, of the current sliding vector and the previous sliding vectors.

Table 3: Summary of the ratios of cross-shear.

Variable	Name	Description
C_f	Perp. to Aligned Friction ratio	Ratio of the frictional impulse components that are perpendicular to parallel to the PMO
C_w	Perp. to Aligned Frictional Work ratio	Ratio of the frictional impulse components that are perpendicular to parallel to the PMO
CS	Cross-shear Ratio	The perpendicular frictional work component normalized by the total frictional work (defined to fall between 0 and 0.5)
CM	Crossing Motion	Perpendicular frictional work component normalized by the maximum possible frictional work component (ranges from 0 to 1)
σ_0	Normalized Crossing Intensity	Crossing intensity normalized by the maximum possible crossing intensity
X^*	Normalized Cross-shear Intensity	Cross-shear intensity normalized by the cross-shear intensity that would be present if the sliding direction were always perpendicular to the UHMWPE alignment direction
Z^*	Normalized Crossing Surface Potential	Crossing surface potential normalized by the crossing surface potential that would be present if the sliding direction were always perpendicular to the UHMWPE alignment direction

Other factors that affect wear of UHMWPE

There have been several methods suggested on how to adjust the wear factor in Archard's law to account for cross-shear, but there are a few other wear models and special considerations for studying the wear of UHMWPE. Abrasive wear in polymers has been linked to ultimate properties, such as ultimate tensile strength and strain at failure. Delamination wear is related to the fatigue properties and strain life, but has also been connected to lamellar thickness. There is also much debate in the literature about the influence of load on wear rate. Additionally, these mechanisms may be different if the polymer component is the plate rather than the pin. Wear is also affected by the contact geometry and the type of lubricant used.

Ratner and Lancaster have argued that removing a wear particle requires the amount of work equal to the area under the stress-strain curve (Lancaster 1969). They approximate this work as the product of the breaking stress, σ_u, and the elongation at break, ε_u, and propose then that the wear rate of polymers should be proportional to the inverse of this product:

$$\dot{V} = k\frac{\mu L}{H\sigma_u\varepsilon_u} \propto \frac{1}{\sigma_u\varepsilon_u} \ . \qquad \text{eq. 39}$$

They have also suggested that instead of using measures of material toughness from monotonic loading, it would be more appropriate to consider the toughness under the much higher loading rates that occur during sliding. However, they report that wear rates have not shown a convincing correlation with impact strength.

Wang et al. proposed a microscopic wear model based on a similar idea, except that he suggested a wear particle would break free after a particular location had reached a critical strain criterion, ε_c, where all the ductility has been exhausted (Wang, Stark, et al. 1995). Together with an empirical relation between the average roughness and the number of asperities, an assumption on how asperities between the two surfaces will be in contact, and the assumption that the real contact area will be proportional to the yield stress, he proposed the following relationship:

$$\dot{V} \propto \frac{L^{3/2}R_a^{3/2}}{\sigma_y^{3/2}\varepsilon_c} \ . \qquad \text{eq. 40}$$

They suggest that this wear mechanism is a dominating factor for wear in hip replacements, where contact stresses are lower, but they suggest a different model based on surface fatigue would be more dominant in the knee (Wang, Sun, et al. 1995). For the lower conformity conditions of the knee, it is not only the microscale UHMWPE asperities that are in direct contact that can reach yield, but also the surface and near-surface regions. Shear cracks could develop and grow under cyclic loading until they reach another crack or the surface. This is analogous to low-cycle fatigue where crack growth rate is related to the ultimate strain, the plastic strain amplitude, $\Delta\varepsilon_p$, and an empirical constant, α. The volumetric wear rate should be proportional to the crack growth rate:

$$\dot{V} \propto \left(\frac{\Delta\varepsilon_p}{\varepsilon_u}\right)^{\frac{1}{\alpha}} \ . \qquad \text{eq. 41}$$

This is the most basic formulation for a fatigue-based wear mechanism. Delamination theory and fatigue wear was first described by Suh for metals (Suh 1973), and others have adapted it for a damage-tolerant fatigue approach in polymers (Omar et al. 1986).

Van Citters expanded the delamination theory of wear by adding a composite approach to account for the differences in stiffness between crystalline and amorphous phases (Van Citters 2006). The differences in stiffness lead to differences in shear strain under the shear stress from frictional sliding that cause local tensile stresses at the interface of the crystalline regions (Figure 16). Cracks can initialize at these interfaces and then continue to propagate under mode I (tension) and mode II (shear) crack growth. The thicker the lamellae, the greater the tensile stresses at the interface and the more cracks and wear debris should form.

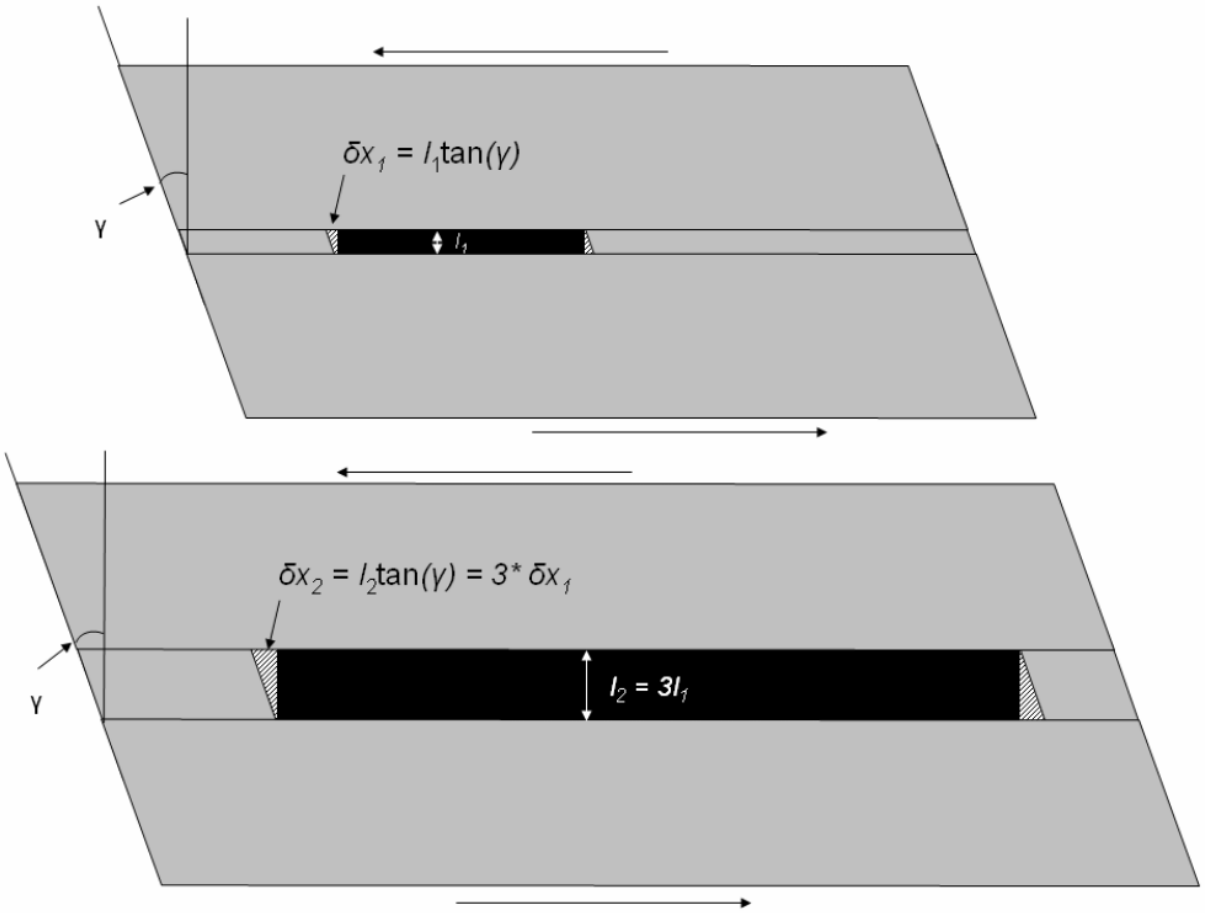

Figure 16: Schematic illustrating the effect of lamellar size on tensile stress concentrations at the edge of the lamellae interface. Crack initialization is governed by composite theory and crack growth and debris liberation by delamination wear theory. (Van Citters 2006)

Despite these many different models for wear mechanisms, Archard's Law is still commonly used in the orthopaedic community. Archard developed his adhesion wear model from work with metals, and showed a linear dependence between wear volume and load (Archard 1953). The same does not necessarily hold true for polymers though, and UHMPWE in particular. Studies of UHMWPE wear have resulted in wear depth rates that increase

exponentially with contact pressure (Rose et al. 1982; Klapperich et al. 1999; Rostoker & Galante 1979), increased logarithmically with contact pressure (Walker et al. 1996; Wang et al. 2001; Saikko 2006; Barbour et al. 1995), and been unaffected by contact pressure (Mazzucco & Spector 2003; Galvin et al. 2009; Vassiliou & Unsworth 2004). This range of results may be attributed to the many interacting parameters at work in a tribological system that can change the type of asperity interaction. The incremental effect of contact pressure may be different depending on the wear mechanisms that dominate when if the magnitude is low (less than 3-5 MPa), moderate (but below yield), or greater than yield. The effects on wear of the interplay between load, apparent contact area, and apparent contact pressure has not been well explained, and factors such as wear debris trapped in the contact area and acting as roller bearings, or lubrication starvation, can complicate matters further.

Another important aspect of the surface contact is the geometry. For laboratory testing, the contacts are generally either flat pin on a flat disk or a hemispherical tipped pin on a flat disk. For tribo-testers that can simulate rolling, this later is often called ball-on-flat contact. A flat pin-on-disk contact is more controlled, in that you theoretically have a uniform contact pressure across the entire wear surface. However, the edges of the pin are a stress concentrator (Barbour et al. 1995), greatly increasing the pressure, and unrealistic surface characteristics such as a center "nipple" (Vassiliou & Unsworth 2004) and "protuberances" (Saikko & Ahlroos 2000) have been reported on the polymer surface. The center of flat pins may also become lubrication starved (Jin et al. 2006) and wear debris will have a more difficult time escaping, potentially changing the nature of the asperity contacts and wear mechanisms. While these effects may be appropriate for hips, this is not the best representation of the contact area and conformity in knees.

Also, for a flat pin-on-disk test, the polymer must always be the pin because otherwise the sharp corner on the metal pin would dig into the polymer disk as it wore and have an even greater stress rising effect. For hemispherical contact, the metal pin on an UHMWPE disk has been shown to have a significantly higher wear factors than an UHMWPE pin on a metal disk (Cornwall et al. 2001; Barbour et al. 1997). This may be due to the difference in the cyclic nature of the load and the effect it has on fatigue or the viscoelastic stress, or because of differences in how easily wear debris can escape the contact.

Tribo-testers

Researchers first investigated the tribology of TJAs using single directional "pin-on-disk" wear testers with continuous or reciprocating paths. However, wear rate results from these tests did not agree well with *in vivo* observations and several researchers reported that wear of UHMWPE is very sensitive to multidirectional sliding and cross-shear (Wang, Sun, et al. 1997; Bragdon et al. 1996).

Many research groups across the world are now using laboratory wear testing machines that incorporate some degree of cross-shear (Figure 17), which produce wear rates that are at least on the same order of magnitude as those observed *in vivo* (Bragdon et al. 2001; Van Citters

et al. 2004; Saikko 1998). One of the more basic types of cross-shear testers is a circularly translating pin-on-disk (CTPOD) machine (Saikko 1998), in which a stationary polymer pin is loaded against a metallic disk that moves in a circular path without rotating. AMTI's Ortho-POD (AMTI n.d.) and DesJardins's Multi-Axis Cross Shear (MAX-Shear) Wear Testing System at Clemson University (Gevaert et al. 2005) are both pin-on-disk testers that simulate multidirectional sliding with two separate axes of motion. J. Fisher's lab at the University of Leed's has a tribotester that produces cross-shear on a rotating polymer pin loaded against a unidirectional linearly reciprocating metallic disk (Kang, Galvin, Brown, Fisher, et al. 2008). Laboratory pin-on-disk testers are useful for a preliminary evaluation of materials, but cannot capture all aspects of complex motion that occurs in the knee.

Wear Test Method	Location of Polymer	Motion of Bearing Surfaces	Relative Motion of Shear Forces w.r.t. Polymer	Shear on Polymer: Multi-directional?	Shear on Polymer: Change path?	Shear on Polymer: Cross path?	Bearing Contact at Discrete Points on Polymer	Resultant Damage Track on Polymer
Rotating POD	Pin	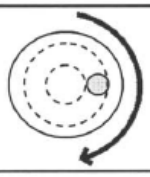		○	○	○	Contin-uous	**N/A** (whole poly surface in contact)
	Disc	Same as above		○	○	○	Inter-mittent	Circular
Recipro-cating POD	Pin	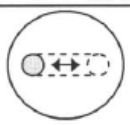		○	●	○	Contin-uous	**N/A** (whole poly surface in contact)
	Disc	Same as above		○	●	○	Inter-mittent	Linear
CPTOD	Pin	See Figure 9	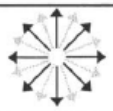	●	○	○	Contin-uous	**N/A** (whole poly surface in contact)
Change path POD	Pin	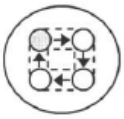		●	●	○	Contin-uous	**N/A** (whole poly surface in contact)
Multi-axial POD	Pin	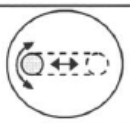	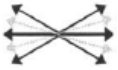	●	●	●	Contin-uous	**N/A** (whole poly surface in contact)
	Disc	Same as above		○	●	○	Inter-mittent	Linear
Cross path POD	Disc			●	●	●	Inter-mittent	Discrete areas of separable cross-path, change-path, and linear damage track
Total Knee or Hip	Analogous to Disc	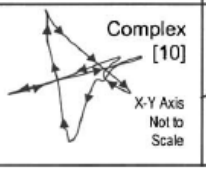	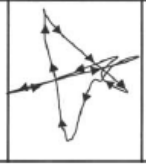	●	●	●	Inter-mittent	Complex; distributed over discrete areas[6]

Figure 17: Summary of wear test methods. Symbols ○/● indicate absence/presence of cross-shear. (Gevaert et al. 2005)

There are a few wear testing machines that try to capture the rolling motion (about an axis parallel to contact surface) present in knees. Tribotesters that simulate pure unidirectional sliding combined with rolling have been used by F. Kennedy's lab at Dartmouth (Figure 18) as well as a few others using a different mechanisms (Oñate et al. 2001; Schwenke et al. 2005). A. Wang at Howmedica, Inc. has a tribotester that replicates rolling (actually sliding since there's

no translation) and rotation (axis perpendicular to surface, in this case about the point of contact) (Wang et al. 1998). V. Saikko at Helsinki University of Technology (Saikko et al. 2001) and T. Schwenke at Rush University Medical Center (Schwenke et al. 2008) have both developed tribotesters that incorporate rolling of a metal ball or cylinder on a rotating flat disk with unidirectional sliding. In both of these cases, however, the rotation is based on the center of the polymer disk, and not the center of the metal ball. These cases are similar but not identical because sliding is involved and most of the rotation for *in vivo* knee kinematics is centered on the lateral condyle (rolling disk equivalent).

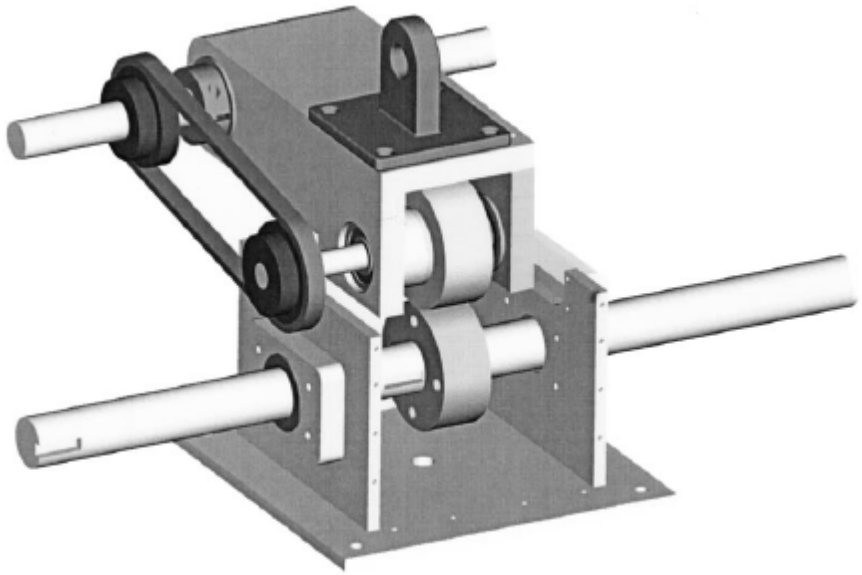

Figure 18: Close-up view of a CAD model of one test station from Van Citter's Rolling-Sliding Tribotester. One rolling puck is UHMWPE, the other is metallic, and the drive train can be adjusted to control the sliding/rolling ratio. (Van Citters et al. 2004)

Most of these wear testers only utilize two dimensions (2D) of motion, be it 2D sliding paths, rolling and sliding in one direction, or unidirectional sliding combined with rotation. These methods are very useful in studying fundamental wear behavior, comparing materials, and optimizing formulations, but joint kinematics in the knee can be quite complex and involve 2D sliding combined with rolling and rotation along with varying loads and complicated geometry. In order to analyze specific implant designs and replicate gait motion and loading, many medical companies utilize hip and knee joint simulators (Figure 19). Joint simulator studies are useful for evaluating a future design and are required by the Food and Drug Administration, but they are not well suited for comprehensive and fundamental research about specific wear mechanisms and are not always successful at predicting clinical outcomes (Affatato et al. 2008).

Figure 19: The commercially available ADL knee simulator controls dynamic loading, flexion, internal-external rotation, and anterior-posterior translation, with free motion allowed in medial-lateral translation and valgus rotation (AMTI n.d.).

Although both traditional laboratory testing machines and joint simulators can yield valuable insight and can be used to answer a myriad of questions, there is a gap in the fundamental understanding of UHMWPE wear that neither type of equipment is well suited for. Pin-on-disk wear testers are good for comparing how different material treatments will affect wear and for controlling for a wide range of specific variables. Simulators are good at evaluating a specific combination of material and implant design for specific gaits or sets of gaits. However, the pin-on-disk testers cannot test the effects of more complex motions, which are important for UHMWPE wear. Simulators are also ineffective at isolating specific variables within designs, which is needed to understand the scientific relationships. To address the fundamental wear behavior, tests need to both isolate specific variables and retain important aspects of the motion and stress condition (Figure 20).

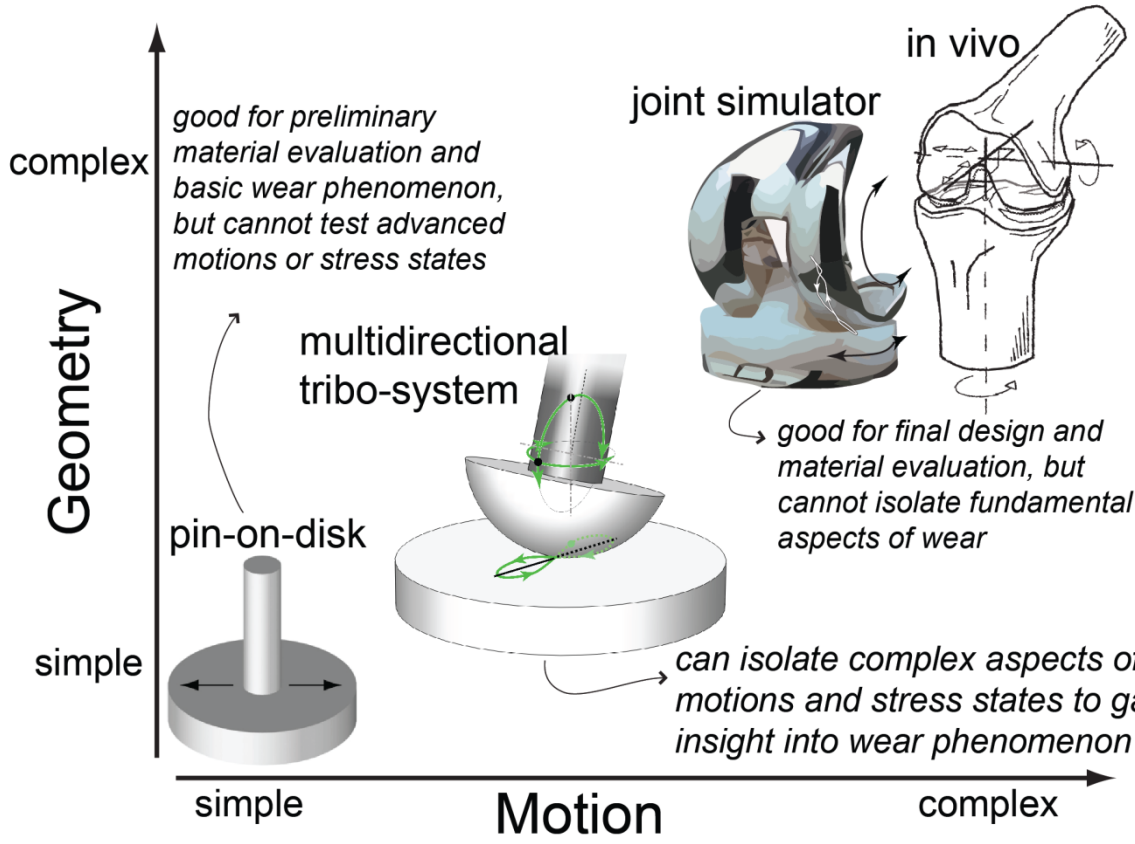

Figure 20: There are important tribological questions that can be investigated in the missing gap between the typical pin-on-disk test and complete joint simulation. Images adapted from (Affatato et al. 2008; Woo et al. 1999) and <www.thewillingtonkneeunit.com>.

1.3 - Research Questions

Experimental aims and summary of method

Cross-shear induced wear of UHMWPE in total knee replacements arises from a combination of internal-external rotation, flexion-extension, and anterior-posterior and medial-lateral sliding. The specific geometric design of the bearing surface can affect the kinematics, but the fundamental relationship between the kinematics and wear rate is not well studied. There are several competing theories but they have all either only been validated with flat pin-on-disk testing, which may not represent *in vivo* conditions accurately enough, or on knee simulators, where their individual effects cannot be studied. The aim of this research is to

i) investigate the individual and combined effects of knee kinematics on the wear of conventional UHMWPE,

ii) determine which measures of cross-shear can best be used to predict this wear, and

iii) examine the role of microstructural evolution on the cross-shear wear mechanism.

These experiments were carried out with a custom ball-on-flat, multidirectional tribo-system in order to have a controlled and fundamental approach while properly mimicking physiologically relevant conditions (Figure 21).

To investigate the role of the different types of kinematics, eight different combinations of motion were tested: either a linear reciprocating wear path or a “figure 8” with a specific crossing angle, either no rolling motion or a specific ratio of rolling to sliding, and either no rotation or specific rotation angle. The cross-sectional area of the wear scar was then measured and compared. The wear surfaces will also be examined with scanning electron microscopy for evidence of prominent wear mechanisms.

To determine which measures of cross-shear are most appropriate for design and optimization of total knee replacements, a computer model was developed to simulate the distribution of loading, sliding velocity, and sliding direction across the wear scar at the cross-section of interest. These were used to calculate the total tribological intensity for each motion combination as well as all the different measures of total cross-shear and cross-shear ratios described in the UHMWPE literature. The many different fits of cross-shear and wear will be compared.

To examine the role of microstructure on wear mechanisms under these cross-shear conditions, sections were cut from the UHMWPE disk and etched in an acid bath to remove the amorphous phase. The orientation of the remaining lamellae will be measured using an image analysis program. The distribution of lamellae orientations at the wear surface will be compared to that of an un-worn surface, and the distribution of lamellae orientations of the near-wear-surface layer will be compared to that of the sub-wear-surface.

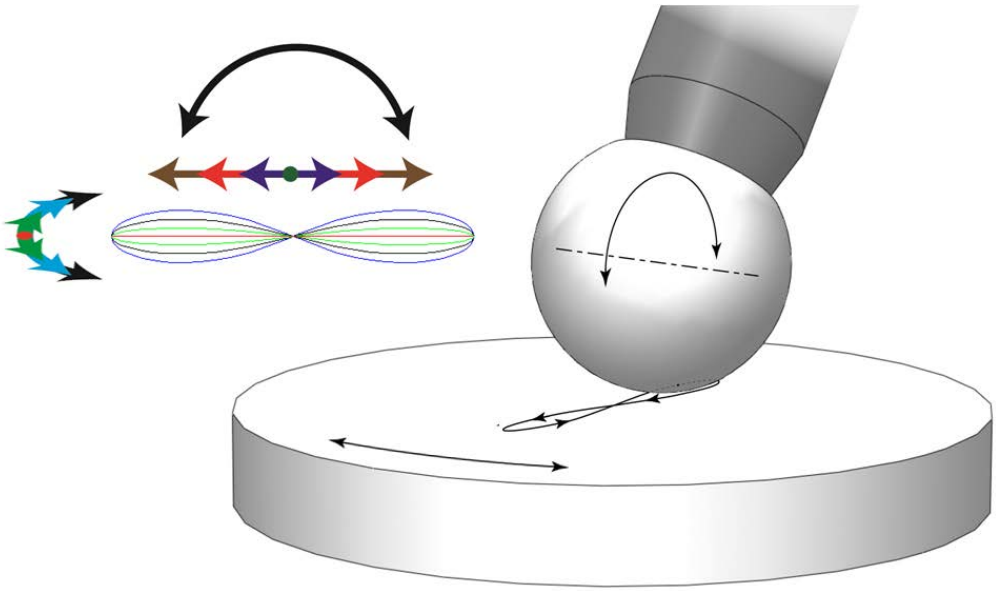

Figure 21: Different combinations of sliding, rolling, and rotation will be investigated using a fundamental approach with physiologically relevant kinematic and contact conditions.

Chapter 2: Methods and Materials

2.1 - Custom Multidirectional Tribo-system

A key aspect of this research is the design and construction of a tribo-system that could simulate realistic physiological conditions (such as motion and stress conditions), yet also control and isolate specific variables (Patten 2008). Designing and building a tribo-system that is robust enough to apply a large range of loads for millions of cycles and adaptable enough to test many types of samples with any sort of wear motion poses many challenges. To simplify the system and start with a relatively inexpensive and robust frame, the system uses a two-axis computer numeric controlled (CNC) vertical-knee milling machine as the base (Anilam, Inc., Jamestown, NY). The machine is already capable of automated 2D motion and can be easily retrofitted by replacing the milling head with a frame that can be used to attach specimen holders and loading mechanisms (Figure 22). Primary design concerns were strength, modularity, loading mechanism, sample size, sample orientation, and ease of operation.

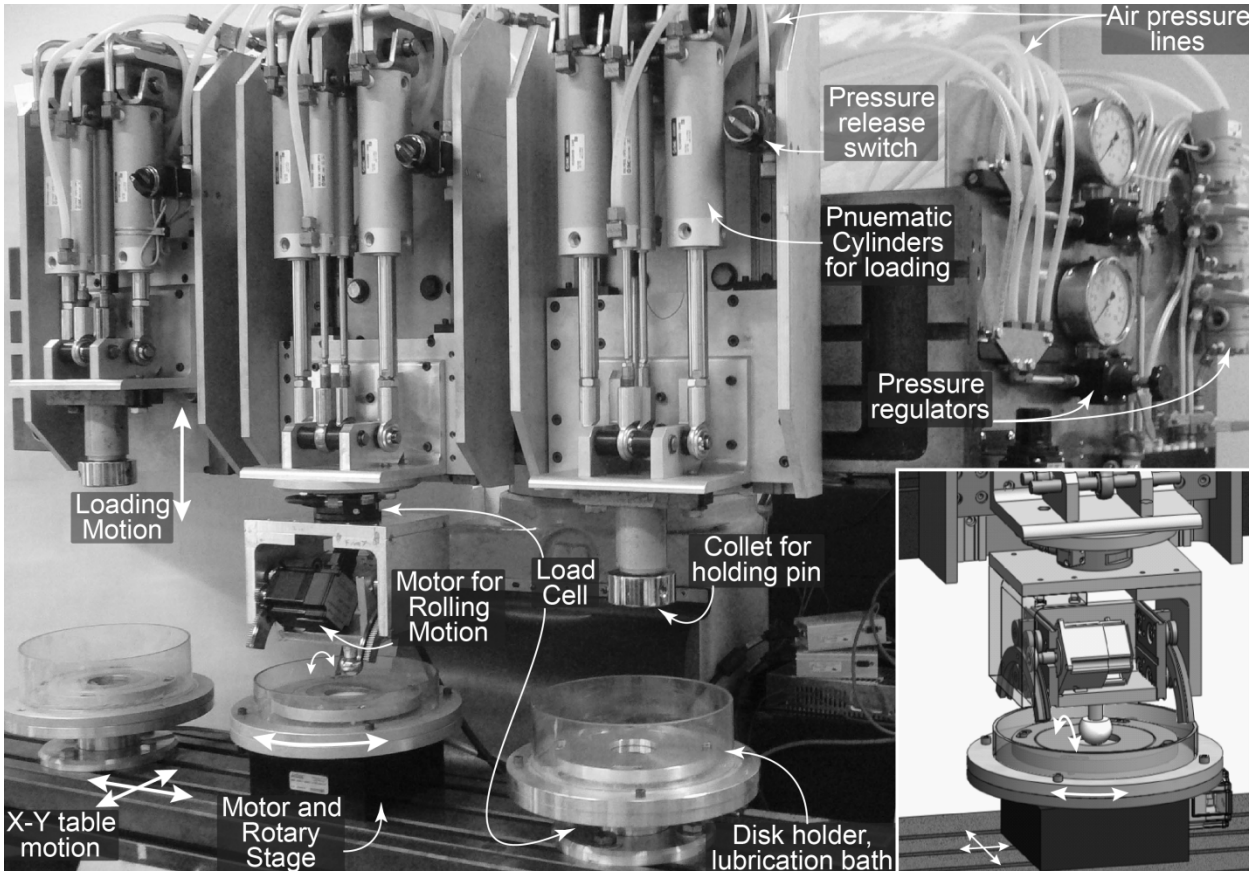

Figure 22: The multidirectional tribo-system (main picture) uses a CNC milling machine as its base and can be used for two-direction pin-on-disk sliding, or rolling and rotation can be included for ball-on-flat wear testing (inset).

Strength and stiffness are major concerns in any mechanical testing machine. When performing friction testing in particular, chatter induced by unwanted flexing of the sample holder can drastically affect the loading. Tightly coupled to the strength of the machine is the loading capacity. Although it is important to simulate physiological loading levels (on the order of thousands of Newtons), many laboratory wear tests are performed with smaller samples, which require less loading (tens of Newtons).

Wear testing results tend to have large variability and run for days or weeks, so having multiple stations running simultaneous tests is important in order to achieve statistical significance in a reasonable amount of time. Quick setup and measurements times, and other ease-of-use features, were equally valuable. To make it easier to manufacture and assemble the tribo-system, increase the adaptability of the testing setups, and allow for interchangeable parts, components were designed to be as modular as possible and off-the-shelf items were used whenever feasible. Most components that had to be custom machined were made of 6061 aluminum for easy manufacturing and prototyping.

A CNC milling machine was chosen as the base of the tribo-system because of its inherent mass, strength, and stiffness. Used CNC milling machines with two degrees of motion already built in are fairly common and have been designed to support large loads for many millions of cycles. The attached motors are capable of moving the stages at rates in excess of 60 mm/s – more than enough to cover the average joint sliding velocity of 30 mm/s. A second worktable mounted vertically to the ram allows for stationary, modular fixturing above the moving platform. For pin-on-disk testing, any type of pin geometry can be used and the ultra-high molecular weight polyethylene (referred to hereafter as either UHMWPE or polyethylene) component could be either the pin or the disk. Any type of path can be programmed, such as circular translation, square, or a “figure 8.” The ball-on-flat testing can replicate any combination of cross-shear sliding, rolling, and rotation relevant to total knee replacements, and could even replicate motions relevant to total shoulder replacements – very few wear studies specific to total shoulder replacements have been performed and they are not quite as advanced as total hip or knee replacements.

The loading mechanism was designed to be capable of producing the loads that may be expected in the gait of a human. Pressurized air was chosen for delivering constant vertical loads across the multiple test stations. Each station is equipped with two large, 2-inch diameter, and two small, 0.75-inch diameter, pneumatic cylinders. The large diameter cylinders can provide a high base load while small cylinders have higher sensitivity for control. With 100 psi from the house air supply, the capacity for four pneumatic cylinders provide nearly 3,200 Newtons of force (720 lbf), or 40 MPa of stress on a flat 10 mm diameter pin-on-disk experiment. This corresponds to some of the largest contact stresses reported in knees (Bartel et al. 1986) applied on the largest size flat pin used in orthopeadic pin-on-disk testing (ASTM 2006). Modularity in the design and use of pneumatic cylinders of different sizes allows for various ranges of forces to be achieved. In the primary configuration, two manual regulators control upper and lower pressures common to the small cylinders at all stations and electropneumatic transducers

(EP211-X27-5V, Omega Engineering inc., Stamford, CT) control the upper pressures on the large cylinders for each individual station. These electronic pressure regulators have a 0-27 psi output control with a 0-5 V signal. Each station is equipped with a pressure-release switch to quickly drop the load and raise each station. An adjustable damper at each station ensures smooth loading motion and prevents sudden motions of the system that could cause injury or overload the load cells.

Each station is fitted with a load cell to monitor and help control the normal forces during the wear testing. The system has one 6-axis load cell, which can be used to measure friction, and two 1-axis load cells, which can only be used to measure the normal load. The 6-axis load cell (Gamma SI-32-2.5/SI-65-5, ATI Industrial Automation, Apex, NC) is capable of accurate normal load measurements in either the 0-100 N or 0-200 N range, depending on the calibration, and can also measure the horizontal frictional forces in both directions and all three axes of torque. The 1-axis load cells were designed and machined in-house, and feature a 3-spoke cantilevered beam design with 12 high-quality strain gages mounted to the beams and wired in a wheat-stone bridge circuit such that sensitivity to off-center loading is minimized. All load cells are of similar size and have identical hole-patterns so that they can be interchanged between the stations.

The loading mechanism is designed with a versatile fixturing end to attach a simple pin sample holder or additional rotational hardware for the rolling/sliding behavior. A 5C collet and a quick release collet holder secure the sample pins. The disk sample holder can hold a range of sample sizes and materials, primarily 2.5- and 3.5-inch diameter disks of CoCr and polyethylene, respectively. The outer polycarbonate cylinder is a safety shield to prevent the lubricant from leaking or splashing onto the work table. Lubricant such as bovine serum can be retained within the basin formed by the clamping plate as evaporation rates are low.

This configuration is very adaptable and can be easily modified for many different types of tests. For regular pin-on-disk testing, a collet holds the pin and is mounted to the loading frame, and the disk and lubrication bath are mounted to a load cell on the moving table. To simulate flexion (rolling), a CoCr ball is mounted to a carriage assembly that moves along a curved rail (FCP/R25-159, Bishop-Wisecarver Corporation, Pittsburg, CA). The ball is mounted such that the center of curvature of the ball coincides with the center of curvature of the rails so that the contact point at the bottom of the ball has no displacement in the vertical direction (Figure 23A). The carriages have a maximum total range of approximately 90° (45° in each direction) and the can handle up to 400 N of vertical load. A servo-style stepper motor (QCI-A23K-3, QuickSliver Controls, Inc, Covina, CA) mounted to the carriage assembly drives the carriage back and forth along the track through a rack-and-pinion mechanism. This assembly is mounted to a load cell and then to either the loading mechanism or to the rotary stage (Figure 23B). The rotary stage is a high-accuracy, 45:1 ratio worm gear with a 800 N load capacity and max speed of 10 rpm (model 306045-1-S-M02-C001-L09, LinTech, Monrovia, CA), driven by the same model motor as the rolling motion. The rotary stage can also be mounted between the disk/lubrication bath and the milling table for a different type of rotation motion, or to provide

continuous rotation for a unidirectional pin-on-disk wear test or Stribeck curve experiments. The system can currently be configured for three pin-on-disk test stations, for one rolling/rotation and one control ball-on-flat station, or for one rolling, one rotation, and one control ball-on-flat station. One station can be converted to a load-soak control for tests that use gravimetric measurements.

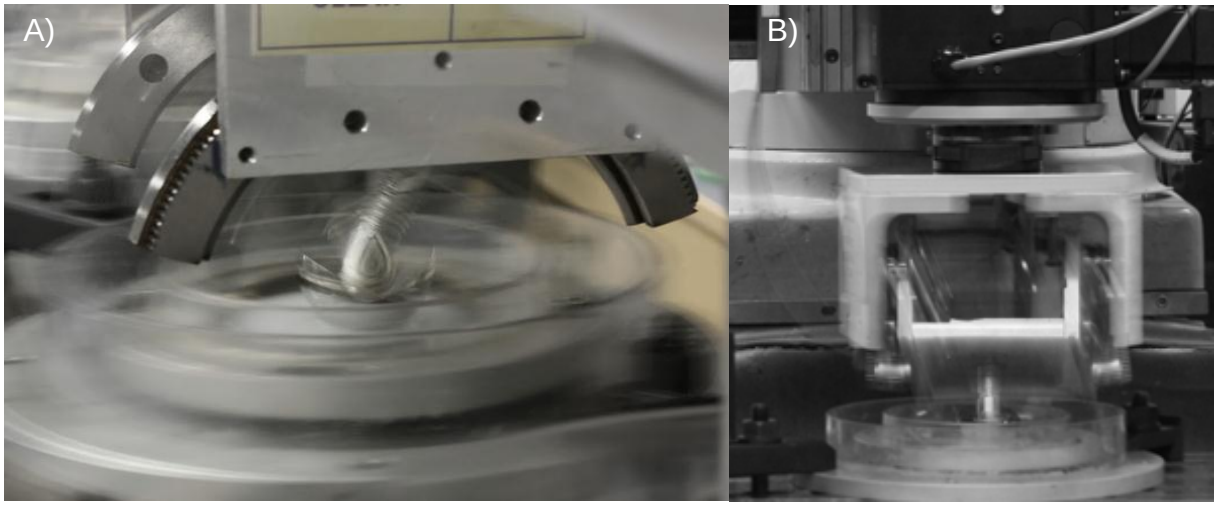

Figure 23: Long exposure photographs demonstrating the sliding, rolling, and rotation motions. A) Linear sliding with rolling and no rotation. B) Linear sliding with rolling and rotation.

The loading and motion are controlled with a custom LabVIEW code (National Instruments, Austin, TX) that also collects and records various data during the test, including the load at each station, number of cycles, room and lubricant temperature, and frictional forces. Any type of path can be programmed in, such as circular translation, square, or a “figure 8.” The computer uses an 8-axis stepper/servo motion controller PCI card (NI PCI-7358) to interface between the LabVIEW code and the servo motors, which are powered with the original amplifiers from the CNC machine. The code uses feedback from the load cells on each station to independently adjust the load with the electropneumatic transducers and a PID control algorithm. A 16-bit, 16-channel DAQ card (NI PCI-6251) collects data from the 6-axis lead cell and the current load through each motor. Additional control and data collection is achieved with a CompactDAQ chassis (NI cDAQ-9172) fitted with several modules: a 4-channel wheat-stone bridge module (NI 9237) to measure the signal from the 1-axis load cells; a 4-channel thermocouple module (NI 9211) to measure the temperatures of the motor casings, serum, and room; a 16-channel analog output module (NI 9264) to control the pressure transducers, and a 32single/16double-channel analog-to-digital module (NI 9205) to measure the home signal from the hall switch on the rotary table and the output signals on pressure transducers attached to each pressure segment of the pneumatic segments. The temperatures on the CNC servo motors and the normal loads on each station are monitored throughout the test and a warning can be emailed out if these ever drift into an unacceptable range.

To date, the Multidirectional Tribo-system has performed about 2,000 hours of wear testing for research, in addition to weeks of component testing and performance verification, and has proven to be reliable and versatile.

2.2 - Wear test parameters and procedures

This research was the first experiment to utilize all directions of the system's motion, so kinematics were chosen that represented the extreme minimum and maximum values of what is seen *in vivo*. The other testing parameters were selected to be the most physiologically relevant that the system could provide (Figure 24).

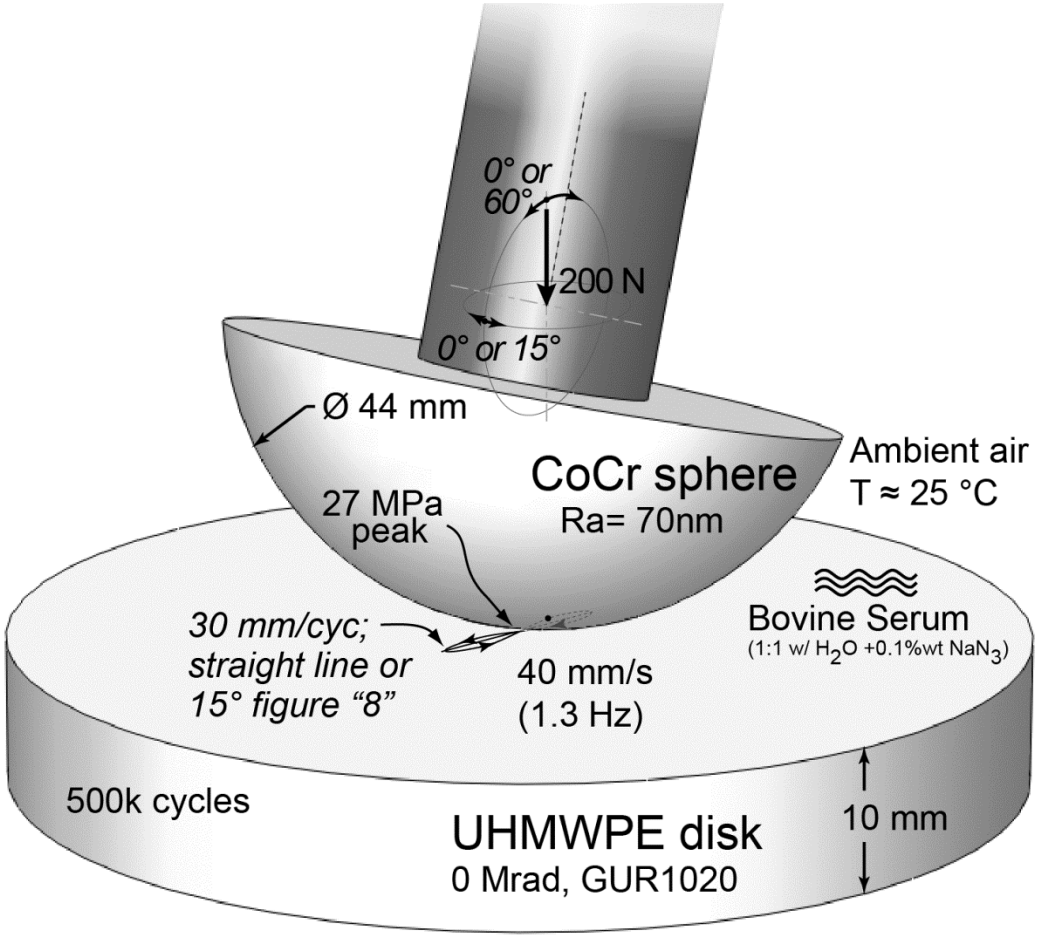

Figure 24: Wear was tested under eight different motion combinations of sliding, rolling, and rotation, using a custom multidirectional tribo-system to simulate physiologically relevant conditions. Motion paths and dimensions relative to contact conditions are drawn to scale.

Ultra-high molecular weight polyethylene (polyethylene) disks were machined from rods of unirradiated, compression molded, GUR1020 resin (Smith & Nephew, Memphis, TN). The disks were 89 mm in diameter and 10 mm thick. This thickness is similar to what has been traditionally recommended in hip and knee implants (Bartel et al. 1986) and minimizes the stress increases from the much stiffer metal supporting it. Machining marks were removed with wet

sanding, working up from 600-grit to 1200-grit. Average roughness values (R_a) were between 0.20 and 0.40 μm, with a skewness (R_{sk}) of -0.1 to -1.

Cobalt-chrome (CoCr) humeral heads were used as the metal spherical counter-bearing material. The implants, "New Shoulder Humeral Head," (Tornier, France) were received polished and fit for human implantation. They conformed to ASTM standard F15-37, which specifies the chemical, mechanical, and metallurgical requirements for wrought cobalt-28chromium-6molybdenum alloys used for surgical implants. The heads had a spherical diameter of 44 mm, a thickness of 17 mm, and a 3° female taper fitting with an offset of 1.5 mm. Average roughness (R_a) values were less than 0.07 μm. This is equivalent to the implantation roughness of CoCr components for hips and knees. Care was taken not to scratch or damage the CoCr surface before or after the tests.

The wear path on the polyethylene disks was either linear reciprocating, for no cross-shear, or a "figure 8," for specific crossing angles of cross-shear. The curvature of the "figure 8" path was a modified lemniscate of Bernoulli, scaled such that the interior crossing angle was either 0 degrees (a straight line) or 15 degrees. Typical crossing angles in the knee have been reported between 4 and 9 degrees (Hamilton et al. 2005), so these represent the minimum and extreme scenarios. In all cases, the total path length per cycle and cycle frequency were kept at 30 mm and 1.33 Hz, respectively, for a linear path speed of 40 mm/s. Path lengths of 20-30 mm per cycle are typical for knees. Walking speeds are approximately 1 Hz; slight increases above this frequency have been shown to produce equivalent wear rates.

The wear path on the CoCr spheres was either stationary or linear reciprocating using a rolling motion. The rolling motion was produced by a rotation about the axis through its center of curvature, parallel to the polyethylene disk surface, and predominantly perpendicular to the primary axis of disk motion (the axis of rolling was connected to the rotation motion). To accurately achieve this motion, the mounted bracket for the rolling mechanisms was carefully adjusted using a laser, such that the center of curvature of the rails was aligned with the center of curvature for the sphere, and the contact point of the bearing surface moved less than 0.005 inches as the carriage was moved through its 90° range of motion. The slide-to-roll ratio (S_n) between two surfaces is defined in terms of their mean and sliding velocities (Van Citters 2006):

$$S_n = \frac{V_s}{\bar{V}}, \qquad \text{eq. 42}$$

where $\bar{V}$ is the mean velocity:

$$\bar{V} = \frac{V_{CoCr} + V_{UHMWPE}}{2}, \qquad \text{eq. 43}$$

and the V_s is the sliding velocity:

$$V_s = V_{CoCr} - V_{UHMWPE}\,, \qquad \text{eq. 44}$$

A 60° range of motion of the sphere results in a sliding speed of 60 mm/s and a slide-to-roll ratio of 0.4. Research on *in vivo* kinematics of prosthetic knees shows sliding/rolling ratios for walking are between 30% and 42% (McGloughlin & Kavanagh 1998; Reinholz et al. 1998).

The other motion replicated was rotation. The recommended kinematic motions in the ISO knee prostheses wear testing standard were used to determine a realistic value for rotation

rate (International Standards Organization 2004). The ratios for A-P sliding to I-E rotation were typically around 0.4 to 0.8 degrees/mm, but about 20% of the gait was at 1.3 degrees/mm and the last 10% was at 5 degrees/mm. A ratio of 1degree/mm was chosen, which requires 15 degrees of rotation from one side of the wear path to the other. Thus, a crossing angle of 0 or 15 degrees, a slide-to-roll ratio of 2 or 0.4, and a rotation-to-sliding ratio of 1 degree/mm represented the minimum and approximate maximum of the *in vivo* cross-shear kinematics. Three variables with two options for each yield eight different combinations of motions (Table 4).

Table 4: Combinations of motions used to create a range of cross-shear conditions. Symbols ○/● indicate absence/presence of that type of cross-shear.

Test combo #	2D sliding 15° "Fig 8"	Rolling Slide-to-roll: 0.4	Rotation 1 °/mm	: Motion type : Kinematic value
1	○	○	○	
2	●	○	○	
3	○	●	○	
4	○	○	●	
5	●	●	○	
6	●	○	●	
7	○	●	●	
8	●	●	●	

Peak contact pressure in knee prosthesis can be as high as 30-45 MPa during flexion (Bartel et al. 1986; Morra & Greenwald 2005), but during gait the contact pressure are lower and laboratory wear tests for polyethylene often use a peak contact pressure closer to 15-20 MPa (Van Citters et al. 2007; Saikko & Calonius 2002). In the 1990s, TKR designs commonly exceeded peak contact stresses of 30 MPa, even at extension (Postak et al. 1998) but delamination of oxidized implants prompted manufacturers to increase conformity (AAOS 2000a; Brown & Bartel 2008). Now that manufacturers know how to better sterilize and store their implants, oxidation is much less common, although some concern remains (B. H. Currier et al. 2007; Atwood et al. 2011). The current trend may be toward less conforming implants (and higher contact stresses) now that some studies have shown that decreasing contact areas (with contact stresses up to 30 MPa) can lower wear rates (Galvin et al. 2009).

For these experiments, a load of 200 N was used to reach an initial peak contact pressure of 27 MPa and a mean contact pressure of 18-19 MPa (Figure 25A). The area of contact is approximately a circle with a radius of 1.8 mm. These contact mechanics were estimated using finite element analysis (Abaqus 6.9) of elastic/linearly plastic contact under static, un-worn conditions, using the implicit, dynamic solver setting. The ball was modeled as a rigid indenter only capable of vertical translation. The disk was divided into approximately 100,000 hexahedral elements with the material properties shown in Table 5, and the lower face of the disk was fixed in all displacements and rotations. These results matched well with observations from the wear testing; the width of a wear scar after about 100k cycles of a low wear rate (1D sliding) was about 4.2 mm. To estimate how the contact pressure would change during the test as the wear scar develops the contact condition were also modeled with a representative wear scar (a spline

about 6-mm wide and 90-µm deep, representative of about 200k cycles of a higher wear rate, such as 2D sliding + rolling) removed from the polyethylene disk. While the peak contact pressure was initially above yield, the contact pressure dropped to just below yield after a decent wear scar had developed (Figure 25B). Additionally, the contact pressure distribution shifted to become wider and have two peaks. The peak contact pressure dropped to 19.2 MPa, and the mean contact pressure dropped to 15.6 MPa. The center contact pressure was about 3% lower than the peak contact pressure.

Table 5: Material properties used for finite element contact analysis (Atwood 2010). The polyethylene response was modeled as bi-linear. The ultimate strain value is the additional strain beyond yield.

E	380	MPa
ν	0.46	$-$
ρ	935	$\frac{kg}{m^3}$
σ_y	22.3	MPa
σ_u	118	MPa
ε_u	0.0235	$-$

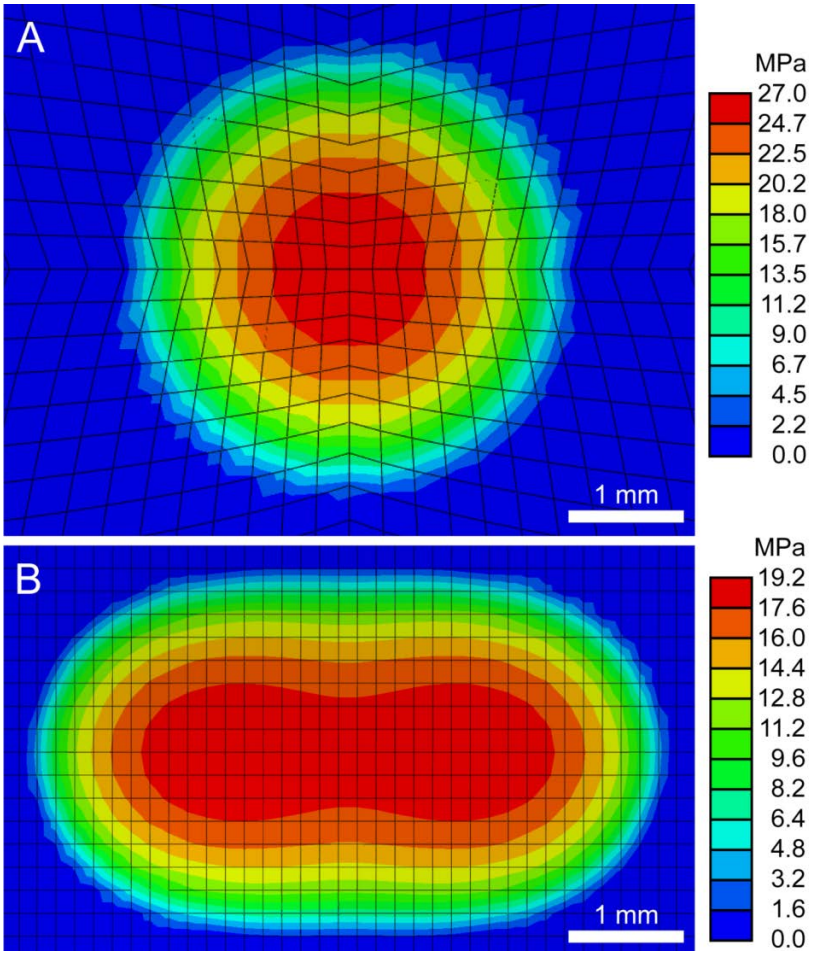

Figure 25: FEA of contact pressure under non-sliding conditions for A) initial contact without a wear scar, and B) contact after approximately 200k cycles at a relatively high wear rate, the visible wear scar is as wide as the image.

The lubricant for the wear testing was dilute bovine serum (Alpha Calf Fraction w/Iron, HyClone, Fisher Scientific part# SH3007603). The serum was diluted 1:1 with de-ionized water for a final albumin protein concentration of 10 mg/ml. To prevent bacterial growth, 0.1%wt of sodium azide (NaN_3) was added to the solution. The lubricant was stored in a refrigerator until needed.

Prior to every test, polyethylene and CoCr bearing surfaces were cleaned using a sonicator and de-ionized water with laboratory-grade detergent, and rinsed using several changes of de-ionized water, acetone, and propanol. Once cleaned, the components were wrapped in clean Kimwipes and only handled with clean gloves. Components were then mounted in their respective holders and aligned with a fresh wear path location. The location and orientation of each sample were noted so that the exact same wear path could be continued after pauses in the test for wear measurements. The lubrication well was filled with 20 ml of serum solution, and cleaned thermocouples were positioned to monitor the serum temperature. The LabVIEW code running the machine was set-up with the necessary parameters for controlling the motion paths and air pressure and measuring the loads and temperatures, which were recorded every 5-15 minutes. Initially, testing was paused approximately every 100,000 cycles (once per day) to measure the profile of the wear scar on the polyethylene and replace the lubricant. Testing was concluded after at least 500,000 cycles. The final wear profiles were measured again at least one month later to account for creep during the test.

2.3 - Measuring Wear

As most bearings systems are designed to minimize wear, the main difficulty of tribological testing is that the amount of material that has worn away is very low; tests need to run for a long time in order to generate any amount of discernible significant difference. There are two main ways to measure the amount of wear: volumetric and gravimetric. The volumetric method measures the change in the sample's volume, either looking at the profile of a wear scar on a sample such as a flat disk, or looking at the diameter of the worn area on a hemispherical-tipped pin. It can be challenging to get accurate measurements with this method for viscoelastic materials since some of the dimensional changes are only due to creep and not material removal. The gravimetric method measures the change in the weight of the sample before and after the test, which can be converted to a wear volume using the material density. Accurate measurement with this method is challenging for materials that can absorb moisture during the test, or otherwise gain or lose weight for reasons not related to material removal. Ultra-high molecular weight polyethylene is a viscoelastic material that also absorbs a small amount of fluid, making it difficult to accurately measure the wear via either method. For ease of use and lower variability, wear was primarily measured volumetrically.

For the volumetric method, the depth profile across the middle of the wear scar (Figure 26) was measured using white-light interferometry (ADE, MicroXAM-100), which gives XYZ

data for a small area of a surface. The largest scan area with this machine is 2.6 mm x 1.8 mm, so several scans had to be stitched together in Matlab (Mathworks, Natick, MA) to cover the entire wear cross-section and the unworn section on either side (Figure 27). The middle of the "figure 8" wear scars were easy to identify, but to ensure the measurement profiles of the 1D sliding wear scars were taken at a consistent location, a small mark was scratched into the polyethylene disk a few millimeters outside of the wear scar. The calibration of the instrument was verified before each use. The way polyethylene defuses and reflects light makes it difficult to image and the noise threshold was lowered to 0.3, which allowed for measurements with enough data that they were repeatable and could be reliably stitched together but without high levels of noise that would affect the measurement. Vision32 software (Veeco, Tucson, AZ) was used to interpolate between the small areas of missing data and correct for surface tilt using the unworn areas on either side of the wear scar (Figure 28). The wear profile, running perpendicular to the main axis of motion, was averaged along a 400-μm-wide line to ensure repeatability and filter out noise (Figure 28). This profile was exported to a *.csv file and, using a custom Matlab code, the edges of the wear scar were detected and the area in between was numerically integrated to determine the total wear volume, per unit scar length. The linear wear rate was calculated using a line fit through the data points in the steady-state region (following an initial "bedding-in" period due to creep of about 100,000 cycles) (Figure 29). To account for the creep response of polyethylene, the wear volume was measured again several weeks after the test had ended (strain-recovery was quickest in the first few days but had ended after 3-4 weeks, with an average recovery of 10-50% of the wear volume). In initial wear tests, the linear wear rates calculated using just this strain-recovered wear volume and the total number of cycles were generally less than 20% higher that the steady-state wear rate. Also, this wear rate was more consistent between tests than the steady-state wear rates. One set of wear tests, of 2D sliding both with and without rolling, was run out to more than 1.5 million cycles and no change in wear rate was detected. Due to the consistency between tests, similarity between methods, additional time needed to acquire steady-state measurements during the test, and consistency in wear rate out to a higher number of cycles, the next set of wear rates were only calculated based on the strain-recovered wear volume (Figure 30). The cross-sectional area of the wear scar was then used to calculate the wear factor based on eq. 7.

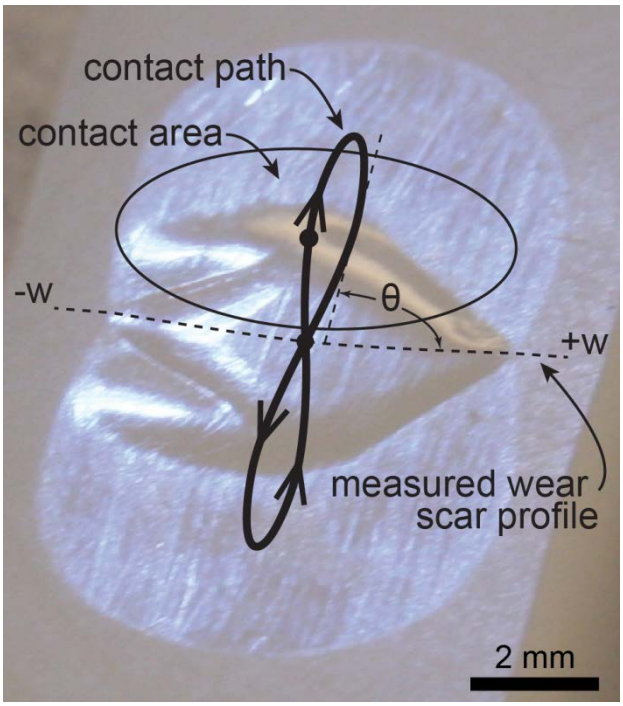

Figure 26: Picture of a wear scar after 540k cycles of rolling and cross-sliding, showing the sliding path of the contact point, approximate size of the contact patch, and the location for the profilometer measurements of the wear scar profile. When calculating the cross-shear, the sliding angle, θ, is measured counter-clockwise from the +w axis and constrained to fall between 0 and π.

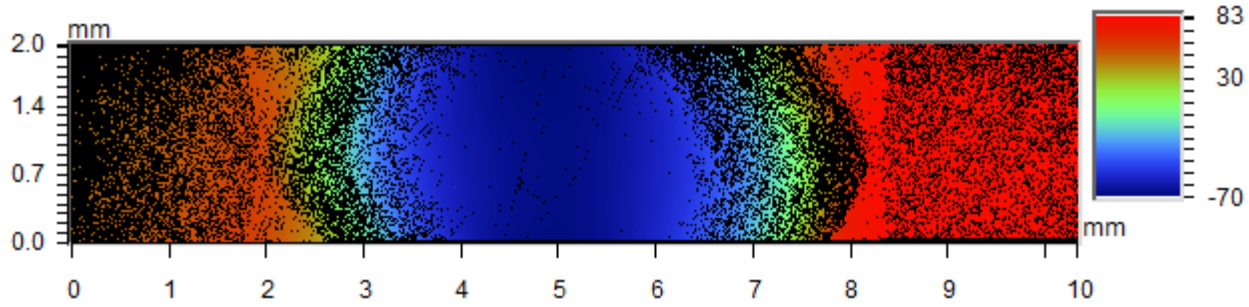

Figure 27: Several measurements on an optical profilometer stitched together into one image. Color scale bar is in µm.

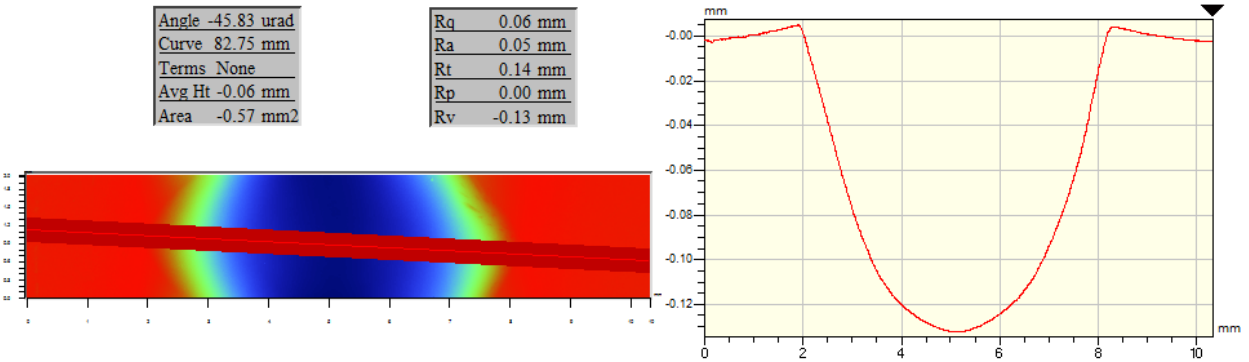

Figure 28: The data fall-outs in the measurement are interpolated and the depth, averaged along a ~300µm width, is profiled across the center of the wear scar.

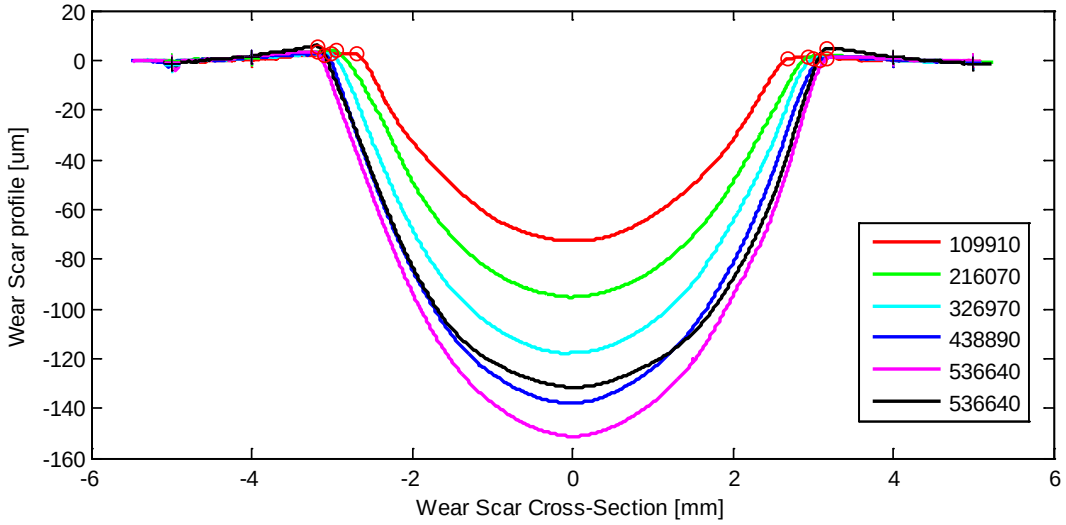

Figure 29: Example of how the wear profile progresses during a test (legend shows the number of total number of cycles at each measurement), and then recovers following a resting period of 51 days (black line).

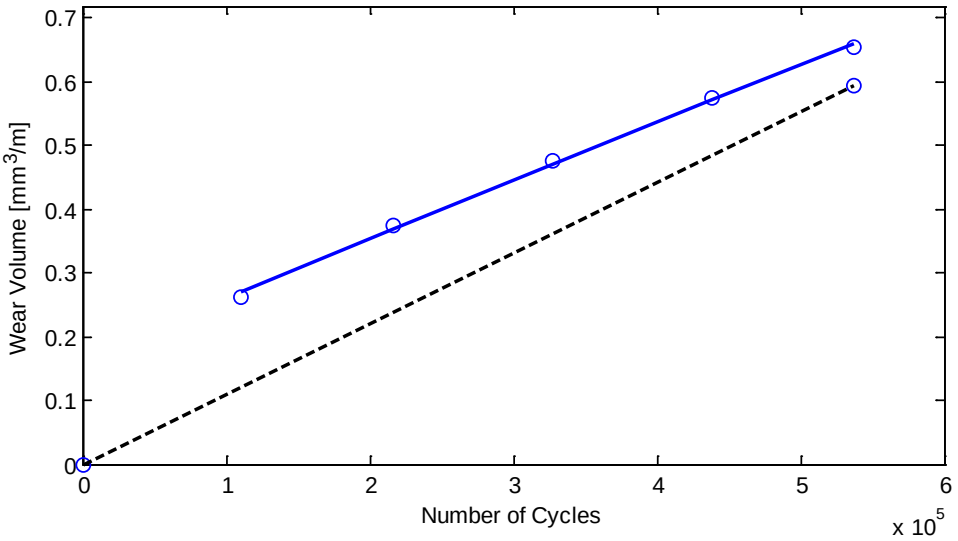

Figure 30: Example of how the wear volume progresses during a test (blue line). The steady state wear rate (black dashed line) was very similar to the wear rate based on the creep recovered volume loss.

2.4 - Analyzing Microstructure Changes

Wear in polymers is sensitive to the type of motion at the surface because of how the shear forces can orient the lamellae at the surface. To analyze how the different motion combinations affected the microstructure at the wear surface, samples were chemically etched to remove the amorphous phase, and imaged with a scanning electron microscope (SEM).

The samples of the wear surface were taken from the bottom center of each wear scar and were 3 mm x 3 mm wide and 10 mm thick. Control samples were also taken from the unworn

areas next to the wear scars. To observe the microstructure in the near- and subsurface regions, the wear samples were sectioned with a razor and prepared with a microtome to reveal a surface perpendicular to the sliding surface and aligned with sliding direction (Figure 31).

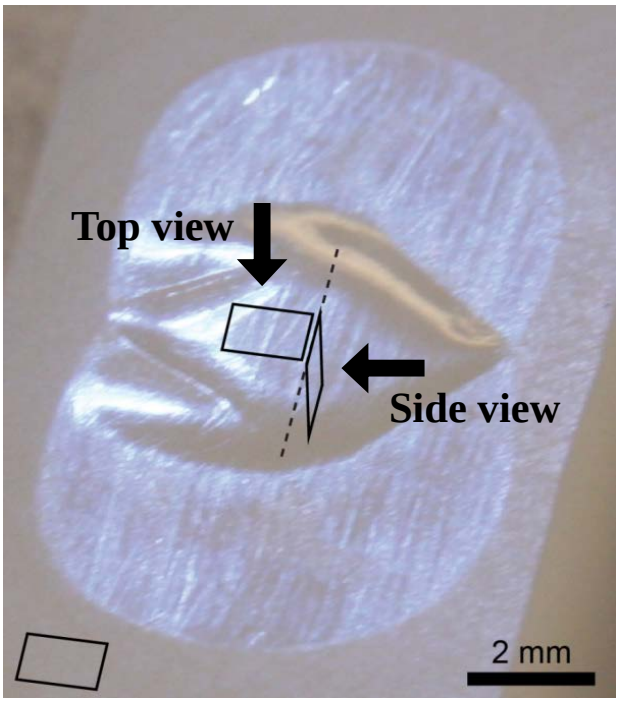

Figure 31: The microstructural evolution of the wear samples were examined from a top view looking down on the wear surface and at from a side view at different depths below the wear surface. These were compared to the microstructure of non-worn areas of the disk.

The surfaces of interest were then submerged in an acid solution that would preferentially etch away the amorphous phase of the polyethylene, leaving behind the lamellae at the surface. The acid solution was 66.7%v sulfuric acid, 26.7%v ortho-phosphoric acid, and 6.7%v deionized water, with 1.34 %w of potassium permanganate (Olley & Bassett 1982). Once the solution was carefully combined (to a final volume of 100 ml), it was stirred for 1-2 hours to fully dissolve the potassium permanganate. The wear samples were sequentially cleaned with soap, DI water, acetone, and propanol in a sonicator. They were then held suspended in the etching solution such that the wear surface was fully submerged. Samples too small to hold directly were epoxied to metal pins such that the surface of interest was completely exposed and the sample could be fully submerged. After 1-1.5 hours in the etching solution, the samples were removed and consecutively rinsed with sulfuric acid, hydrogen peroxide, deionized water, and acetone. A 1-mm thick slice of the surface of interest was carefully sliced off of each sample with a razor and prepared for SEM imaging by sputter-coating a thin layer of gold-palladium (Tousimis Sputter Coater, Rockville, MD). SEM images were taken at 10,000-40,000x magnification and 10kV of accelerating voltage to yield a resolution of 8.8-2.2 nm (Hitachi S- 5000, Tokyo, Japan).

The resulting images were analyzed for differences using a custom image analysis code written in LabVIEW (National Instruments, LabVIEW v8.5). The user loads in a grayscale SEM image, selects a threshold brightness value for converting the image to black & white and

defining the edges of lamellae, and then applies several standard filters to isolate individual lamellae (Figure 32). The thesholding sensitivity is controlled by “Power x value” setting, which the user adjusts as needed, and then the program performs an auto-thresholding using the inter-class variance method, which determines an optimal threshold by maximizing the between-class variation with respect to the threshold. The first set of filters cleans up the noise in the thresholded image in three steps: morphological transformation of the white objects with at least 14 dilations and erosions of the “pclose” transformation; a “fill hole” transformation that removes the noise within the objects; and then a removal of all objects below a certain size threshold, typically 1% but adjusted based on the magnification level of the image. The remaining objects were considered to be all of the lamellae edges. The second set of filters removed objects that would not yield a representative or accurate orientation angle measurement: objects touching the edge of the image were removed as these portions may not be representative of the full lamellae; objects with a small ratio of equivalent rectangle side values or elongation factors were remove since they were either too stout to be clear representations of lamellae or too curly to determine the orientation of; and large groups of lamellae that the previous filters were not able to recognize as individual lamellae were removed if they did not fall within the user-defined perimeter limitations. This process produced well defined lamellae from most images, but for some images the procedure and settings had to be adjusted at the discretion of the user in order to identify the representative lamellae.

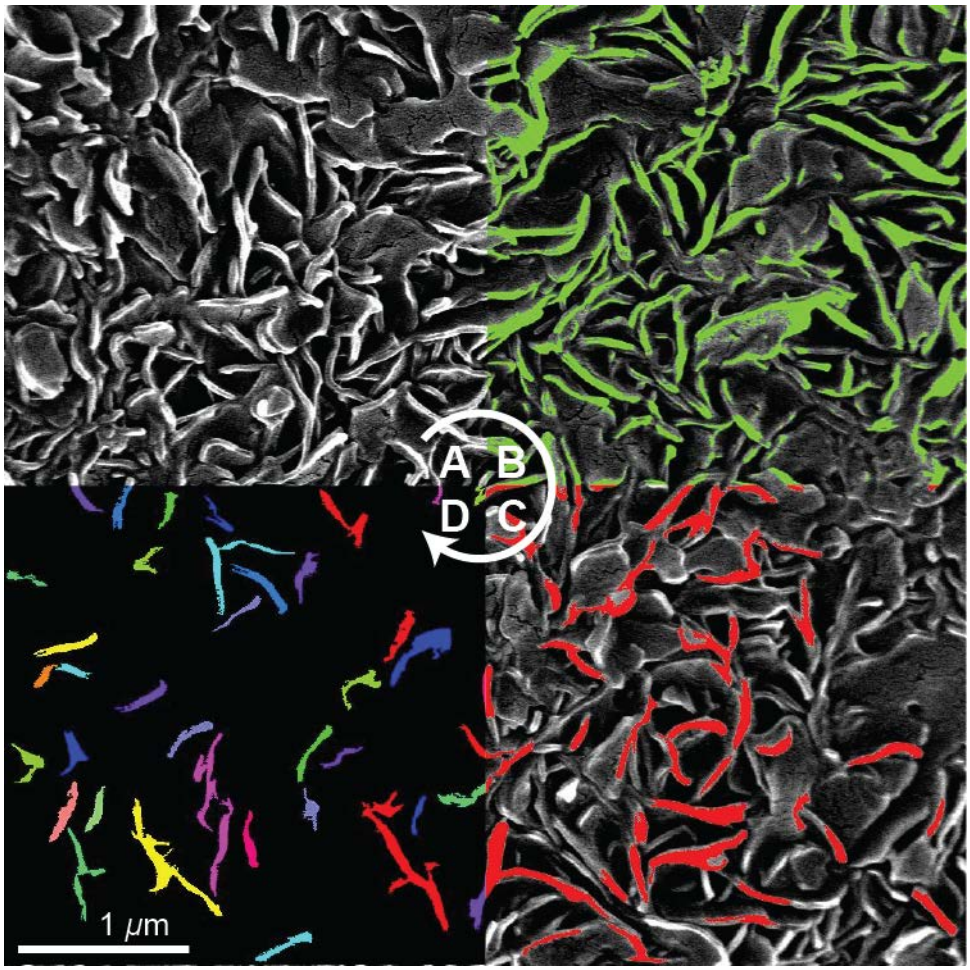

Figure 32: The steps of the image analysis procedure used to quantify texture development, demonstrated on the four quadrants of an SEM image of the etched microstructure. The original image (A) was thresholded to pick out the lamellae edges (B, highlighted in green) and then lamellae that were touching the edge or combined with other lamellae were filtered out (C, highlighted in red) and the angle of the major axis for all the remaining lamellae (D) was calculated.

After the threshold and filtering, the main axis of orientation for each lamella was calculated by determining the axis which minimized the area moment of inertia. The angles were defined such that all lamellae orientations lay between 0 and 180 degrees, where 90 degrees was the direction of sliding and expected alignment orientation. This definition results in both a fully aligned microstructure and a fully random microstructure having the same average alignment angle, but very different distributions. The standard deviation of orientations of all lamellae in each image was compared across the different samples and locations to find trends. The threshold technique only identifies the edges of the lamellae and assumes the rest of the lamella is perpendicular to the surface. To account for texture evolution that would orient the lamellae parallel to the surface, the percentage of image area that was detected as a lamellar edge was used (after the threshold step and the first three filters: morphological transformation, fill hole, %area; approximately half-way between Figure 32B&C). This approximation for parallel alignment assumes that the lamellar size distribution and crystallinity is equivalent between the

samples and that more alignment of lamellae parallel to the surface leads to fewer edges detected.

Orientation in the microstructure was also analyzed using an image fast Fourier transform (FFT) of the original microstructure image. The 2D image FFT analysis tool in LabVIEW analyzes the frequencies present in the image by running an FFT to convert the distance-brightness waveform of many lines than run through the center of the image into the frequency-brightness domain. The brightest and longest lines across the resulting image indicate that lamellae edges were more often crossed in that direction than in the other directions, suggesting an alignment of lamellae perpendicular to this line (Figure 33).

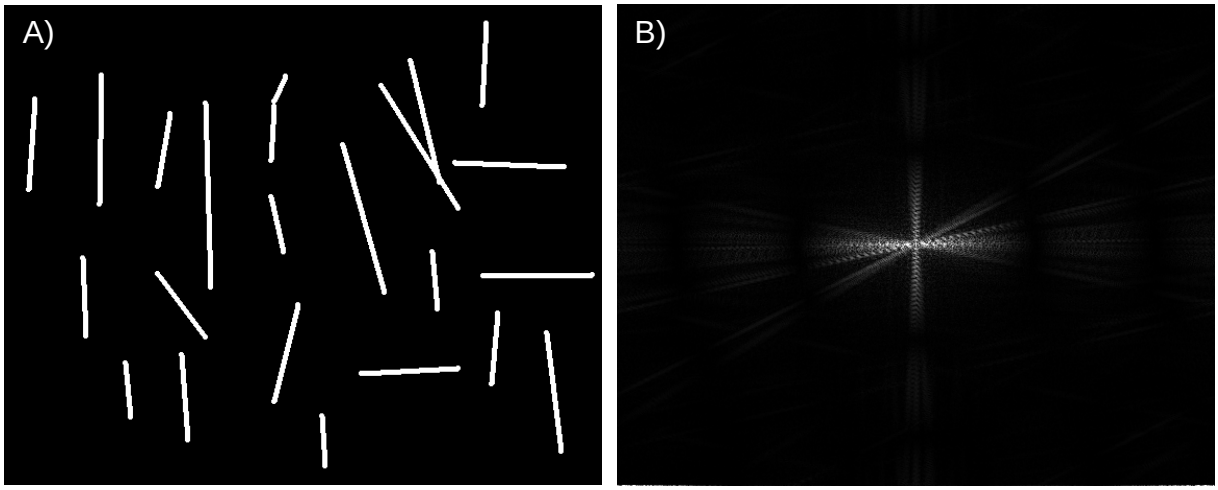

Figure 33: Orientation in the microstructure was also quantified using FFT. This test image shows how clear orientation in one direction (A) would produce a pattern which becomes clearly evident on the FFT result (B) as a bright line perpendicular to the direction of orientation.

2.5 - Calculating Tribological Intensity and Cross-shear

The cross-shear parameters presented in the section starting on page 16 were calculated for each wear path using numerical methods. The central cross-section of the wear path (same cross-section as the measurement location in Figure 26) was divided into $N_w = 101$ elements (each 70 µm wide) across the width of the sliding area, and the relative slip velocity and contact pressure at each element were calculated every 0.001 seconds. Results for non-memory-based parameters with these settings were within 0.05% of results calculated with 1001 elements and a time step of 0.0001 seconds, except the total sliding distance, which was within 1% (the memory-based parameters were not calculated at this higher setting). The slip velocities were calculated using vector addition of the disk sliding velocity, sphere rotational velocity, and sphere rolling velocity (eq. 45, eq. 46, eq. 47, and Figure 34). Vector angles were confined to fall between 0 and π radians, measured counter-clock-wise from the +X axis (see θ_v in Figure 34). Since the contact area was relatively small compared to the radius of curvature of the spheres used, the rolling velocity was assumed constant along the cross-section. The contact pressure

was calculated using an elliptical fit to the FEA contact model (Figure 25) and the current position of the central contact point (Table 6).

$$\vec{v}_{relative} = \vec{v}_{sliding} + \vec{v}_{roll} + \vec{\omega}_{rot} \times \vec{r}_{i/c} \,, \qquad \text{eq. 45}$$

$$v_y = v_s \cos\theta_s - v_s \frac{2 - S_n}{2 + S_n} \cos\theta_c - \omega_{rot}(r_i - r_{cx}) \,, \qquad \text{eq. 46}$$

$$v_x = -v_s \sin\theta_s + v_s \frac{2 - S_n}{2 + S_n} \sin\theta_c - \omega_{rot}(r_{cy}) \qquad \text{eq. 47}$$

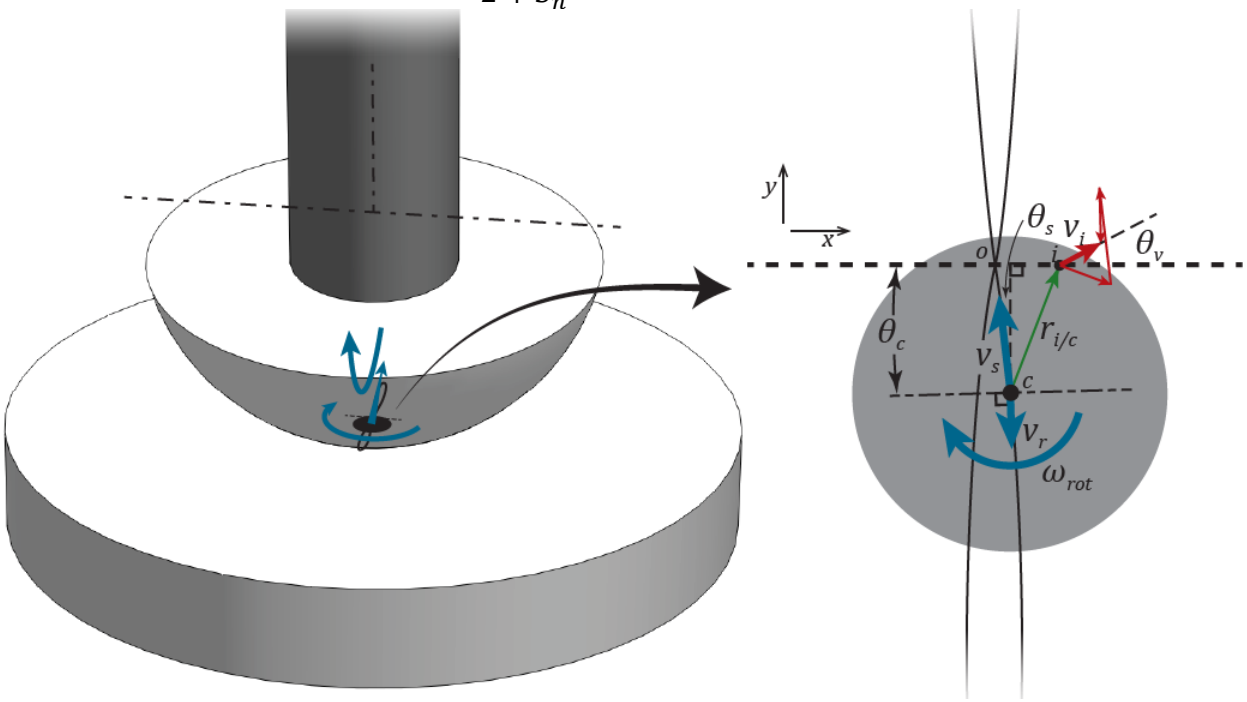

Figure 34: The relative slip velocity, v_i, for each element across the middle cross-section (thick dashed line) under contact (gray circle) was calculated by summing the tangential component of the rotational velocity at each location with the sliding and rolling velocities.

Table 6: Parameters for ellipsoidal pressure distribution

Peak Contact Pressure	27	MPa
Contact Radius	1.8	mm
Resultant Load	200	N

The tribological intensity and frictional work parameters at each time step were summed across the entire portion of the cycle where the cross-section was in contact, and then summed along the width of the cross-section. For example, the total frictional work expended at element *j* in one loading cycle is

$$W_{Tj} = \sum_{i=1}^{N_T} \mu P_{ij} v_{ij} \Delta t \,, \qquad \text{eq. 48}$$

and the total frictional work expended across the contact cross-section in one cycle is

$$W_T = \sum_{j=1}^{N_w} \sum_{i=1}^{N_T} \mu P_{ij} v_{ij} \Delta t \, \Delta w \, . \qquad \text{eq. 49}$$

Similarly, the cross-shear ratio at each element and the total cross-shear ratio are

$$CS_j = \frac{\sum_{i=1}^{N_T} \mu P_{ij} v_{ij} \sin^2\left(\theta_{ij} - \bar{\theta}\right) \Delta t}{\sum_{i=1}^{N_T} \mu P_{ij} v_{ij} \Delta t} \; ; \qquad \text{eq. 50}$$

$$CS = \frac{\sum_{j=1}^{N_w} \sum_{i=1}^{N_T} \mu P_{ij} v_{ij} \sin^2\left(\theta_{ij} - \bar{\theta}\right) \Delta t \, \Delta w}{\sum_{j=1}^{N_w} \sum_{i=1}^{N_T} \mu P_{ij} v_{ij} \Delta t \, \Delta w} \, . \qquad \text{eq. 51}$$

Since there are multiple complexities at the contact interface, such as varying lubrication film thickness across the contact area and increasing contact area as the wear depth increases, the cross-shear at each element should not be related directly to the corresponding depth of the wear scar at that location. Similarly, the cross-shear ratio should be the ratio of the total amount of perpendicular frictional work and the total frictional work, instead of the sum or average of the ratios at each element.

Chapter 3: Cross-shear Modeling

3.1 - Code development and validation

The effect of each type of motion on the frictional work and cross-shear can be best analyzed by looking at the variation in frictional power across the wear path as time progresses throughout a cycle. The simplest case is for the motion path with no cross-shear (Figure 35). The horizontal axes are the distance from the center of the wear cross-section (perpendicular to the wear path, along measurement path in Figure 26) and the time since the start of the loading cycle (not counting the time the center cross-section is not in contact). The loading cycle is simplified to only the two time intervals where the middle cross-section is being loaded: when the sphere crosses that point moving one way, and when it crosses it again coming from the other direction. Since the velocity is uniform, the only variation in frictional power is from the contact pressure distribution, resulting in two peaks in frictional work with symmetrical distributions across the wear scar and time.

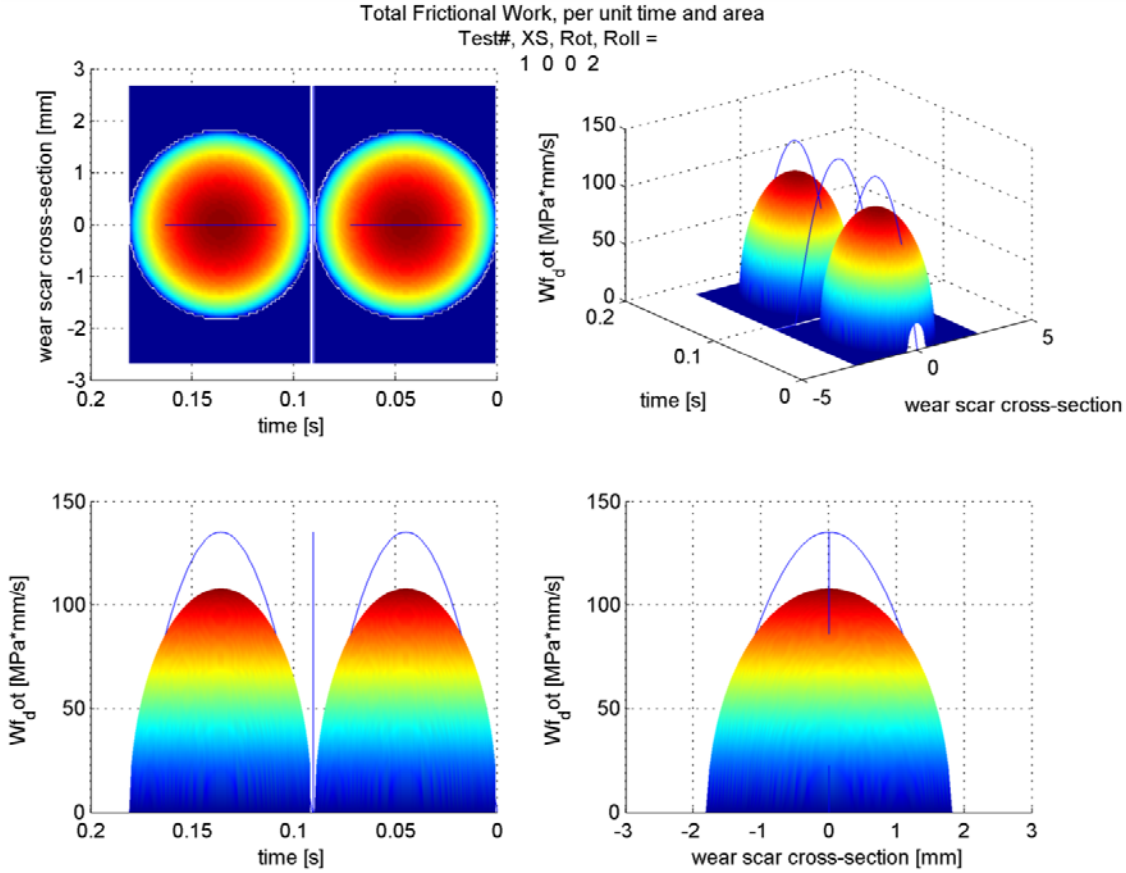

Figure 35: Distribution of the total frictional power, $\dot{W}_T$, for the no cross-shear condition: crossing angle = 0°, rotation = 0°/mm, roll-to-slide ratio = 2. Isometric and orthographic projections plotted across the wear

scar cross-section and as time progresses. The blue line is scaled the sum of the frictional power, either across the wear scar or across the cycle time.

The most complex case is when each cross-shear motion is present: crossing angle, rotation, and rolling. The total amount of frictional work expended is about 60% less than that for the no cross-shear case because the rolling of the sphere is in the sliding direction, and hence, the relative slip velocity and sliding distance is much less (Figure 36). The distribution of each contact instance is not symmetrical across time because it is sliding across the line at an angle; the $-w$ side will come in contact before the $+w$ side will, and the $+w$ side will remain in contact after the $-w$ side has lost contact. This distribution is the same for the second contact instance as well, since the sphere is moving in the $+w$ direction both times due to the shape of the "figure 8" sliding path. The peak of the distribution is not centered about the contact cross-section because of the rotation motion; the direction of rotation is such that it adds to the sliding velocity on the $-w$ side of the cross-section and subtracts from the sliding velocity on the $+w$ side and therefore the peak frictional work, a product of contact pressure and sliding velocity, occurs just slightly to the $-w$ side.

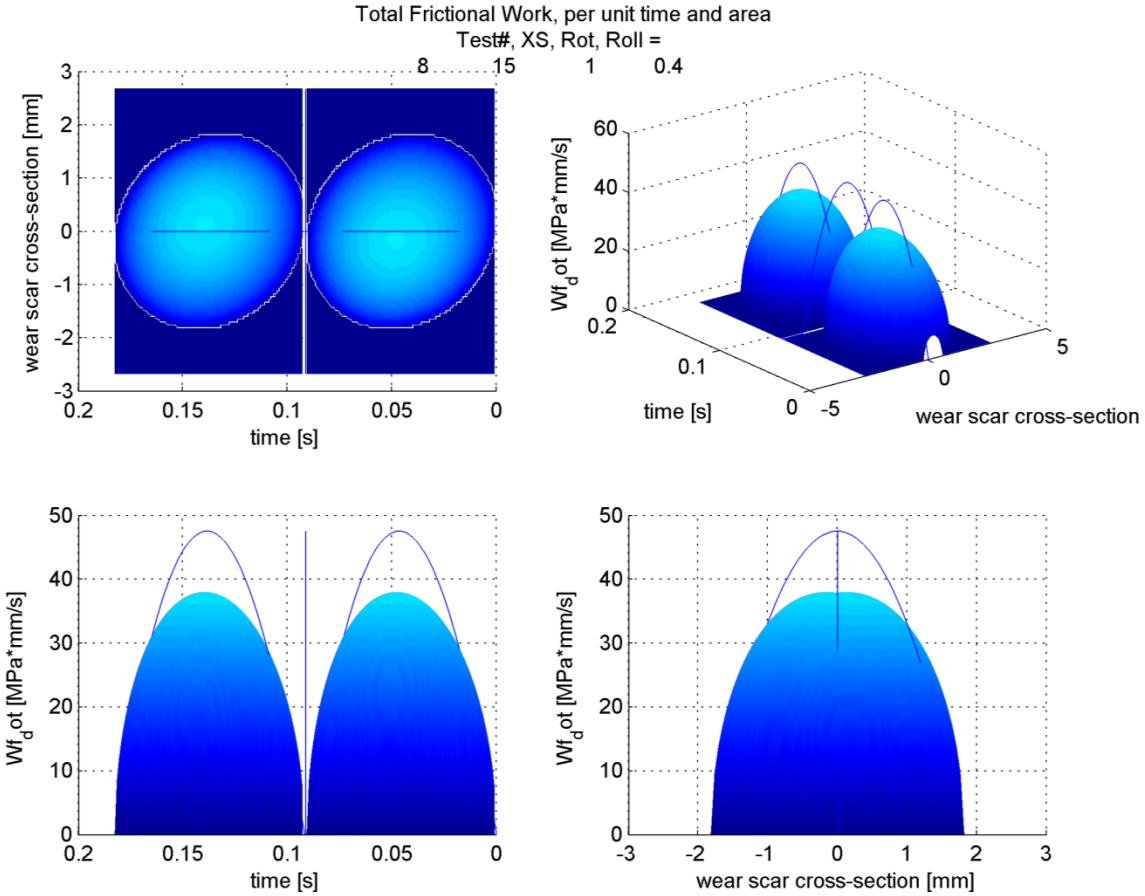

Figure 36: Total frictional power expended, $\dot{W}_T$, for the max cross-shear condition: crossing angle = 15°, rotation = 1°/mm, roll-to-slid ratio = 0.4. Same axis and color-scale as Figure 35.

The main parameter in calculating the cross-shear is the direction of sliding, which is determined by calculating the angle of the velocity vector. By convention this angle is defined to

be between 0 and π, since there is no evidence in the literature that motion in the reverse direction has significant effect on molecular orientation. For the simplest motion paths, the sliding angle is constant throughout the cycle, but the angle can vary significantly for more complex combinations such as “figure 8” sliding combined with rolling and rotation (Figure 37). The “figure 8” sliding path obviously has the greatest effect on changing the sliding angle between the two contact instances of the cycle. The rotation of the CoCr head will alter the velocity angle as the center of rotation slides over the wear scar cross-section, and the rotation component of velocity is either aligned with or perpendicular to the main sliding direction. This rotation also means one side of the track will have a higher magnitude of sliding velocity than the other. The rolling motion also has a significant effect on the sliding motion. Since the axis of rolling is aligned with degree of rotation and not the sliding direction, a slide-to-roll ratio of 0.4 means the forward component of velocity is decreased but the side component of the velocity is not affected. This increases the angle of the relative sliding velocity.

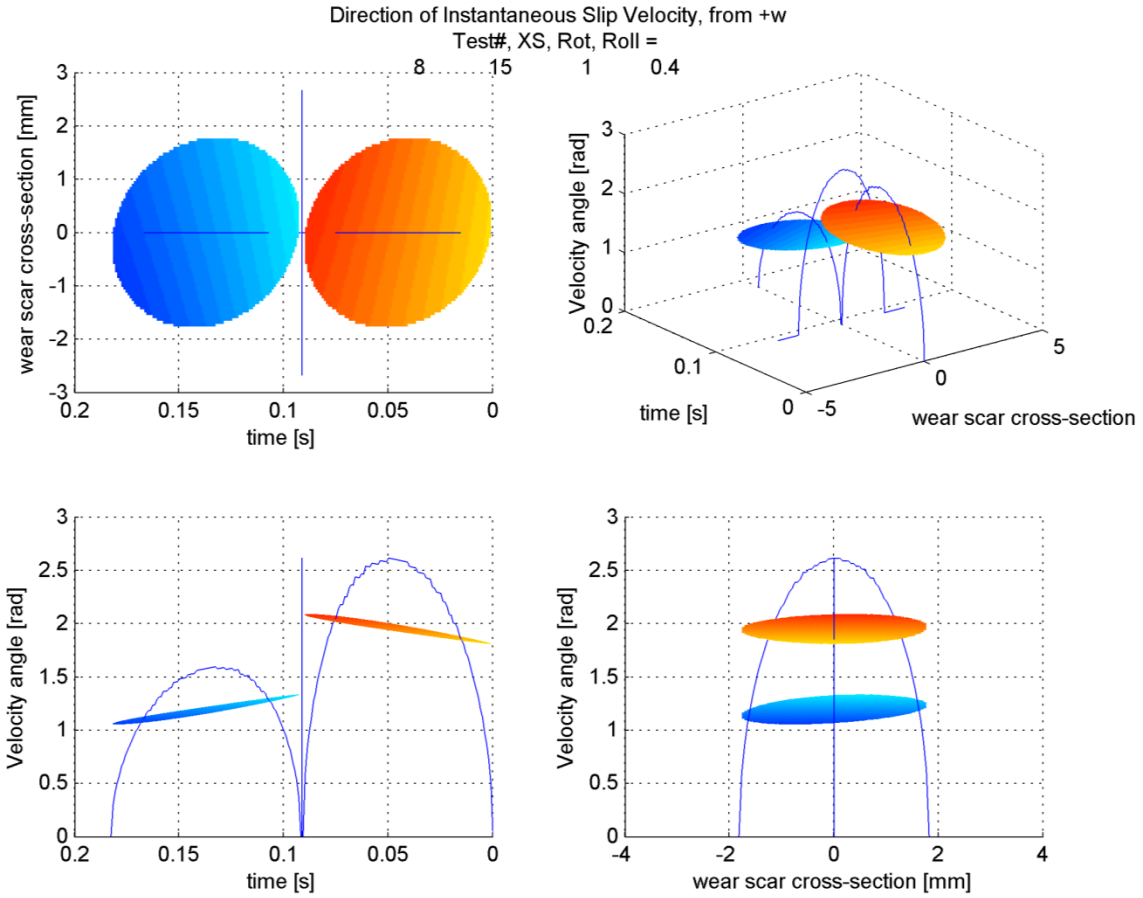

Figure 37: For combinations of motion, such as “figure 8” sliding + rolling + rotation, the sliding angle can vary significantly throughout the wear cycle and across the wear scar. For the first half of the cycle, sliding is to the left and rotation is clockwise. Angle convention is defined in Figure 26.

In order to use these sliding angles to calculate the perpendicular components of frictional work, a primary direction of molecular orientation must be defined for use as the base-line angle. The standard definition of the primary molecular orientation (PMO) is the baseline

angle that either maximizes the parallel component of frictional work or is perpendicular to the minimized direction. The PMO was found to be 90° for all motion combinations. For example, Figure 38 shows the how the parallel component of the frictional work was maximized for a primary molecular orientation of 90° and minimized at 0°, for all locations across the wear scar.

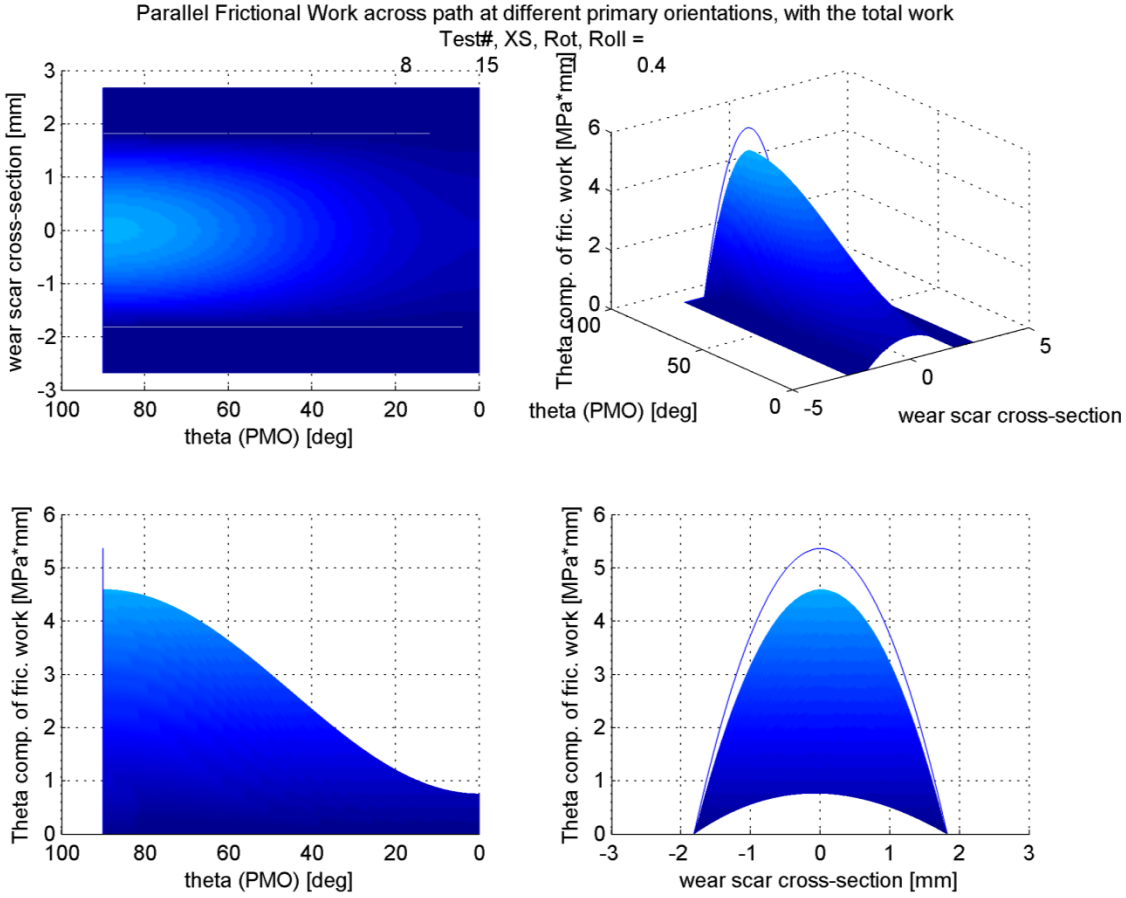

Figure 38: The parallel component of frictional work, $W_{\parallel}$, for “figure 8” sliding + rolling + rotation was maximized at a primary molecular orientation of 90° and minimized at 0°, for all locations across the wear scar. The blue line is the total frictional work at each location across the wear scar.

3.2 - Cross-shear variations during contact

The perpendicular component of frictional work is a function of both the sliding angle, the magnitude of the velocity (since it affects the sliding distance of each location), and the contact pressure distribution. Since the variations in velocity and sliding angle across the contact line are small compared to the variations in contact pressure, the elliptical distribution of the contact pressure dominates the distribution of frictional power. The effect of the magnitude and direction of the velocity vector is to skew this distribution toward the locations and times with higher sliding velocities and with sliding directions further from the primary molecular orientation. For example, in Figure 39, the peak is shifted later in the cycle because the rotation

direction is such that the velocity from rotation subtracts from the sliding velocity in the first part of the cycle but adds to it after the center of rotation has slid across the cross-section line. The peak is also slightly toward the left of the cross-section because the rotation velocity has a forward component on that side and a backward component on the other side. The rolling mainly decreases the forward direction of velocity and has little effect on the perpendicular component so the sliding angle is actually greater than it would be otherwise, increasing the relative component of frictional work in the direction perpendicular to the PMO. The effect of rotation is more evident in the pure rotation case (Figure 40). The only times frictional power is expended perpendicular to the PMO is before and after the center contact point passes the cross-section, even though these extremes are where contact pressure is smaller. Near this instant the center contact point passes the cross-section the rotational velocity components are mostly aligned with the PMO.

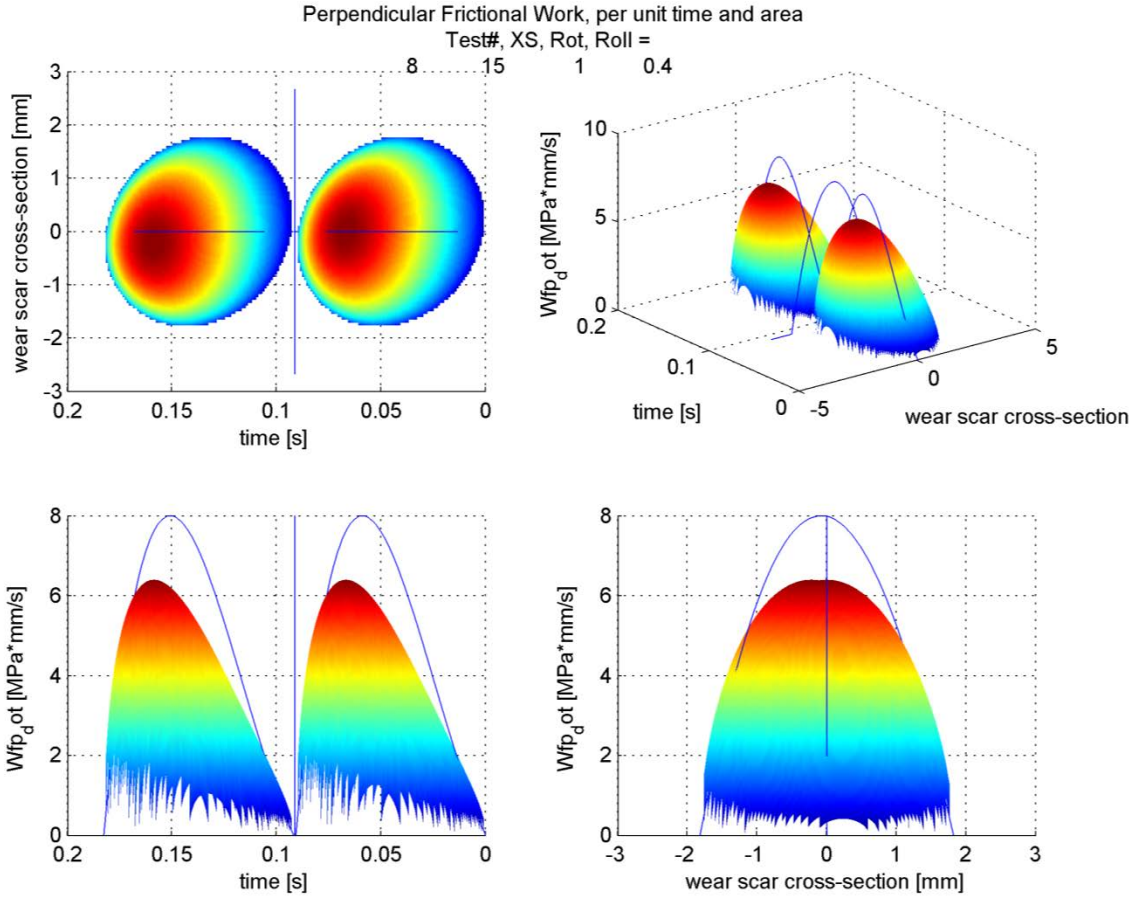

Figure 39: The distribution of the perpendicular component of frictional power, $\dot{W}_{\perp}$, for “figure 8” sliding + rolling + rotation. The peak is shifted toward the end of the cycle and slightly toward the -w direction because of how the velocity direction from the rotation adds to the sliding angle from the “figure 8” path.

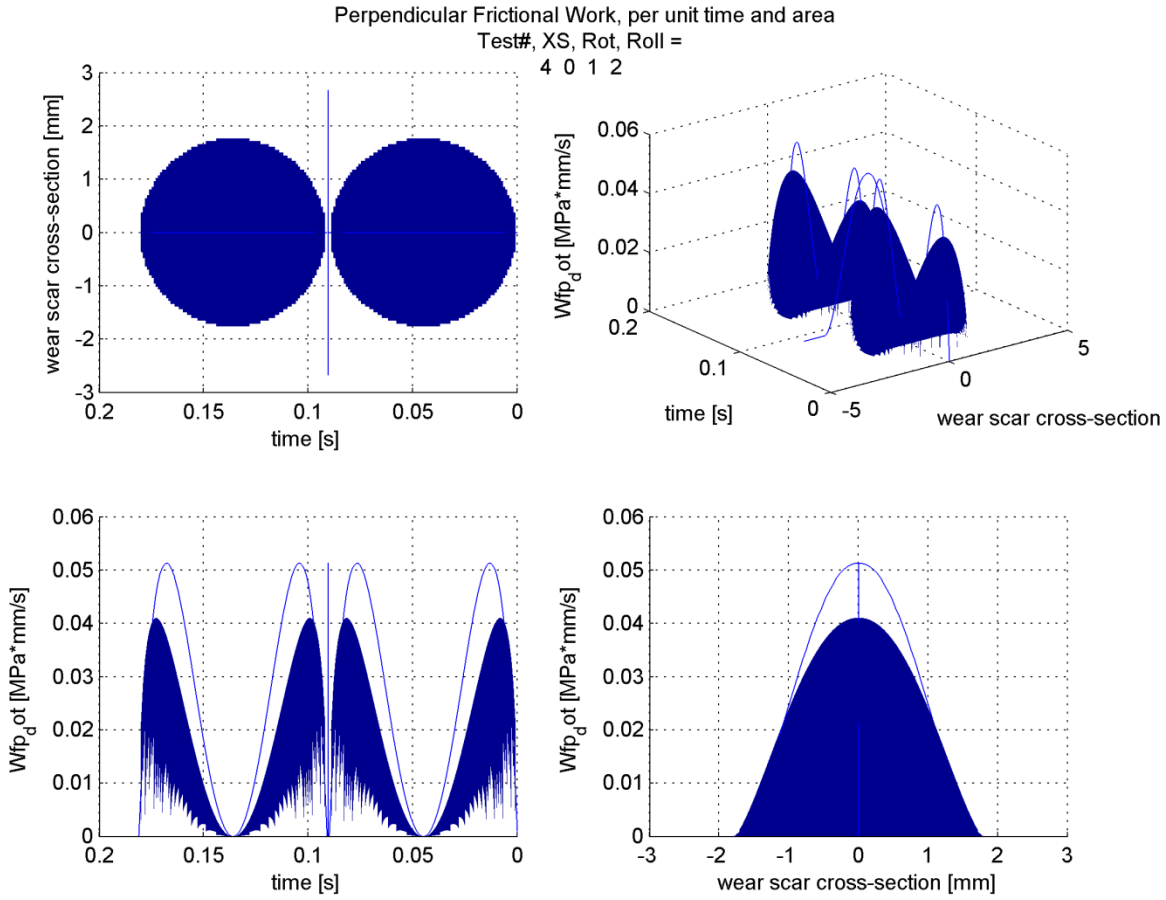

Figure 40: The distribution of the perpendicular component of frictional power, $\dot{W}_{\perp}$, for 1D sliding + rotation; same color-scale as Figure 39. The velocity angle is mostly aligned with the PMO at the times when the contact pressure is near maximum, resulting in a unique distribution. The magnitude of the frictional power, however, is much lower than other motion combinations.

During a wear cycle, the memory-based measures of cross-shear are greatest immediately following a change in sliding direction. For the 2D "figure 8" sliding scenario, this means the cross-shear is greatest at the beginning of each contact instance. This can be seen for Petrella's method, the cross-sliding intensity (eq. 29), in Figure 41; once the contact has slid in a constant direction for the length of the memory distance the molecules are considered completely aligned and no additional cross-shear takes place until another change in sliding direction. A similar trend is seen in Strickland's approach (eq. 33), except that the decay is exponential, not linear, and that a shorter distance for S_c is needed for a similar effect (Figure 42).

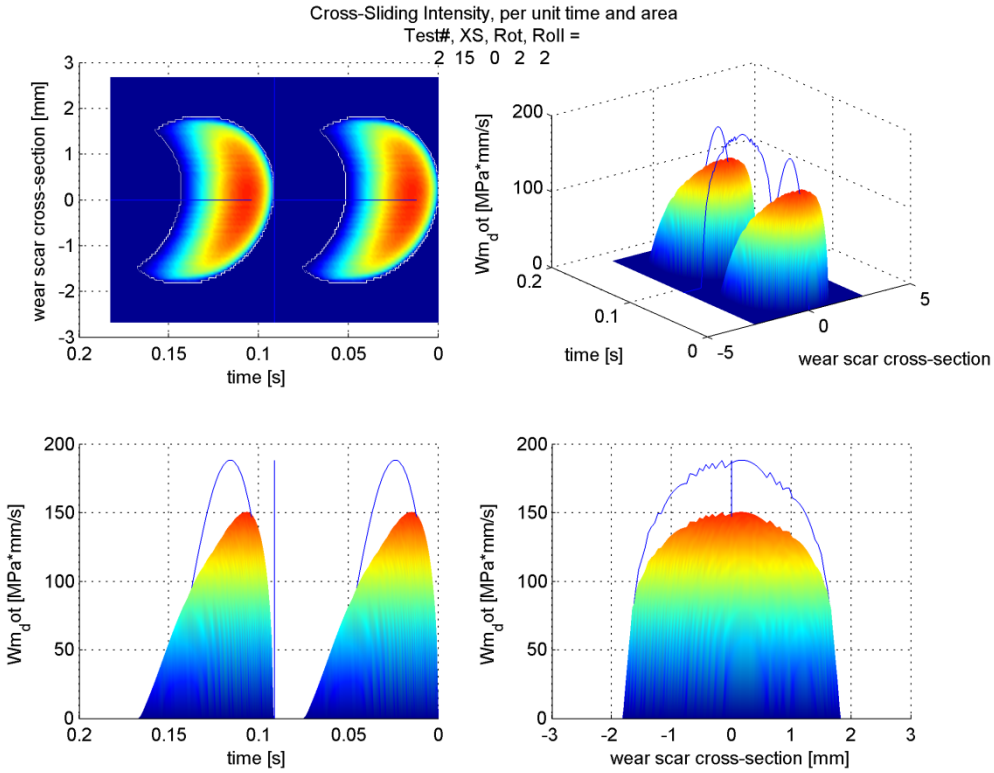

Figure 41: The rate of cross-sliding intensity, $\dot{W}_m$, for "figure 8" sliding, for a memory distance of 2 mm. (The slight jaggedness of the profile is an artifact of the time step and the number of elements chosen.)

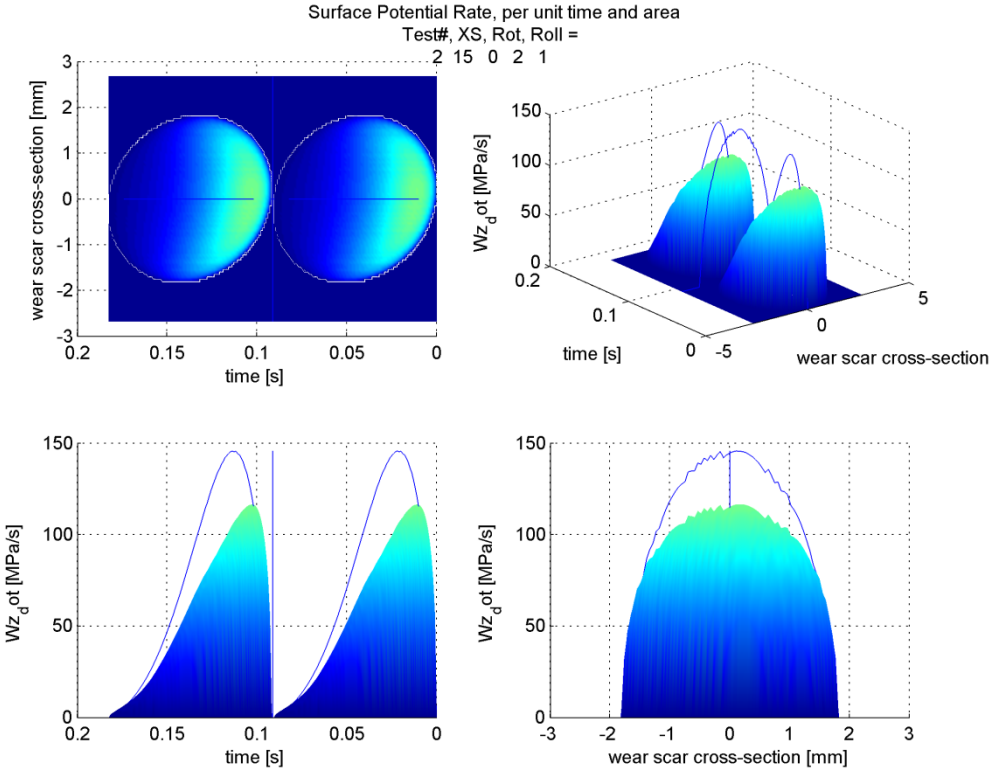

Figure 42: The rate of crossing surface potential, $\dot{W}_\zeta$, for "figure 8" sliding, for a memory distance of 1 mm. (The slight jaggedness of the profile is an artifact of the time of each step and the number of elements.)

3.3 - Results

The easiest way to compare the effect of the motions on the cross-shear values is by plotting them on the points of a cube. The tribological intensity (Figure 43) and total frictional work only varied with rolling, since the contact pressure, contact duration, and contact area was similar in all cases and the relative sliding velocity varied only with rolling. The crossing angle of the "figure 8" sliding path slightly increases the amount of tribological intensity due to the slight increase in cross-section width that comes in contact with the circular contact patch. The perpendicular component of friction work, however, was affected by the sliding motions, with the "figure 8" sliding path having a significantly higher component of perpendicular friction work than the linear sliding path (Figure 44). While the rolling motion decreased the total frictional work, it substantially increased the perpendicular component of frictional work. This is because of how the test was set-up with the rolling motion decoupled from the sliding motions – the rolling only decreases the sliding velocity in the PMO and doesn't change the perpendicular component of the sliding velocity. This increases the angle of the relative sliding direction and increases the perpendicular component of friction, and hence the perpendicular frictional work, without increasing the perpendicular sliding velocity.

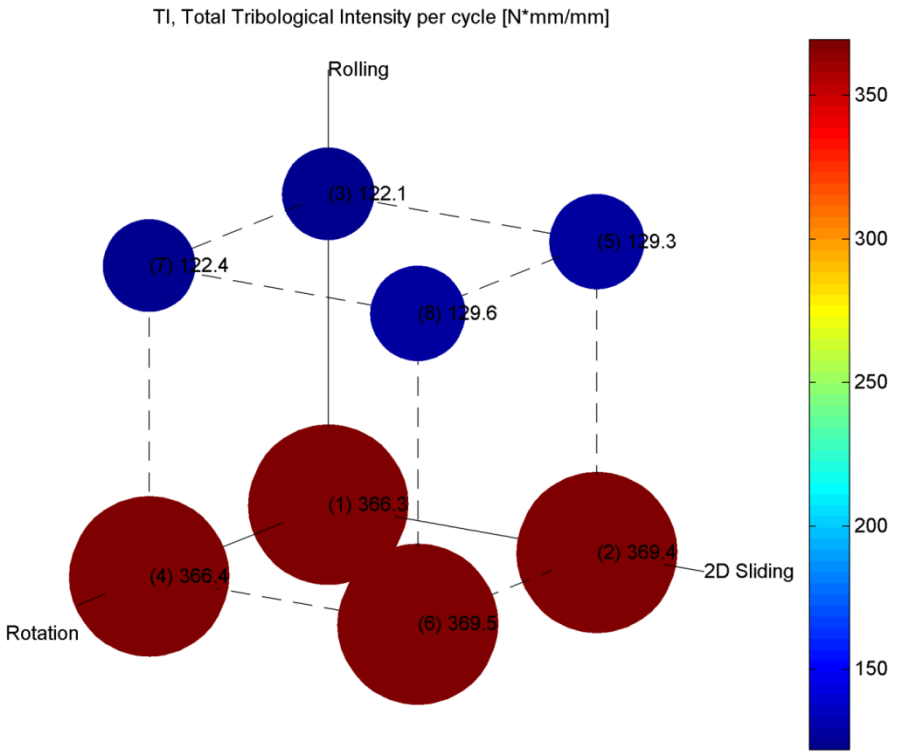

Figure 43: The tribological intensity per cycle, τ_l, for all motion combinations: with and without "figure 8" crossing motion, with and without rotation, and with and without rolling. The area of each circle is scaled to the intensity magnitude. The only significant difference between the combinations is that rolling decreases the relative sliding velocity, and hence the sliding distance and tribological intensity.

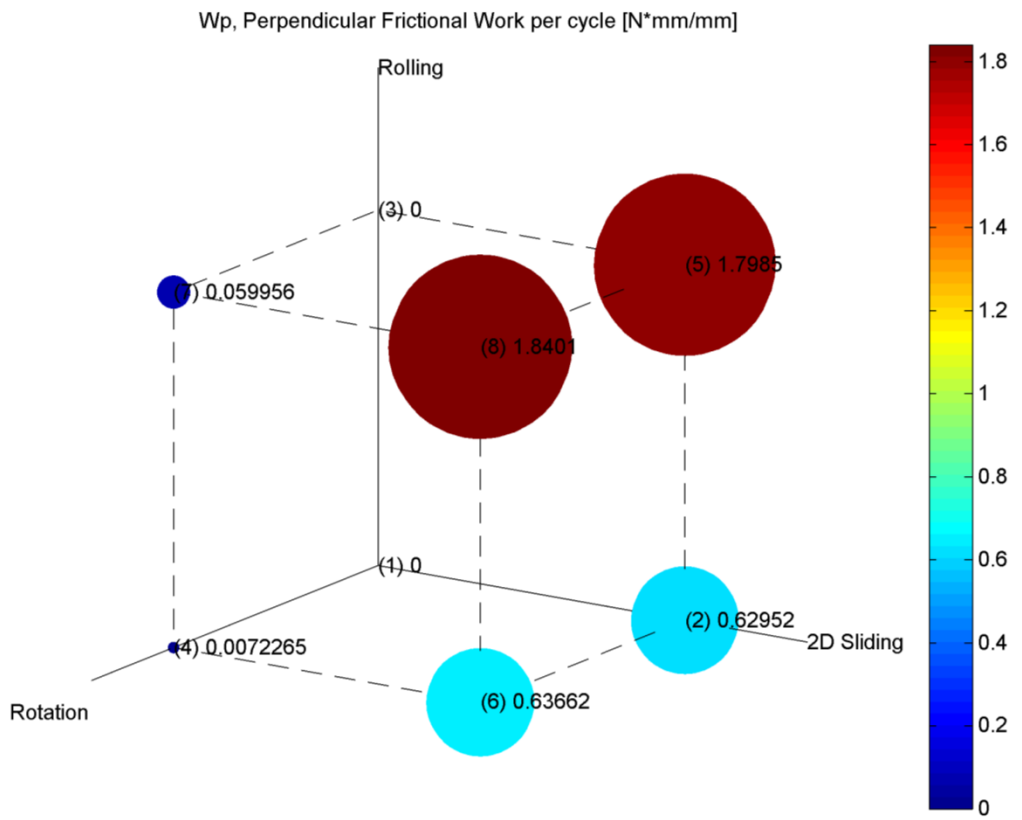

Figure 44: The perpendicular component of frictional work expended per cycle, $W_{\perp}$, for all motion combinations: with and without "figure 8" crossing motion, with and without rotation, and with and without rolling. As the complexity of motion increases, so does the amount of cross-shear.

This general trend, with the "figure 8" sliding having the greatest increase in cross-shear and rolling having the least, was seen for all cross-shear parameters (Table 7), although the relative effect differed between them. For example, with crossing intensity, σ, all values with 2D sliding had very similar amounts of total cross-shear, and the relative effect of the rotation motion was higher for cross-shear intensity, W_m, than for other cross-shear parameters. The relative effect of the rotation motion was also higher for the crossing surface potential, W_{ζ}, but the relative effect of 2D sliding was different between these two memory-based parameters, depending on the sliding distance needed for alignment. However, the trends did not change for some parameters. Specifically, while there is an important conceptual difference between the traditional perpendicular frictional work and the crossing-motion weighted calculation of perpendicular frictional work, and while the magnitudes of the cross-shear values were different, the relative trend in the values between all the motions was the same for both of these cross-shear parameters. This is because the relationship between crossing motion and the perpendicular frictional work were fairly consistent across the motion parameters used in this study, which according to eq. 21 leads to a fairly linear relationship between $W_{\perp}$ and W_{β}. To really differentiate between these two parameters you need to vary either only the ratio of crossing motion or only the total amount of perpendicular cross-shear.

It is also interesting to look at how the effect of a type of motion depends on the other motions present. This can be investigated by subtracting the amount of cross-shear for the case without that motion present from the amount of cross-shear with that motion present, with all other motions being the same for both. For example, to look at the effect of 2D sliding, “1D sliding” was subtracted from “2D sliding,” “1D sliding + rotation” was subtracted from “2D sliding + rotation,” etc. This yields four differences for each motion type and the standard deviation of these differences will hint at how consistent the effect of a particular type of motion was. The differences were never perfectly consistent for any measure of cross-shear, but they were more consistent for some that for others. The crossing intensity and memory-based parameters had the most consistency, with standard deviations ranging from 3 to 6 % of the greatest amount of cross-shear (i.e. relative to the value of cross-shear for the 2D sliding + rolling + rotation combination). For other parameters, the standard deviation was around 30% for the 2D sliding and rolling motions and about 1% for rotation. Theoretically, the same trends could be evaluated using multiplicative effects instead of cumulative, but this cannot be done easily in this case as two motion combinations had values of 0.

The ratios of cross-shear are mainly a measure of how much cross-shear there is for a specific sliding path relative to the total maximum amount of cross-shear that would exist under the worst possible sliding path for that given load and sliding distance. This is a maximum amount that primarily scales with the load and sliding distance, so most of the cross-shear ratios are normalizing the cross-shear magnitude by the tribological intensity. As was demonstrated in Figure 43, the main difference in the tribological intensity of the different motions is due to the rolling motion, so the main differences between the total cross-shear parameters and the cross-shear ratio parameters is the effect of the rolling motion. For example, the effect of rolling on the crossing motion ratio (Figure 45) is much greater than the effect of rolling on the perpendicular frictional work (Figure 44).

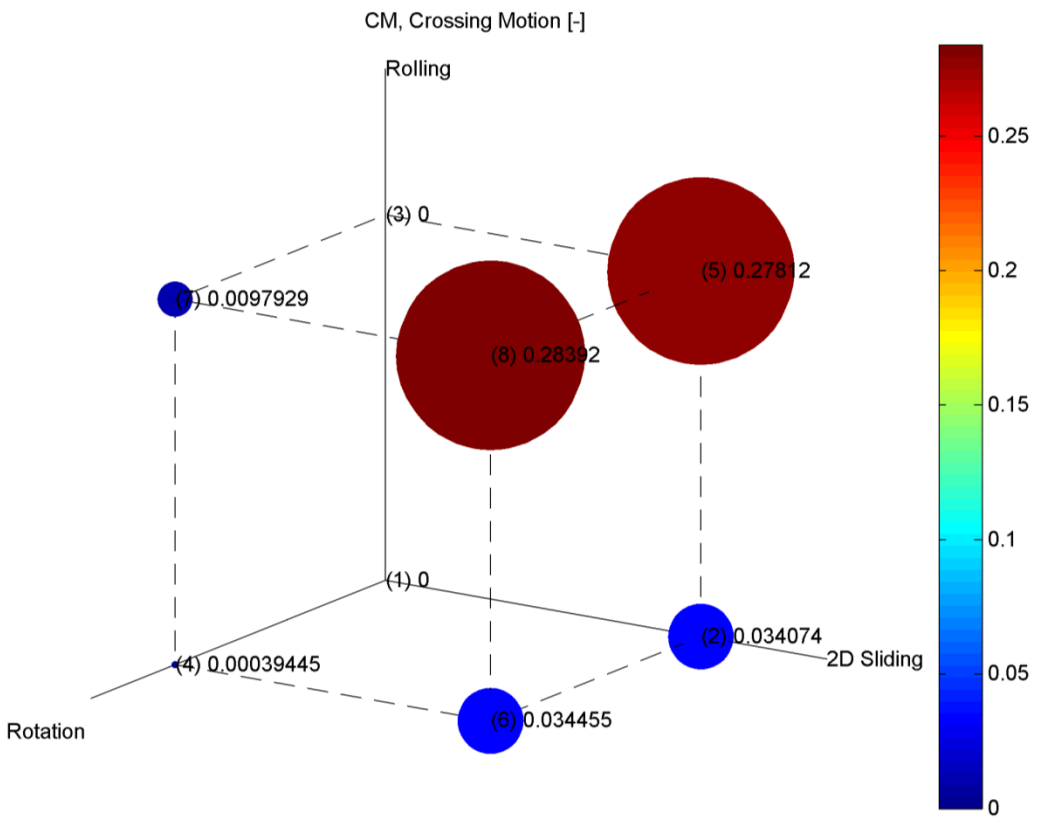

Figure 45: The crossing motion ratio for all motion combinations: with and without "figure 8" crossing motion, with and without rotation, and with and without rolling. The effect of rolling is much greater for the crossing motion ratio than for the perpendicular frictional work because of the decreased tribological intensity of the rolling motions.

The results of both of the memory-based cross-shear methods are a function of the memory distance, S_c. Physically this represents the sliding distance needed to align the molecules at the surface. This has a different effect on each wear path (Figure 46). If the weighting of the previous sliding angles is uniform, as in Petrella's method, then increasing the memory distance means each change in sliding angle has a longer lasting effect and the overall amount of cross-shear will increase until the memory distance is approximately equal to the sliding distance per cycle. If the weighting is an exponential decay, then the most recent change in sliding direction has the greatest effect. The longer the memory distance, the smaller this effect; the total amount of cross-shear decreases as the memory distance increases. For both memory based cross-shear parameters, the 2D sliding motions with rolling are much more sensitive to the memory distance than the other motions, both because they have greater changes in sliding angle throughout the cycle and because the sliding distance per cycle is less. Wear tests are needed to determine an appropriate value of S_c that gives the best agreement between the cross-shear values and the actual wear rates for a given formulation of UHMWPE.

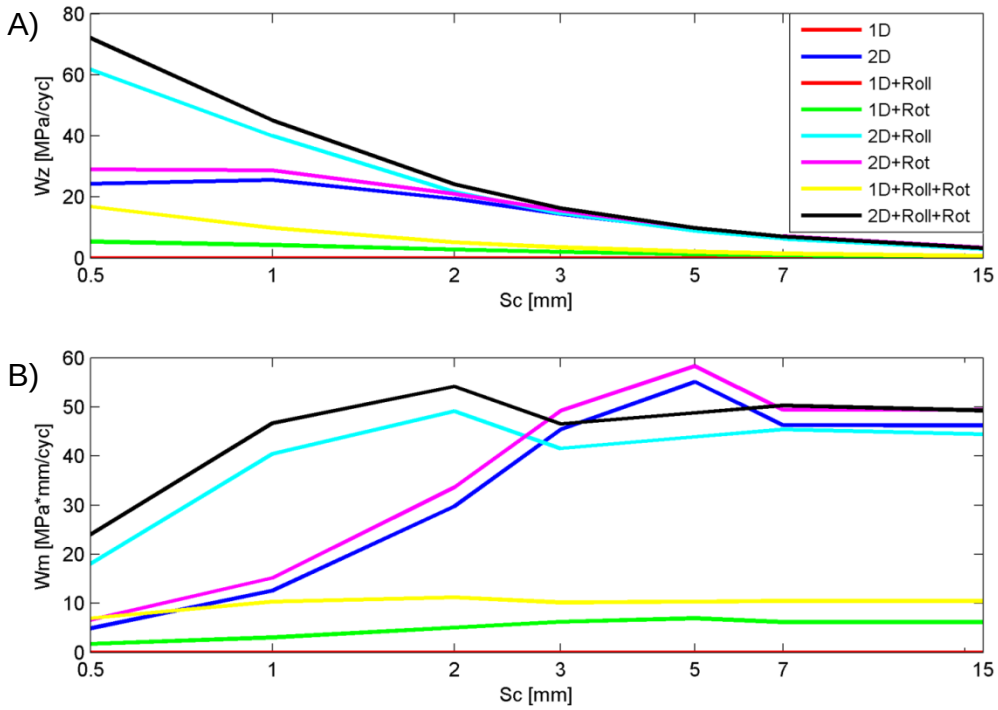

Figure 46: The (A) crossing surface potential, W_{ζ}, and (B) cross-shear intensity,W_m, for all motion combinations as a function of memory distance, S_c (on a log scale). 1D sliding and 1D sliding + rolling have zero cross-shear for all values of S_c.

Table 7: Tribological and cross-shear parameters for the eight different motion combinations. All parameters are for one full cycle.

	Sliding distance s_l $[mm]$	Total Frictional Impulse F_T $\left[\frac{N\ s}{mm}\right]$	Perp. Frictional Impulse $F_\perp$ $\left[\frac{N\ s}{mm}\right]$	Tribological Intensity τ_l $\left[\frac{N\ mm}{mm}\right]$	Total Frictional Work W_T $\left[\frac{N\ mm}{mm}\right]$	Perp. Frictional Work $W_\perp$ $\left[\frac{N\ mm}{mm}\right]$	CM weighted Perp. Fr. Work W_β $\left[\frac{N\ mm}{mm}\right]$	Crossing Intensity σ $\left[\frac{N\ mm}{mm}\right]$	Cross-shear Intensity W_m $\left[\frac{N\ mm}{mm}\right]$	Crossing Surface Potential W_ζ $\left[\frac{N}{mm}\right]$
1D	5.67	0.916	0.000	366.4	36.64	0.000	0.000	0.000	0.000	0.000
2D	5.71	0.924	0.121	369.5	36.95	0.630	1.238	32.89	45.42	14.39
1D+Roll	1.89	0.916	0.000	122.1	12.21	0.000	0.000	0.000	0.000	0.000
1D+Rot	5.67	0.916	0.011	366.4	36.64	0.007	0.0145	2.975	6.213	1.976
2D+Roll	2.00	0.924	0.344	129.3	12.93	1.799	3.097	33.61	41.54	14.66
2D+Rot	5.72	0.924	0.121	369.5	36.95	0.637	1.251	33.03	49.21	15.49
1D+Roll+Rot	1.90	0.916	0.054	122.5	12.25	0.060	0.119	4.966	10.20	3.474
2D+Roll+Rot	2.01	0.924	0.343	129.6	12.96	1.840	3.157	34.10	46.56	16.29

Table 8: Ratios of cross-shear for the eight different motion combinations. All ratios are unit-less.

	Perp. to Aligned Friction ratio C_f	Perp. to Aligned Frictional Work ratio C_w	Cross-shear Ratio CS	Crossing Motion CM	Normalized Crossing Intensity σ_0	Normalized Cross-shear Intensity X^*	Normalized Crossing Surface Potential Z^*
1D	0.000	0.0000	0.0000	0.0000	0.0000	0.0000	0.0000
2D	0.132	0.0173	0.0170	0.0341	0.1443	0.1229	0.0118
1D+Roll	0.000	0.0000	0.0000	0.0000	0.0000	0.0000	0.0000
1D+Rot	0.012	0.00020	0.00020	0.00039	0.0131	0.0170	0.0016
2D+Roll	0.402	0.1615	0.1391	0.2781	0.4214	0.3212	0.0341
2D+Rot	0.132	0.0175	0.0172	0.0345	0.1449	0.1332	0.0127
1D+Roll+Rot	0.059	0.00492	0.00490	0.00979	0.0656	0.0833	0.0085
2D+Roll+Rot	0.401	0.1655	0.1420	0.2839	0.4263	0.3592	0.0378

3.4 - Discussion

The results of the code were confirmed, where possible, with calculations of cross-shear presented in the literature. Cross-shear calculation in the literature are generally only given for common pin-on-disk motion paths were the pin is polyethylene, and not all motion paths are translatable to what would be seen when the disk is polyethylene. For example, the equivalent type of cross-shear motion of a circular translating pin-on-disk test (constant load but constantly and uniformly changing sliding direction) for a ball-on-flat test would be a “spirograph motion,” and then only for the part of the polyethylene at the very center of the motion. There is also no real equivalent pin-on-disk motion for the rolling and rotation motions used in this study, but the 2D sliding from a pure “figure 8” motion path is equivalent to polyethylene pin sliding along a rhombus-shaped path.

All of the different measures of cross-shear are designed to only take into account the component of motion perpendicular to the main sliding direction. All parameters will yield zero cross-shear if there is only linear motion, which is the case for the linear 1D sliding, and the linear 1D sliding + rotation. This means that if wear of polyethylene were only dependent on cross-shear, all linear paths with any combination of load, sliding distance, and roll-to-slide ratio would result in the same amount of wear: zero. This is obviously not realistic, but may be acceptable for some situations since the wear from cross-shear can be orders of magnitude higher than wear from linear sliding. The prediction of zero wear under linear motion is also applicable for memory-based parameters once the total sliding distance has exceeded that needed for full alignment.

One of the surprising results of the computer model is the effect that rolling played into the perpendicular component of frictional work. As explained earlier, this difference existed because the axis of rolling was not always perpendicular to the direction of sliding and so would not only decrease the relative sliding velocity but also change the relative angle of sliding. It is therefore difficult to discern whether the effect of rolling when combined with “figure 8” sliding is due to the increase in perpendicular friction or due to a change in the lubrication layer from the decreased velocity. In order to not have this effect, the rolling frame would have to rotate between the two halves of the wear path such that the axis of rolling is always perpendicular to the sliding direction when the contact patch crosses the center line. This could conflict with the rotation kinematics desired for other types of cross-shear motion. However, little is known about the exact kinematics in the knee and this type of motion (rolling in one direction and sliding in another) may be physiologically relevant and worthy of investigation. This is likely one of the reasons that the level of cross-shear for the combinations of motions was not simply the sum of their individual values of cross-shear. It also demonstrates why it might be important to test wear under combinations of motion instead of reducing it to a simplified form.

There are two important things to note about the contact pressure distribution used to calculate the cross-shear parameters in this computer model. First, the contact pressure distribution was only based on a finite element analysis of the initial contact patch. As the wear

scar forms, the contact pressure distribution would even out (Figure 25), changing the distribution of the cross-shear frictional work performed across the wear scar. It is uncertain though, how this would affect the wear rate as the test progressed, and if it would change the effect of the cross-shear ranking across the different motions. Even if this does change the total amount of cross-shear for a given motion combination, it will likely have little effect on the cross-shear ratio, as the tribological intensity is used for normalizing it would have the same change in contact pressure and sliding distance and cancel out the effect. Second, the contact pressure was modeled under static loading and does not include the effects of friction during sliding. However, this would likely only have a small effect as the contact pressure would slightly increase on the leading half of contact and slightly decrease on the trailing half. The only motions this might affect are combinations with both "figure 8" sliding and rotation, since the leading and trailing edge would have a different sliding angle from the rotation and this would either add to or decrease the effect of the "figure 8".

For general wear modeling, the memory-based parameters are more robust than the cycle-based parameters because they can take into account the effect of variations between cycles, the effect of change in the size in the sliding path, and the effect on only partial polyethylene alignment. While these memory-based parameters seem to be the most phenomenologically accurate, they only take the motion history into account for the current degree of alignment and do not include the load history. For example, consider a polyethylene pin sliding along a rectangular motion path with one edge that is much longer than that needed for full alignment, and a short edge that is less than what is needed for alignment. For two different loading cases, one with a constant load throughout the cycle and one with double the load for portion of the cycle on the short edge of the rectangle, both memory-based parameters would predict the same wear rate for the start of the long edge. No studies have been done that fully examine the effect of load on alignment, but it would make intuitive sense that more material would become aligned under the higher load of the second scenario than would be under the constant load of the first scenario, leading to a greater degree of cross-shear and higher wear rate in the second scenario. The model could be easily adjusted to account for this by including a load-based term in eq. 28 and eq. 32. An important implication leading from this change would be that instead of a specific sliding distance needed to fully align the polymer, there would be a specific level of tribological intensity (or frictional work).

Another difference between some of the ratios of cross-shear, whether based on sliding distance, frictional impulse, or frictional work, is whether to use the ratio of the perpendicular component to the total quantity, or the perpendicular component to the aligned component. The difference between the two is whether it is a sine term or a tangent term. Normalizing by the total amount of frictional, which is proportional to the tribological intensity, makes sense for evaluating wear in terms of a wear factor, while normalizing by the parallel component would make sense since that is the term that would be responsible for the degree of alignment. For small sliding angles, the differences would be minute, since both $\sin\theta$ and $\tan\theta$ can be approximated as θ. The crossing-intensity, by comparison, doesn't include any trigonometric

term in its calculation of cross-shear using instead only $\Delta\theta$, the difference in sliding angle in radians. This gives a greater weighting to the cross-shear occurring during large angles of sliding, which Hamilton states as the justification for choosing this formulation.

While there are currently many different parameters to quantify cross-shear that have been described in literature, most do not have strong phenomenological justification and no studies have compared them all across a wide range of motions. Therefore, while these parameters may be useful for optimizing joint replacement designs, they cannot offer guidance for how to improve the tribological performance of the material itself.

Chapter 4: Wear and Correlation with Cross-shear

4.1 - Wear rate and wear factor

The progression of wear scar cross-sectional area after the first day was typically very linear (Figure 29 and Figure 30). Once the wear scars had recovered from creep, many had slight raised portions at the shoulder (Figure 29 and Figure 47). Therefore, the profile heights were aligned using the flat, non-worn sections beyond the shoulder and the width of integration was expanded to ensure these shoulders were counted as “negative” wear. Most wear scar profiles were smooth, but some did have grooves in parts of the profile (Figure 47A). Most wear scar profiles were also symmetric, but some were slightly asymmetric with the deepest portion of the profile shifted about 0.5 mm to one side of the halfway point between the shoulders. Asymmetry was mainly observed in wear scars from motions with rotation, which has a higher relative sliding velocity and greater tribological intensity on one side of the profile, but this was not exclusively the case. Some wear scars had a flat or humped portion along the bottom of the profile that became more pronounced following creep-recovery (Figure 47B). This was almost exclusively observed with the 2D sliding motion.

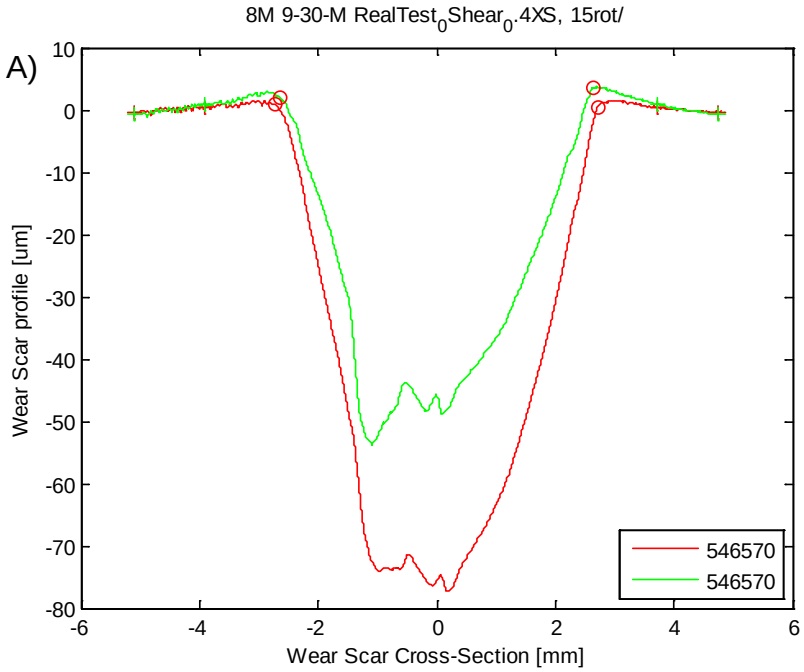

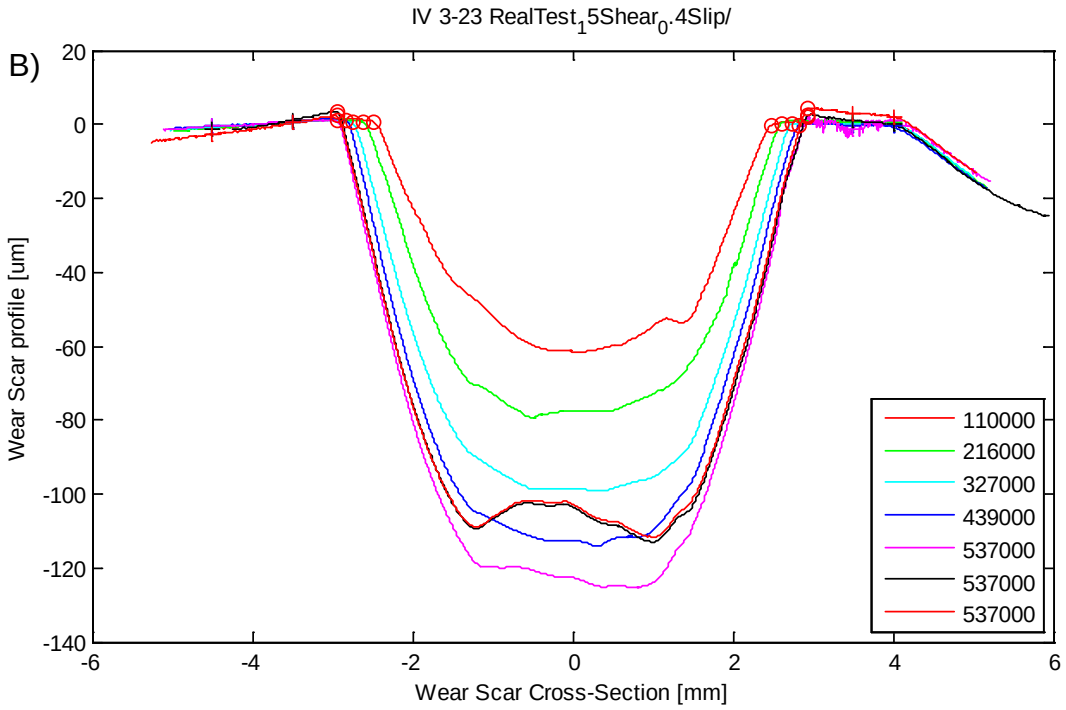

Figure 47: Examples of wear scar profiles during and after testing. A) 1D sliding + rolling + rotation, the second profile is after almost a month of strain recovery. B) 2D sliding, the last two profiles are after 1.7 and 6 months of strain recovery.

Most of the linear wear scars had a consistent profile along their length, up to about a contact-radius away from the ends. The profile of the wear scars from motions with a “figure 8” sliding component varied greatly along the length (Figure 48), as would be expected with a constantly changing amount of cross-shear and total sliding length. For the measurement in Figure 48, 42 individual scans were stitched together, small areas of missing data were interpolated (the black areas are missing data too-large to accurately interpolate between), and the tilt was corrected based on the non-worn region. On the non-wear surface, some circular, lathe machine marks that weren’t fully sanded away can be seen. The deepest area of the wear scar is at the center, where there was the largest crossing angle and complete overlap between both directions of the path. The large green areas on the sides of the wear scar indicate a slower wear rate on account of only coming into sliding contact with the CoCr sphere once per cycle instead of twice. At the end of the wear scar is another deep area, which experienced the high contact pressures of the center-of-contact and greater levels of of cross-shear as the sliding direction quickly curved and reversed direction.

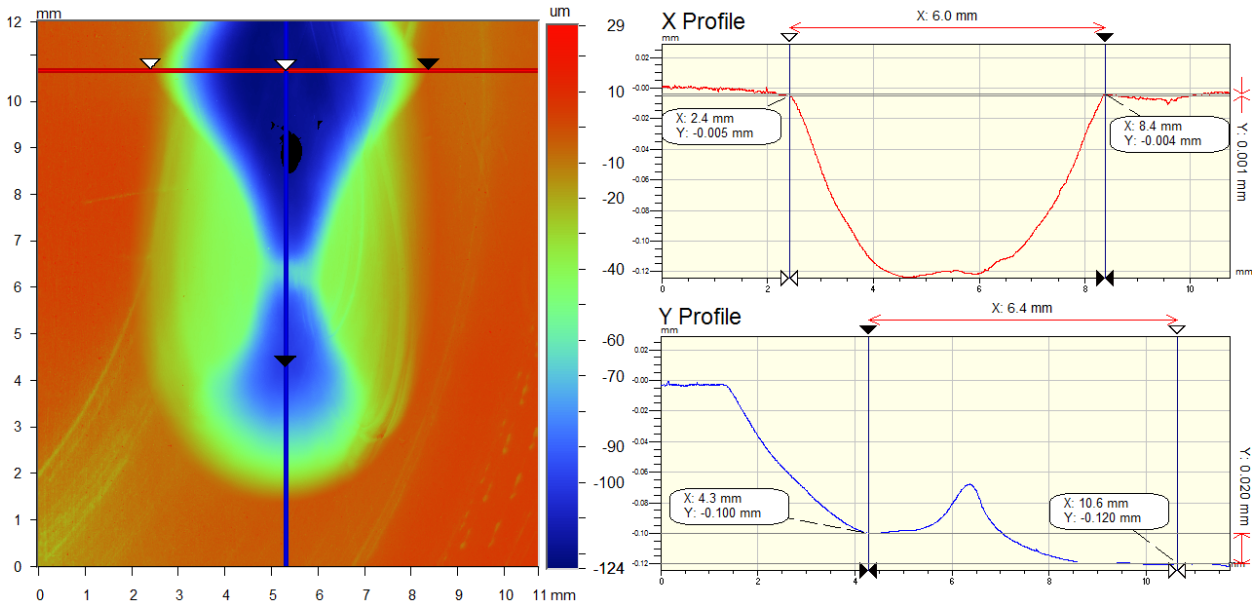

Figure 48: Color counter plot and 2D X and Y profiles from optical profilometry on half of a “figure 8” wear scar, 13 months after 530k cycles of wear testing.

The amount of wear from each test was quantified by measuring the cross-sectional area of the wear scar at the midpoint along the wear path, both directly after a test and at least three weeks after the end of the test. The area percentage of the wear scar cross-section that was recovered after creep was generally on the order of 10% or less. Motions with low wear rates, 1D sliding, 1D sliding + rolling, and 1D sliding + rotation, generally had a greater amount of creep recovery, from 25 to 60%. The wear rate (Figure 49) was then calculated using the final, creep recovered wear scar cross-sectional area and the total number of cycles from each test. The crossing angle from the “figure 8” had the greatest effect on wear rates and the rotation motion had the smallest effect on wear rates, while the effect of the rolling motion was essentially negligible.

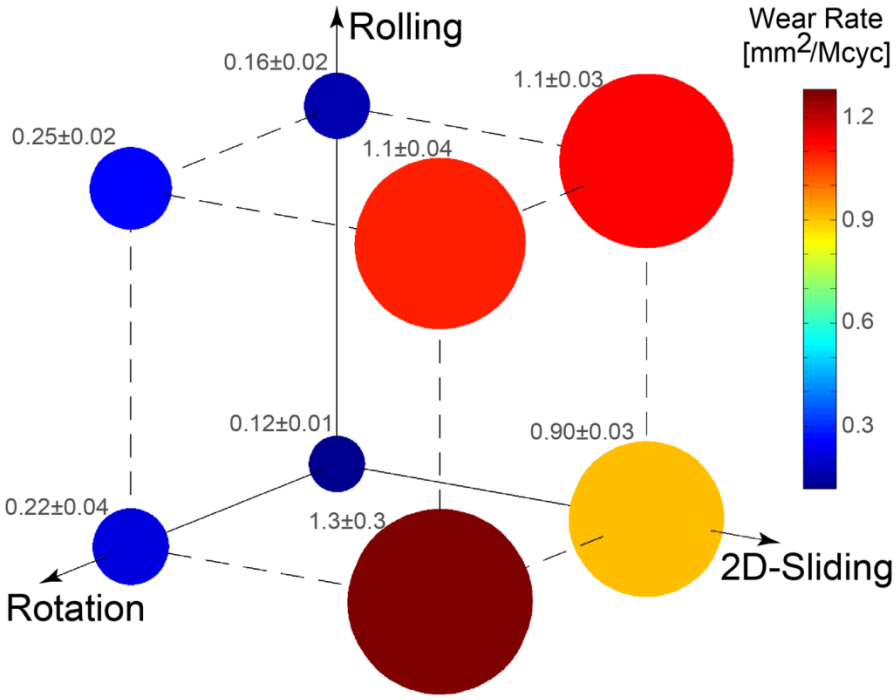

Figure 49: Average ± standard error of the wear rate for the different motions (the area of each circle is scaled to the average wear rate). N = 2-6 wear tests for each motion combination.

There is always scatter and variability in wear testing, and these tests were no exception. However, most test conditions showed relatively repeatable results (Figure 50). Two motion combinations had data points that had much different wear rates from others in their motion combination. Each of these data points was from a different run of tests, the test logs showed no unusual normal loads or temperatures, and nothing appeared remarkably different on the wear scars or the CoCr counter bearings. For the motion combination with more than one repetition, the outlier status was confirmed using Chauvenet's criterion (< 0.3) and Dixon's Q test (at 95%) and removed for all other analysis. The other motion combination had only two data points so neither could be removed and they were both used for all analyses.

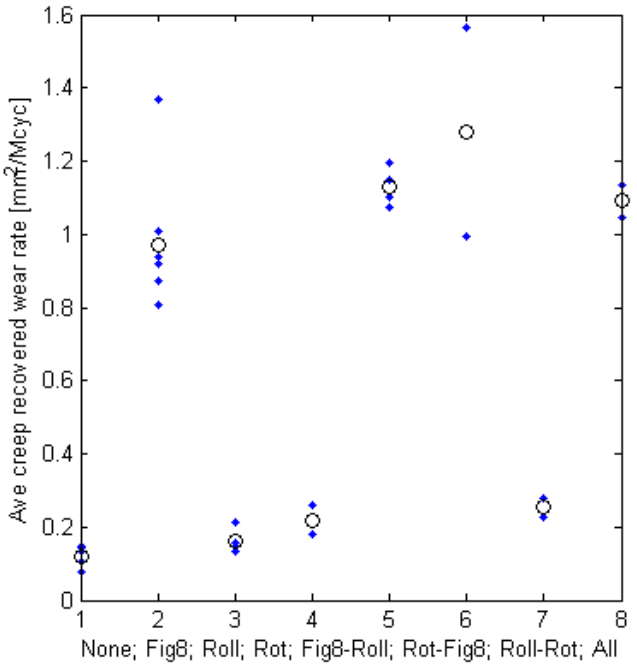

Figure 50: Individual wear rates from every completed test (blue dot) for all the different motion combinations, plotted with the average wear rate for each motion combination (circle). The upper point for motion combination #2 tests positive as an outlier and was removed for all analyses.

To account for the decreased slip velocity in the rolling case and increase in wear scar width for the crossing case, the wear factor (Figure 51) for each motion type was calculated by normalizing the wear rate by the total tribological intensity experienced per cycle at that cross-section (eq. 6 and eq. 7).

The technique described in section 3.3 for isolating the effect of a particular type of motion was also applied to the wear rates and wear factors. The standard deviations of the differences in wear rates were about 10%, compared to up to 25% for the wear factor. Separating the effect of the different motions on wear rate was most consistent with combinations that produced a low wear rate.

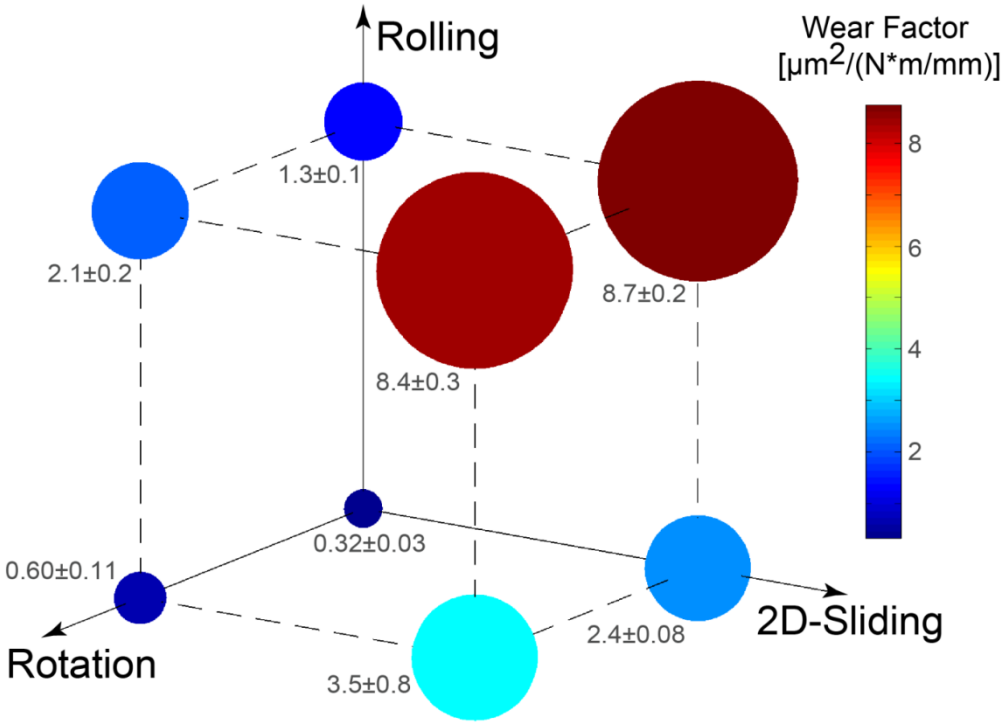

Figure 51: Average ± standard error of the wear factors for the eight different motion combinations (area of each circle is scaled to the wear factor). N = 2-6 wear tests for each motion combination.

4.2 - Correlations of cross-shear and wear

The classic model of wear using Archard's law states that there is a linear relationship between total tribological intensity and final wear volume and analogously between tribological intensity per wear cycle and the wear rate. This model has often been shown to be inappropriate for UHMWPE because of the importance of cross-shear. The results of these wear tests also confirms that simply using tribological intensity is a poor indicator of wear rate (Figure 52).

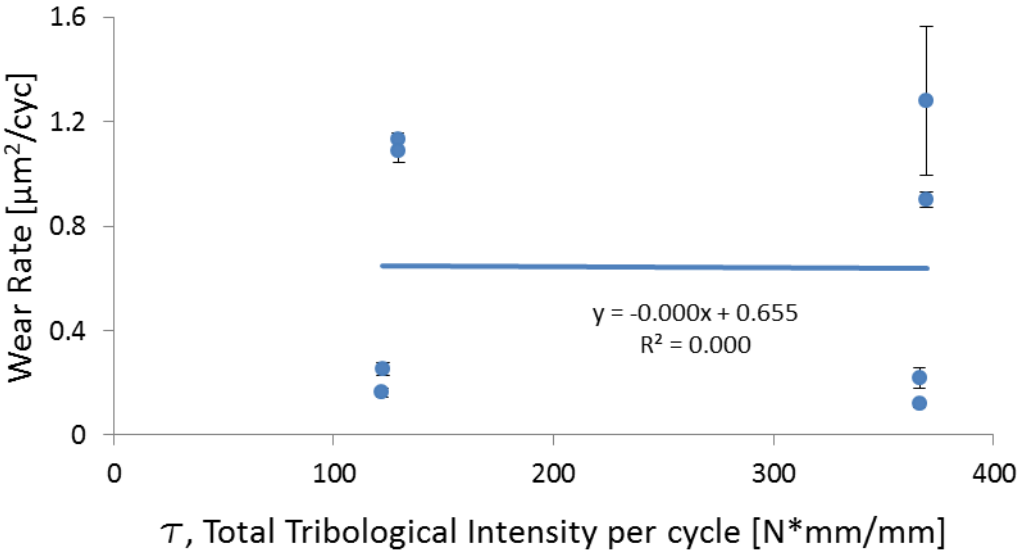

Figure 52: Average ± standard error of the wear rate is not predicted by Tribological Intensity (τ), demonstrating the importance of cross-shear on the wear of UHMWPE.

Wear rates correlated much better with measures of total cross-shear (Table 9) such as W_β, the perpendicular frictional work weighted by the crossing motion (eq. 19, Figure 53), and σ, the crossing intensity (eq. 23, Figure 54).

Table 9: Coefficient of determination of the least squares, unconstrained linear fit between measures of total cross-shear and wear rate.

	$F_\perp$	$W_\perp$	W_β	σ	W_m	W_ζ
R^2 w/ linear fit to $\dot{V}$	0.638	0.659	0.704	0.958	0.958	0.961

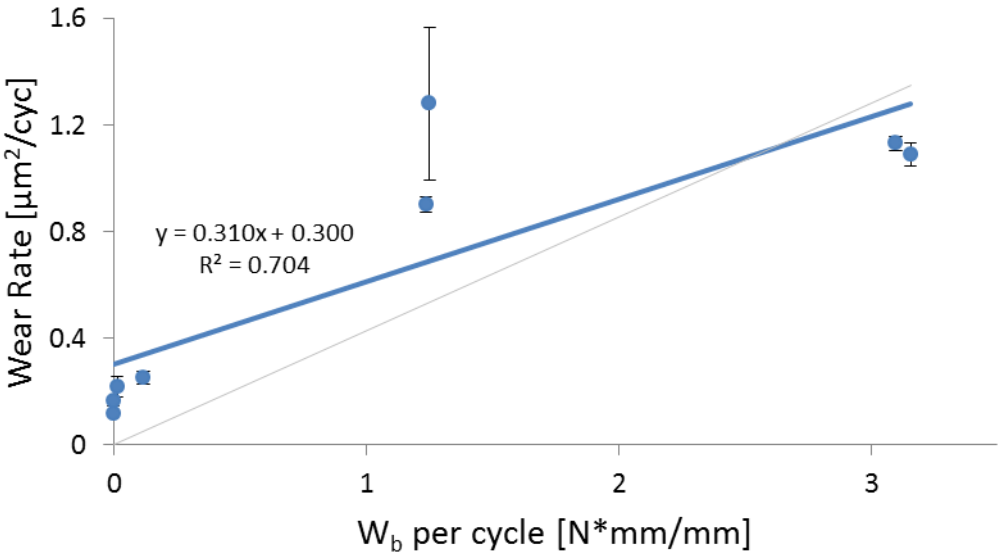

Figure 53: Average ± standard error of the wear rate has a relatively weak linear correlation to W_β, the perpendicular friction work weighted by the crossing motion ratio (eq. 19). The gray line is the best fit for a directly proportional relationship.

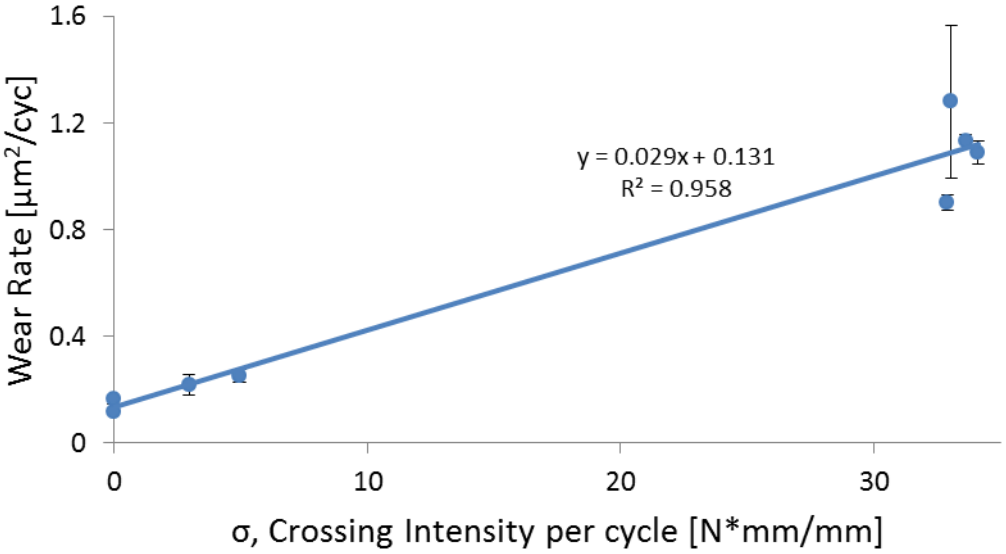

Figure 54: Average ± standard error of the wear rate has a good linear correlation to σ, the crossing intensity (eq. 23), but this may simply be due to the two clusters of data.

The highest degrees of linear correlation were between the wear factor and ratios of cross-shear (Table 10), such as crossing motion (Figure 55, eq. 20) and the normalized crossing intensity (Figure 56, eq. 26).

Table 10: Coefficient of determination of the least squares, unconstrained linear fit between ratios of cross-shear and wear factor

	C_f	C_w	CM	σ^*	X^*	Z^*
R^2 of linear fit to k'	0.981	0.950	0.955	0.980	0.967	0.974

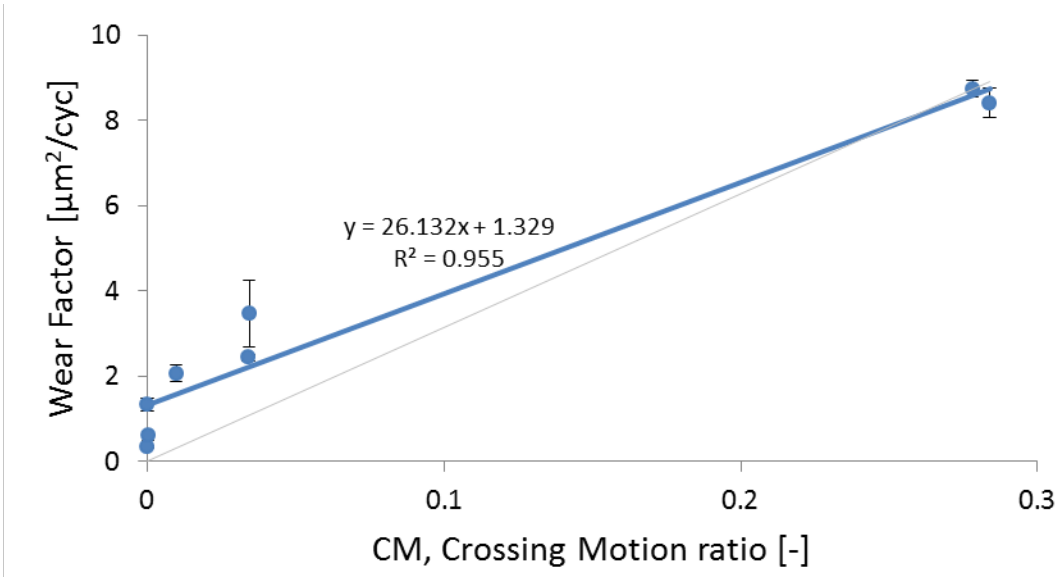

Figure 55: Average ± standard error of the wear factor has a good linear correlation to CM, the crossing motion ratio (eq. 20). The gray line is the best fit for a directly proportional relationship.

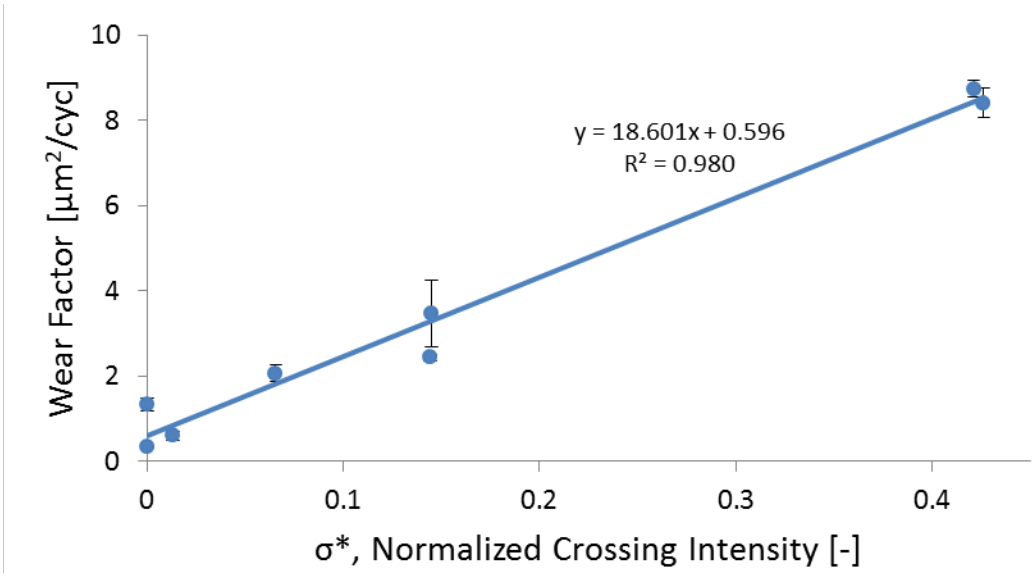

Figure 56: Average ± standard error of the wear factor has a strong linear correlation to σ^*, the normalized crossing intensity (eq. 26).

The memory-based total cross-shear parameters also achieved a strong linear correlation with the wear rate when calculated with a memory distance of S_c = 3 mm for linear average method and S_c = 2 to 3 mm for the exponential decay method (Figure 57A). The correlation between the memory-based cross-shear ratios and the resultant wear factor was even slightly higher (Figure 57B). When using a least squared fit line to calculate the memory-based wear factors, k_0 and k^* (eq. 27), and k_m (eq. 31), Petrella's method yields a slightly higher goodness-of-fit (Figure 57C, Table 11). However, this is most likely only because it allows for a factor that can account for unidirectional wear, while Strickland's method does not, which has the effect of forcing the Y-intercept of the best fit line to pass through zero. Comparing the methods on a more even basis shows little difference between the two.

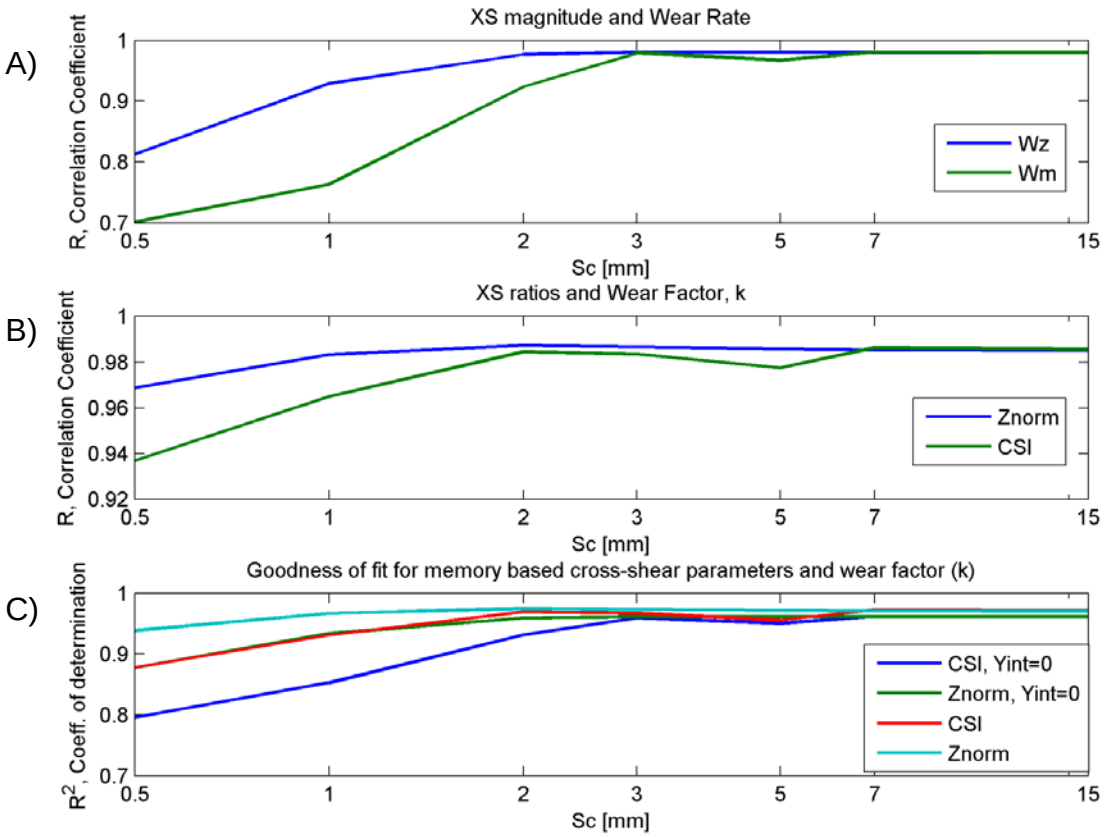

Figure 57: For the memory-based cross-shear approach, the greatest correlation between total parameters and wear rate (A), cross-shear ratios and wear factor (B) and the highest goodness-of-fit parameters (R^2) between cross-shear ratios and the wear factor, both with and without an intercept (C) was around a memory distance of 3 mm.

Table 11: Wear factors from the best fit lines between the memory-based cross-shear parameters (S_c = 3 mm) and the resultant wear factor for both constrained and unconstrained fits.

		Slope	Offset	R^2
Constrained fit:	X^*	24.9	0.00	0.960
	Z^*	k_m = 239	0.00	0.962
Unconstrained fit:	X^*	k^* = 23.4	k_0 = 0.391	0.967
	Z^*	222	0.475	0.974

4.3 - Discussion

In this study, a CoCr sphere was articulated against non-crosslinked UHMWPE at a peak contact pressure of 27 MPa (~18 MPa mean, 200 N load) and a range of motions, from unidirectional reciprocating to a slide-roll ratio of 0.4 to a combination of 2D sliding, rolling, and rotation that lead to a crossing motion ratio of almost 0.3. The wear factors in this study ranged from 0.3 to 8.7 $\frac{\mu m^2}{Nm/mm}$, or 0.3 to 8.7 $\times 10^{-6} \frac{mm^3}{Nm}$, depending on the motion combination. This is

slightly higher that has been reported in other wear studies, but given the inherent variability in wear testing and the differences between the testing conditions, these results are quite reasonable. Saikko et al. reported a wear factor of 0.2 to $0.4 \times 10^{-6} \frac{mm^3}{Nm}$ for flat, gamma-inert sterilized, UHMWPE pins rubbing on smooth CoCr disks in a 9 mm diameter circular translating motion path ($CM = 1$) at a contact pressure of 10 MPa (Saikko 2006) and $0.39 \times 10^{-6} \frac{mm^3}{Nm}$ for a CoCr in 1D sliding + rolling + rotation contact with a flat, non-crosslinked UHMWPE disk at a contact pressure of 17 MPa (Saikko & Calonius 2002). Barbour et al. reported a wear factor of $0.12 \times 10^{-6} \frac{mm^3}{Nm}$ for a spherically-tipped metal pin in unidirectional reciprocating sliding against a non-irradiated UHMWPE disk at average contact pressure of just over 10 MPa (Barbour et al. 1997). Van Citters et al. reported wear rates that convert to a wear factor of $0.3 \times 10^{-6} \frac{mm^3}{Nm}$ for pucks of CoCr and conventional polyethylene rolling against each other with a slide-roll ratio of 0.4 and peak contact pressures of 19 MPa (Van Citters et al. 2007). Cornwall et al. reported wear factors of $0.19 \times 10^{-6} \frac{mm^3}{Nm}$ for spherically tipped CoCr pins on lightly crosslinked UHMWPE, reciprocating along a linear path under a 200 N for an average contact pressure of 32 MPa (Cornwall et al. 2001).

It is important to note that in general, wear tests of metal pins on polymer disks tend to report higher wear rates than a polymer pin on a metal plate under equivalent conditions (Cornwall et al. 2001; Barbour et al. 1997). Also, wear measured using volumetric methods would tend to overestimate wear because the creep of the scar profile may not fully recover, even after months, while wear measured using gravimetric methods would tend to underestimate wear because of mass gain from fluid adsorption, even when using a load-soak control. For these wear tests, creep was assumed to be responsible for all changes in the profile not due to material removal from wear. It was also assumed that creep deformation was fully recovered once the profile dimensions stabilized (about a month after the test finished) and that any overestimations due to creep would not vary with the cross-shear of the motion path. Early testing suggested that the creep-recovered wear measurements were comparable to steady state wear measurements taken during the test, even for tests run out to 1.5 million cycles. However, if the load was high enough to cause permanent plastic deformation, the different levels of cross-shear may affect the kinematic softening of the polymer and the amount of plastic deformation reached.

Creep of the polymer would also be a factor in the shape of the wear scar profile. Even though the “pin” articulating against the polymer is perfectly spherical, the wear scar profiles fit a higher order polynomial much better, and had a radius of curvature of up to double that of the CoCr sphere. As the wear scar develops, FEM analysis demonstrated that peak stresses drop to below yield and the contact patch widens (Figure 25B). Matching the depth of the profile with profiles of local contact pressures, tribological intensity, and cross-shear ratios could potentially be used to examine how the wear factor changes across a full spectrum of values. Such analysis might allow yield special insight when applied to the ends of the wear scars that had a “figure 8” component of motion, which display a unique contour due to the wide range in tribological

intensity and cross-shear likely present there. Unfortunately, the usefulness of this type of analysis would be limited without investigating the variations in lubrication film thickness and creep across the profile and taking them into account. Such analysis could also be potentially used to explain the presence of a center hump on some of the wear scars.

The standard Archard wear law describes a linear relationship between tribological intensity and wear volume, and most wear models that have been adapted for cross-shear also use a linear relationship between their measure of cross-shear and the wear rate. This may not necessarily be fully accurate, and the relationship may be more accurately described by another type of fit. For example, when validating the crossing intensity parameter, Hamilton et al. plotted data from cross-shear wear tests (Turell et al. 2003) on a log-log graph and fitted a linear line to it (Hamilton et al. 2005). Kang et al. compared their model based on the cross-shear ratio using multiple fits: piece-wise linear, power, and logarithmic. Power and logarithmic fits, however, cannot be used for data sets with points at 0 and could not be used to predict wear under linear motions, as is the case here. The many parameters used in this dissertation were mostly analyzed using an unconstrained, least-squares linear fit and compared using the coefficient of determination, R^2. However, the coefficient of determination is not enough on its own to discriminate between different models whose explanatory variables may have some collinearity, nor will it indicate that the ideal type of fit was used. Many of the cross-shear parameters examined in this study had R^2 values above 0.9 or even 0.95, suggesting a high degree of explanatory power. Some of these large R^2 values can be attributed to how a particular definition of cross-shear and the parameters of the motion paths chosen for this set of tests resulted in two separate and relatively tight clusters of data, as may be a factor for the linear fit with crossing motion (Figure 55). More testing with different cross-shear motion parameters could fill out these fits and show which definition is the most appropriate. However, if there is only a little difference between the different parameters and they all work relatively well, it might not matter which specific one is used. An additional point to consider is that some of these parameters were specifically developed for use with crosslinked polyethylene, which may have a completely different form of relationship between cross-shear and wear than non-crosslinked polyethylene.

Two very important strengths of this study are the fundamental and realistic contact conditions used to validate the relationships and the large number of cross-shear parameters that were compared. The studies that proposed the cross-shear parameters used in this study were either validated using rectangular sliding (Turell et al. 2003; Dressler et al. 2011; Hamilton et al. 2005) or sliding and rotating (Kang, Galvin, Brown, Jin, et al. 2008) flat pin-on-disk testing, or wear testing with joint simulators (Willing & I. Y. Kim 2009a). As discussed earlier, these types of pin-on-disk tests may not be realistic enough to apply the results to *in vivo* conditions, and there are so many other factors that may be playing a role in a joint simulator that the effect of cross-shear cannot be isolated. Also, most studies validate their cross-shear parameter by demonstrating a good fit their wear test results, but they typically don't compare their parameters to the others proposed in literature.

Many of the cross-shear parameters actually had very good fits with the wear factors measured in this study. The difference between an R^2 of 0.961 and 0.980 is small compared to the uncertainty present in wear tests and so the subtle differences found with this set of motion parameters is not enough to confidently determine the most appropriate cross-shear parameter. More wear tests at different combinations of rolling, sliding, and rotation, especially combinations that predict the same amount of cross-shear using different combinations of motion, will be needed to fully understand the best way to predict wear. However, the cross-shear parameter that is theoretically most robust and also one of the best-performing in this study is the memory-based, crossing surface potential, W_ζ. Further improvements might include the addition of a linear offset term and further investigation into the role of contact pressure on the alignment and the wear factor. These could be easily integrated into the generic framework that Strickland et al. proposed.

Chapter 5: Wear Surface and Microstructure Analysis

5.1 - Wear surface

Overall the polyethylene wear surfaces appeared smoother than the original surface and had a burnished finish (Figure 31 and Figure 48). A few deeper scratches in the direction of sliding were also evident on many wear scars. There were no apparent polyethylene transfer films on the CoCr wear surfaces. Slight scratching, was often visible on the CoCr wear surface, more commonly on the non-rolling tests. Most were under a few hundred nanometers deep, but some were up to a few microns deep.

When the wear scars were viewed through an optical microscope at 5-20x, some scratches from the polishing were partially evident on many of them (Figure 58A). When measured using optical profilometry, most of these scratches were so small they were no longer visible above the scratches from the wear tests, even for 1D sliding motions (Figure 58B), which exhibited the lowest wear rates. Some scratches could be made more apparent if the curvature of the wear scar was removed, but the scratches from the wear test itself dominated the profile. The edges of the wear scar featured shoulders that were slightly raised above the surrounding unworn profile, but the ends of the wear scars had much smaller, if any, raised shoulders.

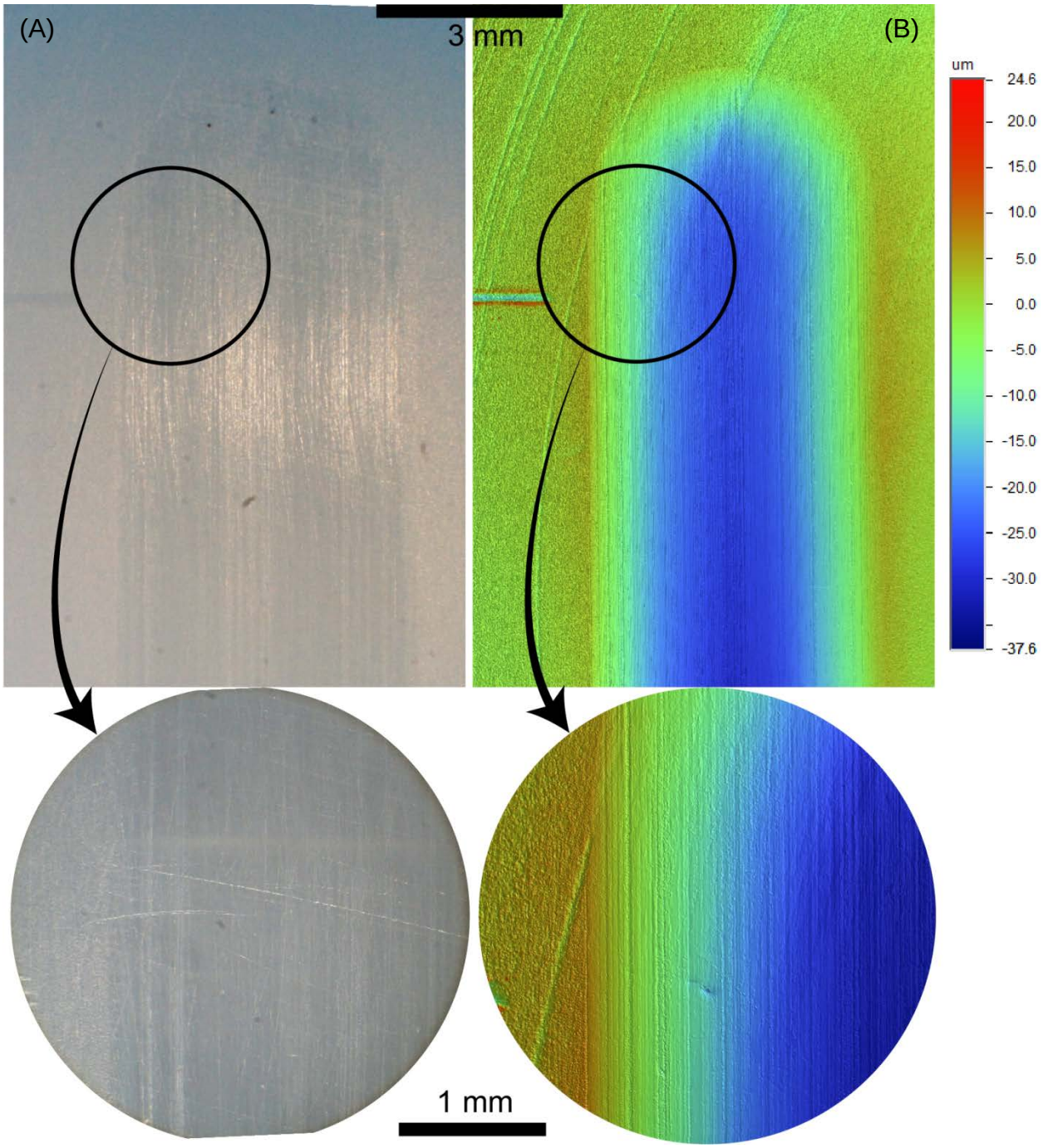

Figure 58: Microscope images (A) and optical profilometry contours (B) of a wear scar, taken 13 months after 540k cycles of 1D sliding. Scratches visible under a microscope at 5x essentially disappear when measured on the optical profilometer.

SEM images revealed a mostly featureless surface with small scratches, most were aligned with the sliding direction but some polishing scratches were visible as well. Also common were ripples, or folds, aligned roughly perpendicular to the sliding direction and a wavelengths on the order of 4 μm (Figure 59). Additionally, there were several instances of surface cracking perpendicular to the primary sliding direction (Figure 60).

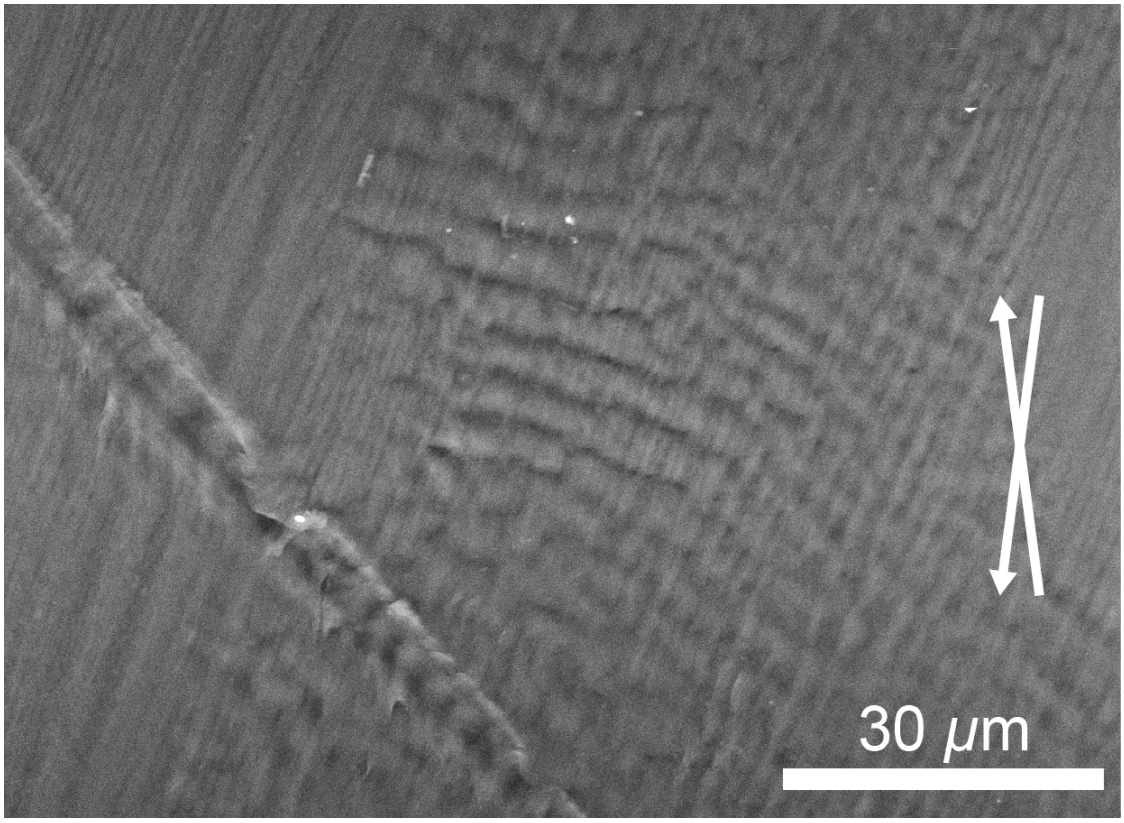

Figure 59: SEM image of the un-etched wear surface from 2D sliding. Small scratches and areas of ripples were common, though much of the surfaces were featureless.

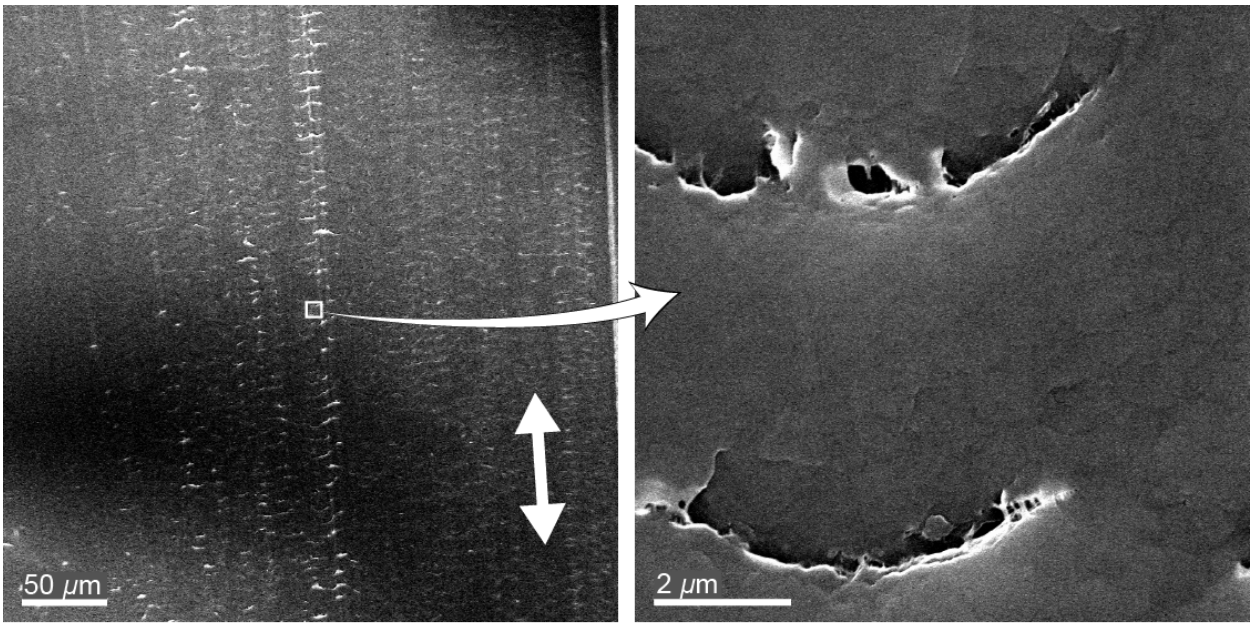

Figure 60: SEM images of the un-etched wear surface from 1D sliding. Several surface cracks are visible perpendicular to the sliding direction (double-headed arrow).

5.2 - Texture development

Etching away the amorphous phase of the microstructure revealed the lamellae structure at the wear surface (Figure 61C). The orientations of the lamellae at the wear surfaces were not discernibly different from the lamellae of an unworn section of the disk surface (Figure 61D). Similarly, the near-surface regions of the disk cross-section (Figure 61A) were not discernibly different from the subsurface regions (Figure 61B).

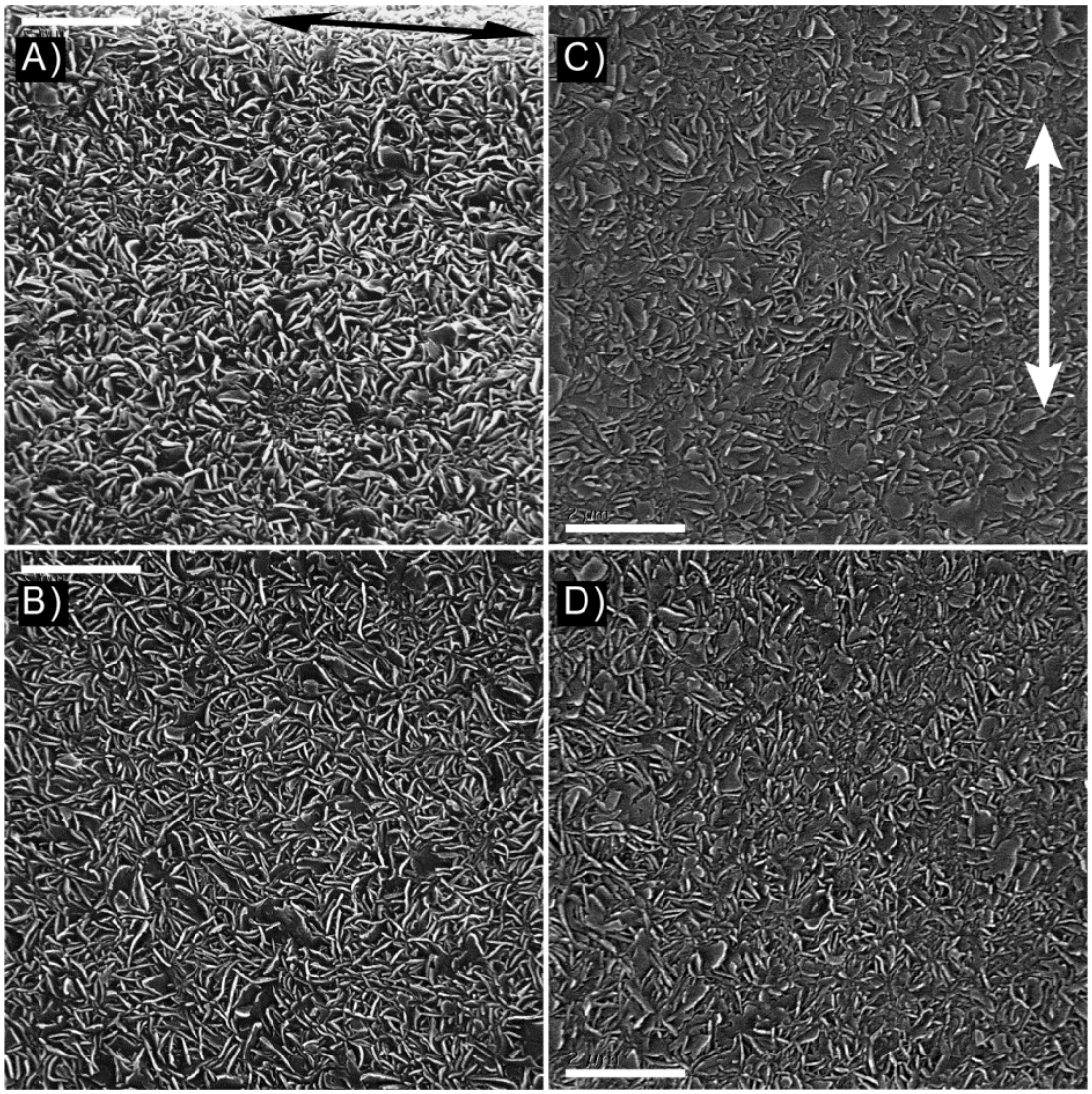

Figure 61: Images of the UHMWPE microstructure and wear surface. A) SEM image of the near-surface region of the cross-section (perpendicular to wear surface and parallel to the sliding direction) of the wear path under pure reciprocating sliding, etched to reveal the lamellar microstructure; the wear surface and sliding direction visible at the top. B) Subsurface region of the same cross-section, approximately 600 µm below the wear surface. C) The microstructure of the wear surface following pure reciprocating sliding. D) The microstructure of the surface of an unworn area of the UHMWPE disk. Arrows in images represent the sliding direction; all scale bars are 2 µm long and all images are shown at the same scale (10,000x).

These observations were confirmed with the image analysis of select surface images. Several images, at a range of magnifications, were analyzed for several types of wear tests and locations: the wear surface, the non-wear surface, the upper near-surface (within 5 µm), the lower near-surface (5-10 µm), and the subsurface (>1-2 mm). Some slight differences could be detected noticed between some of the image groups. For example, Figure 62 shows one of the greatest differences between the images from the wear surface of two different motions. However, these differences were not striking and, moreover, were on the order of the variation with an image group (Figure 63). With the large amount of variation present in the data, no conclusive differences or larger trends could be found in the lamellar orientation of the wear and non-wear surfaces, wear surfaces of different motions types, the upper and lower near-surface regions, or the near- and subsurface regions (Figure 63, Figure 64, Table 12).

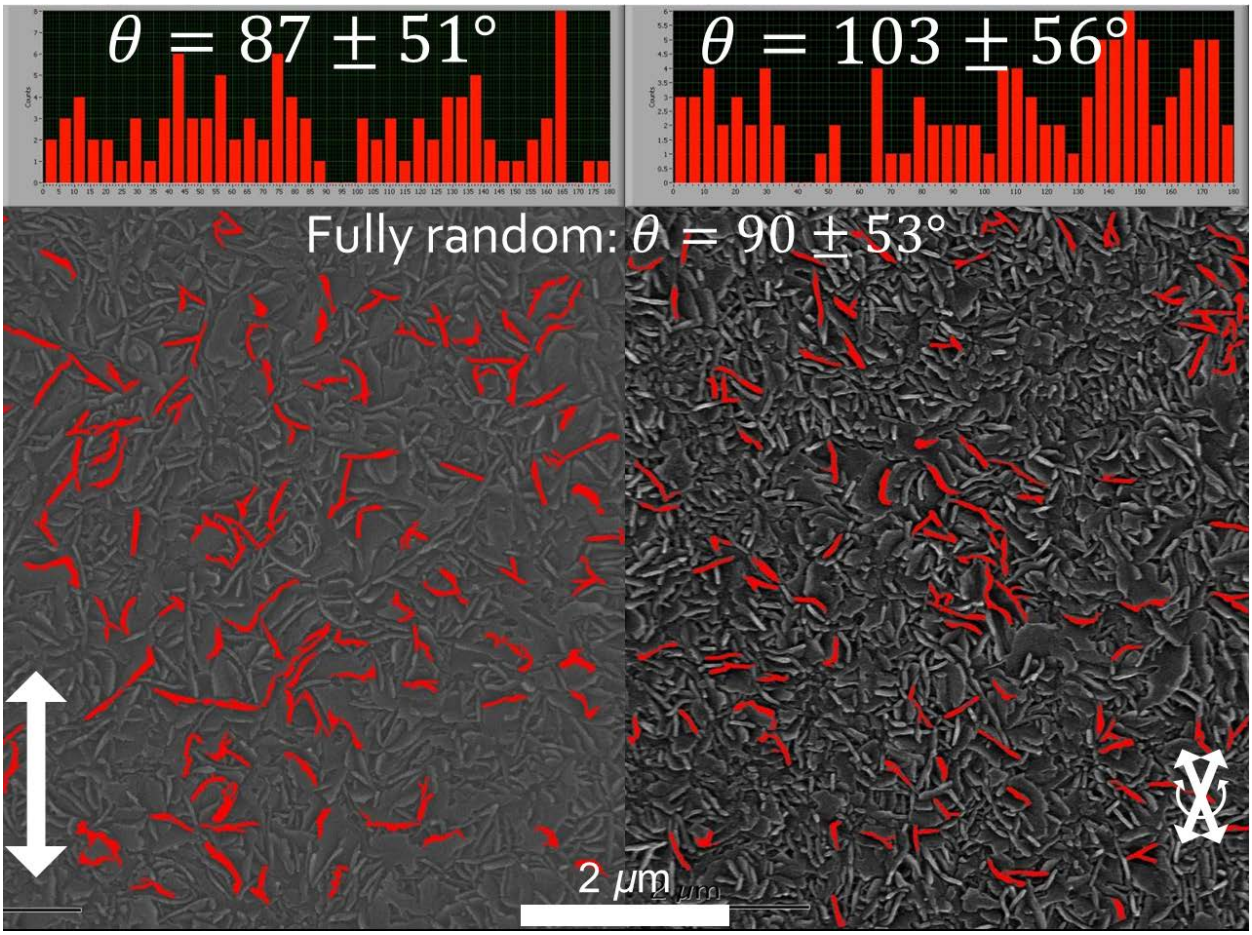

Figure 62: A comparison of the distributions of lamellae orientation between two different wear surfaces: linear sliding, and 2D sliding with rolling and rotation. The difference in standard deviation between these two images was one of the largest found.

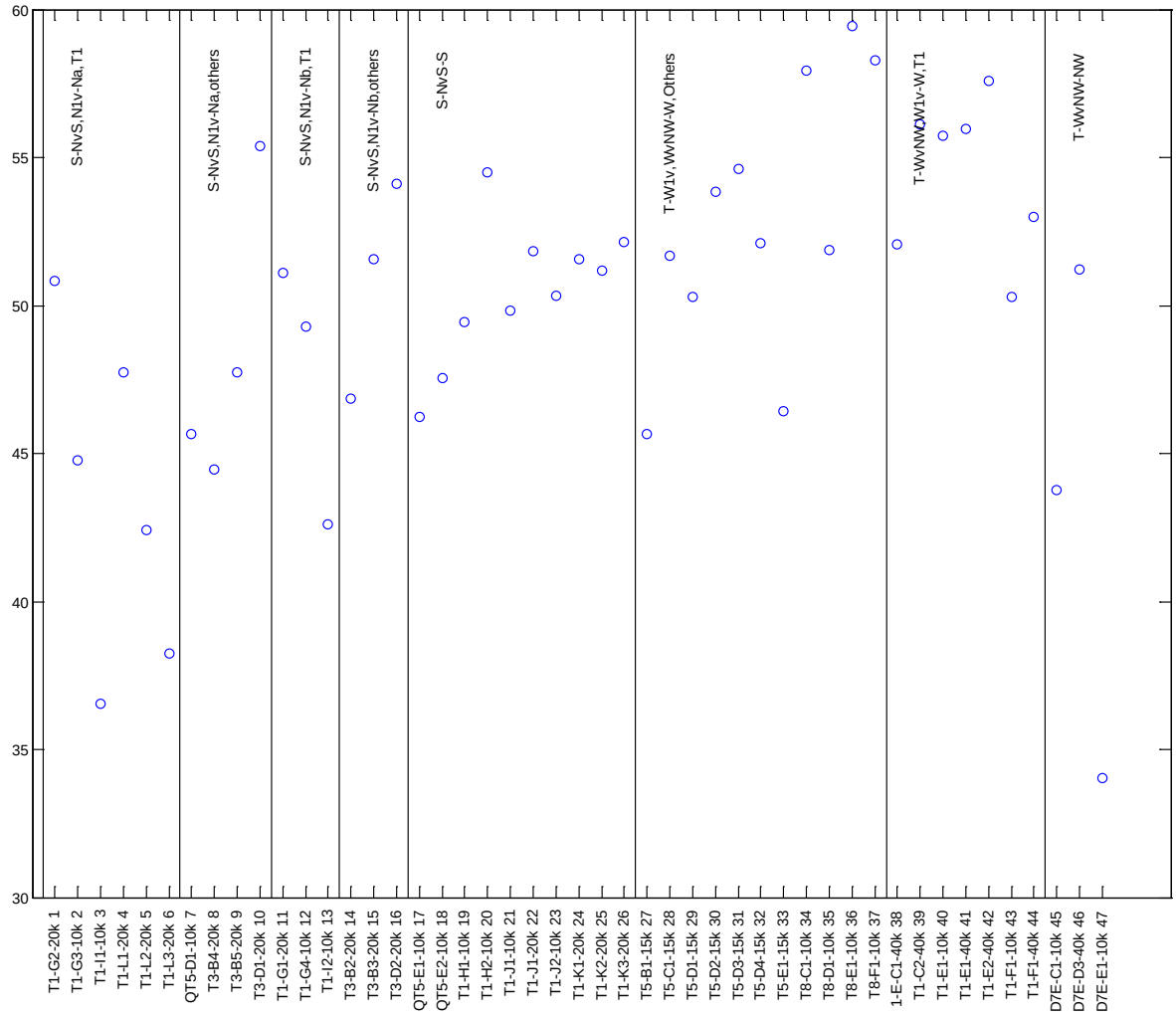

Figure 63: The standard deviation of the lamellar orientation angles (in degrees) of the images analyzed, divided by their type of surface. A standard deviation below 53 degrees signifies a narrow and non-uniform distribution. The large amount of variation found suggests there are no significant overall trends.

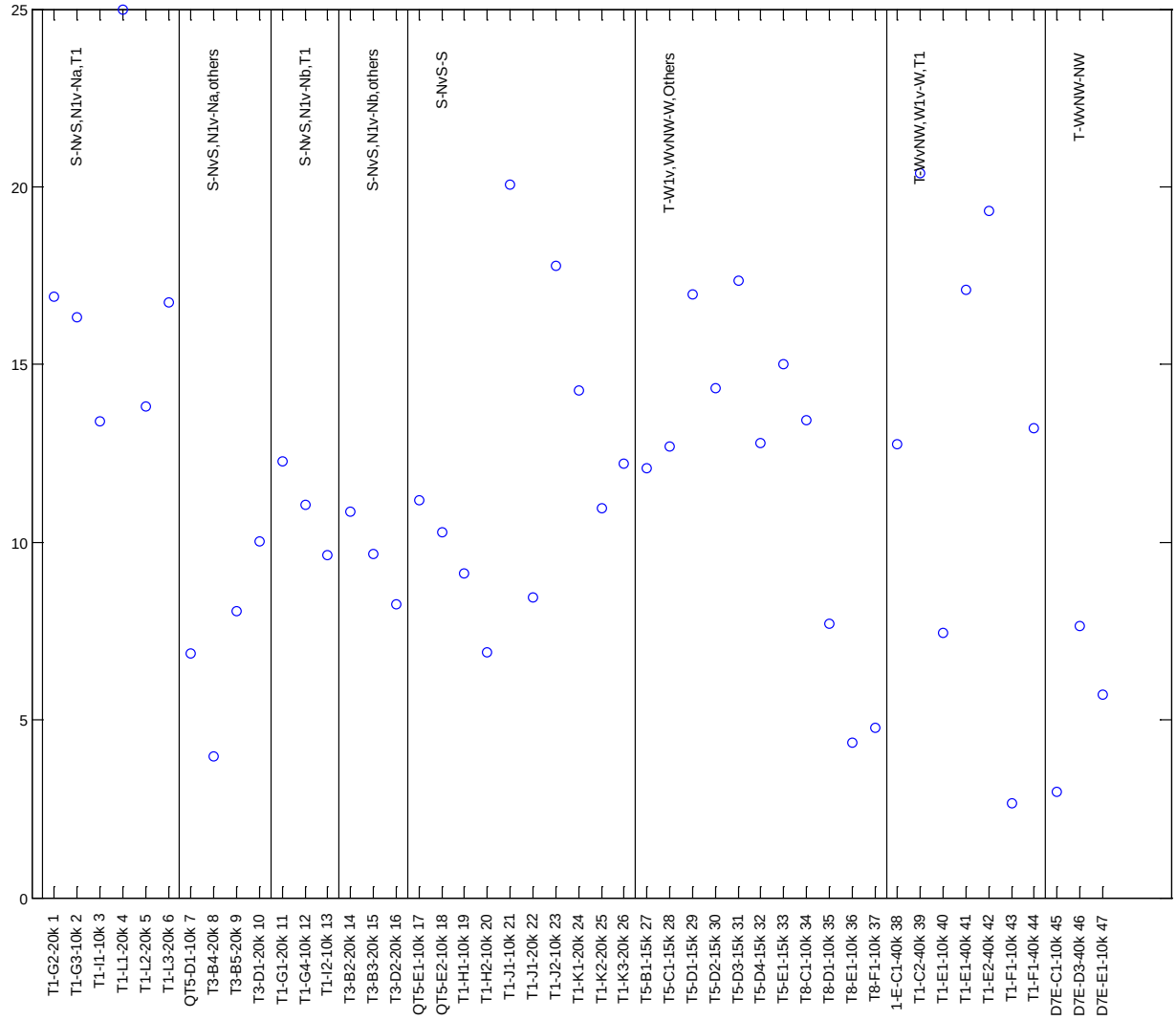

Figure 64: The percentage of each image analyzed that was detected to be an edge, grouped by type of surface. Differences in edge % would hint at differences in the amount of lamellae aligned parallel to the viewing surface. The large amount of variation found suggests there are no significant overall trends.

Table 12: Distributions of lamellar orientations for different motions. A random orientation would have an average and standard distribution of 90±53° for the lamellae orientation angles. The column titled “Variation” shows how much variation can be expected for a set of images collected in very close proximity to each other (from the wear surface of 2D+roll).

Surface type	Variation	Near-surface, upper		Near-surface, lower		Sub-surface	Wear surface			Non-wear surface
Motion type		1D	Rolling	1D	Rolling	1D	1D	2D+roll.	2D+roll.+rot.	no sliding
Ave. of the Orientation Means	99.5	88.7	80.9	90.8	90.4	89.0	82.9	98.1	100.5	101.8
StDev of the Orientation Means	4.61	3.37	2.96	1.87	4.27	4.67	5.60	7.99	4.06	15.83
Ave. of the Orientation StDevs	52.7	43.4	49.2	47.7	50.8	51.4	54.4	50.7	56.9	43.0
StDev of the Orientation StDevs	1.93	5.49	5.59	4.48	3.67	1.60	2.64	3.47	3.40	8.60
Average Edge %	15.4	17.0	7.3	11.0	9.6	12.5	13.3	14.5	7.6	5.5
StDev Edge %	2.18	4.18	3.09	1.32	1.31	4.63	6.44	2.11	4.19	2.34
# of images measured	4	6	3	3	3	8	7	7	4	3

FFT analysis of the microstructure images also revealed no additional evidence of orientation (Figure 65). The FFT images yields a central bright zone that faded into the surrounding black. For a few images, this central zone was slightly elongated, hinting that that particular image might have had small amount of orientation. Again, however, when looking across all the images, there was no conclusive evidence of orientation.

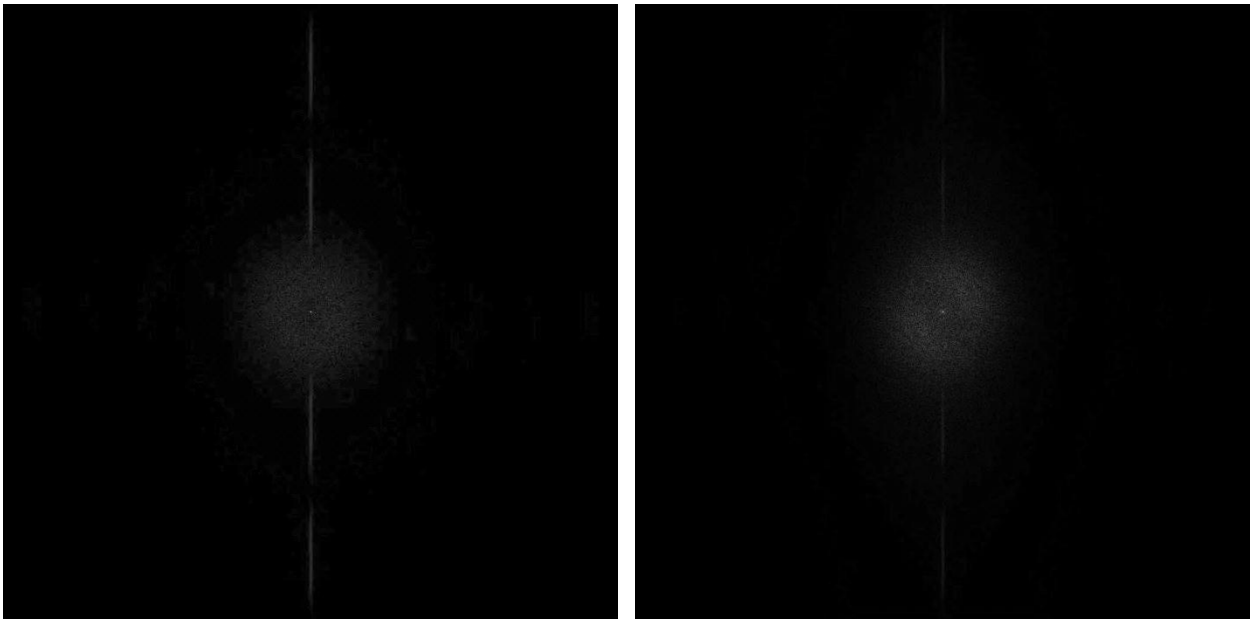

Figure 65: FFT analysis of the wear surface microstructure the different wear paths (the same images shown in Figure 62) showed no evidence of orientation: A) 1D sliding; B) 2D sliding + rolling +rotation. The vertical white line is an artifact from the image itself that appeared on essentially all the resulting images (likely from the scale bar).

5.3 - Discussion

Folding, surface cracks, and scratches are typical features of wear surfaces that have been reported in other *in vitro* and *in vivo* wear studies (Kilgour & Elfick 2009; Zhou & Komvopoulos 2005). Folding, or rippling, is related to adhesive wear mechanisms and the plasticity of the material, and may also play a role in the fatigue wear process. Zhou et al. has reported tighter fold packing and increased wear resistance as chain mobility of UHMWPE was reduced through radiation crosslinking (Zhou & Komvopoulos 2005) and the amount and type of rippling can also be influenced by the presence of cross-shear (Bragdon et al. 2001). The light scratching aligned with the motion direction suggests that some abrasive wear modes may also be present. Surface cracks are evidence of fatigue mechanisms, which would play a more important role in wear debris generation at a higher cycle count, once the cracks have time to grow large enough that they meet up with other cracks or the surface and generate wear particles. It is still unclear how the different wear modes are affected by multidirectional motion. For example, under reciprocating motion a surface crack would experience mode I crack opening in a consistent direction under the tensile wake of the sliding contact, while the direction of maximum principle stress would be changing under multidirectional sliding, slowing crack growth; although, the strain softening that would occur under multidirectional sliding could weaken the material and increase crack growth. Further investigation should be done into the relative prevalence of surface features under different combinations of motion and at different stages of wear.

Although the wear surfaces did have a burnished appearance, some scratching from the polishing step was still visible after the wear tests. The deepest scratches present on the polyethylene disk surface before the wear tests were on the order of a few microns (< 5 μm) while the wear scars were on the order of tens of microns and higher (25 to about 130 μm). Material removal (wear) of down to these depths should fully erase all evidence of the initial surface finish, so it is unclear why it is still visible. Any creep that the material undergoes should be recoverable, and there were only minor additional changes in wear scar dimensions after the 3 weeks of strain recovery–wear scars that were re-measured after 7 months of creep recovery were less than 3% smaller than measurements made after 3 weeks of creep recovery. Creep of UHMWPE under multiaxial loading has not been extensively studied, so it is unknown if the amount of permanent creep would vary with sliding motion. The peak contact stresses are slightly above yield at the start of the wear test (27 MPa vs. 22.3 MPa), but generally dropped below yield as the wear scar grew and the contact area increased. There might have been permanent, plastic deformation of the bulk material, especially if there was significant strain softening from the sliding friction forces. However, any “material loss” from creep or plastic deformation would have to have a corresponding “material gain” elsewhere on the wear scar. The slightly raised shoulders on the edges of the wear scars were taken into account when measuring the cross-sectional area of the wear scar and only affected the wear volume by a few percent. No additional raised areas were noticed at the ends of the wear scars (Figure 48 and

Figure 58), making it unlikely that permanent deformation is a significant component affecting the relationship of cross-shear and wear factor results presented here.

In regards to the microstructure, although some areas of the wear surfaces displayed slight degrees of alignment, the amount of change was too low and the variability was too large to account for the differences in wear. There was no strong evidence for lamellar alignment either on the wear surface or below the surface, parallel to the direction of sliding. Orientation of the lamellar edges for both types of surfaces was quantified using thresholding and filtering image analysis techniques as well as FFT image processing, and neither technique revealed consistent evidence for alignment. Neither were there consistent differences found in the relative areas of lamellae edges, a change which would have suggested alignment of lamellae parallel to the viewing plane.

Several aspects of the method used here to examine the microstructure may explain the absence of observed alignment and need to be discussed further: the image analysis of the lamellar edge area, the way the etching reveals lamellar edges, the amount of material the etchant removes, and the type of material the etchant removes. Using the percent of the image that is a lamellae edge as a proxy for lamellar alignment parallel to the viewing plane relies on a few assumptions that may not hold true. The main assumption is that the crystallinity of the surfaces being compared must be the same. While all the wear tests performed here were on the same batch of UHMWPE with identical processing, wear testing itself may deform the surface layer enough to break apart lamellae and induce de-crystallization (Kilgour & Elfick 2009). Differences in surface strain accumulation between the motions may have led to changes in crystallinity which may be cover up differences in the amount of lamellar alignment parallel to the viewing plane.

Alignment of lamellae parallel to the viewing plane may also be obscured in the way the etching procedure removes material to reveal predominantly lamellar edges. The etchant preferentially removes the amorphous phase that surrounds the crystalline lamellae. Lamellae that are perpendicular to the etched surface have one side that stays embedded in the material, but if all the amorphous material surrounding a lamellae is removed then there is nothing left to anchor it to the surface (Van Citters 2006). This may explain why SEM images of the etched surfaces show a predominance of lamellae oriented parallel to the viewing direction with only one edge exposed, even for areas of the material that should have completely random microstructure. However, even if the etching procedure removes most of the lamellae parallel to the viewing plane, this alignment should be visible in a perpendicular viewing plane, which was not the case here.

Additionally, the etchant could be removing too much of the material at the surface and erase evidence of alignment. However, this is likely not the case here for several reasons. Previous studies using TEM imaging of polyethylene microstructure following wear found that alignment was visible at depths of up to 9 μm (Edidin et al. 1999), while similar etching procedures on high density polyethylene have reported penetration depths of up to 2 μm (Olley et al. 1979). While a long etching time was used in this procedure and it is difficult to determine

the exact resulting etching depth for this polyethylene, shorter etching times did not reveal any alignment. Short etching times, on the order of 1-5 minutes on 1D sliding wear samples, revealed none of the lamellar microstructure. After 10 minutes of etching a 1D sliding + rotation sample, just enough of the amorphous phase had been removed to see hints of lamellae; after 20 minutes enough of the lamellae edges could be seen to approximate orientation. At least 30 minutes, and in some cases more, was needed to completely remove evidence of the amorphous phase and clearly reveal the lamellae. With no evidence of alignment at these shorter etching times it is unlikely that the etching procedure is removing enough of the material to penetrate past an aligned surface layer.

Finally, the etching procedure may not be appropriate for examining alignment due to the type of material it removes. While it predominantly attacks and removes the disordered amorphous material, the etchant can also remove "defective" crystalline regions and the procedure is also sensitive to lamellar orientation (Olley et al. 1979). Any lamellae that were strained enough to change their orientation may have enough dislocations to be defective enough to be attacked by the etchant. However, another microstructure analysis study using a similar etching and SEM imaging procedure on polyethylene pins articulating on CoCr plates (with variable loading up to 4.7 MPa and both linear and elliptical wear paths) was able to detect regions of fragmented lamellae with hints of alignment of non-crosslinked polyethylene, but only for unidirectional sliding – no evidence of alignment was detected for elliptical wear paths (Kilgour & Elfick 2009).

Alignment of UHMWPE from wear has more commonly been studied using other techniques, such as transmission electron microscopy (TEM), X-ray scattering techniques, and Fourier-transform infrared spectroscopy (FTIR). TEM is used to look at thin (~65 nm-thick) slices of polyethylene. Staining the slices in chlorosulphonic acid and then uranyl solution makes the edges of the lamellae visible (Figure 10) without removing the amorphous phase. This technique has been used to examine alignment direction and depth of alignment in wear tests of polyethylene pins (Zhou & Komvopoulos 2005), polyethylene disks (Crane 1998), polyethylene acetabular liners in joint simulators (Edidin et al. 1999), and retrieved polyethylene liners (Kurtz et al. 2000). X-ray absorption spectroscopy can be used to indicate the quantity of different types of bonds. By changing the angle of the specimen relative to the X-ray beam, the quantity of C-C backbone bonds at different orientations can be estimated, and this technique has been used on polyethylene wear pins (Sambasivan et al. 2004). Small-angle X-ray diffraction (SAXS) has been used to investigate alignment of polyethylene during compression testing, and similar methods should work for wear testing as well (A. Galeski et al. 1992). FTIR, when paired with a polarizing aperture, can also be used measure the orientation of polyethylene molecules. This technique has been used to investigate alignment in acetabular liner retrievals (Davey et al. 2004).

The additional techniques described here may be more appropriate for future investigations into texture development during wear than the etching method. For example, orientation analysis using X-ray and FTIR methods would include information about both the

amorphous phase as well as the crystalline phase, and the amorphous phase likely plays an important role in orientation. Further investigation about how polyethylene texture develops under multidirectional sliding and the role it plays on wear volume and wear particle size would guide development and improvement of UHMWPE such that it can be optimized for the amount of cross-shear in a specific joint, such as knees and shoulders.

Chapter 6: Summary and Conclusions

6.1 - Limitations of this study

The two main limitations in this study are related to inherent challenges of tribological testing in general: low sample size and range, and measuring total wear rate without evaluating wear debris size. The time intensive nature of testing a material designed to last 20 years leads to a limited number of motion parameters that could be tested and the number of repetitions ran for each set of parameters. The significance of this limitation is most apparent when comparing the different cross-shear parameters and their predictive capabilities when it comes to wear. The motion parameters for this set of experiments were selected based on the extremes of the kinematic conditions present in the knee, and while this was an appropriate first step to verify the tribo-system and evaluate the significance of cross-shear in the knee, it did not significantly differentiate the cross-shear definitions enough to enable a strong comparison between them. Although it is difficult to perform a meaningful statistical analysis when some motion combinations only have a sample size of 2 wear scars, some motion combinations had up to 6 wear scars tested. These tests showed levels of variation typical of wear testing of UHMWPE, although some outliers existed. Also, the difference was so large between the wear factors at the extremes of motions that the significance of cross-shear was clear.

The second limitation is how the UHMWPE wear factors are generally measured and used in the orthopaedic community. The only reason that wear is a concern at all is because of the biological immune response instigated by the wear particles that leads to osteolysis and implant loosening. The severity of the biological reaction is highly dependent on the wear particle size, concentration, material, and shape (AAOS 2000b). While the distribution of the wear particles' shapes and sizes can be measured by separating wear particles from the serum lubricant (Campbell et al. 1995) or using low angle laser light scattering (Elfick et al. 2000), these technique are difficult and time-intensive to implement. In order to isolate wear particles, the used serum lubricant needs to be recovered, digested using sodium hydroxide, the wear particles need to be separated out using density gradient ultracentrifugation, filtered, dried, and then they can be sputter coated, examined in an SEM, and the resulting images run through image analysis. Low angle laser light scattering can characterize a greater percentage of the total wear debris and may be quicker than SEM, but requires specialized equipment and still requires the bovine serum to be digested and concentrated. Very commonly, the wear debris distribution is simply assumed to be identical between the different materials or conditions being tested and the total wear volume, measured using either gravimetric or volumetric techniques, is taken as a proxy for the osteolytic potential and used as the basis of comparison (Van Citters et al. 2007; Galvin et al. 2006; Saikko 2006; Muratoglu, Merrill, et al. 2003). However, this is not always the case. For example, studies have shown that, on average, crosslinked polyethylene wear

particles are smaller than debris from non-crosslinked polyethylene (Williams et al. 2007). Another study showed that increasing the counterface roughness increases the minimum wear particle size (Elfick et al. 2001). In regards to cross-shear, this same study showed that the distributions of particle sizes from hip simulators were similar for both physiologic and simplified cycle profiles of loading and kinematics, and the same may be true for the different motion paths tested here.

6.2 - Strengths of this study

The three most significant strengths of this study are the tribo-system and wear testing conditions, the large number of cross-shear parameters evaluated, and the image analysis program. This tribo-system is the only non-joint-simulator, wear testing machine described in the orthopedic literature that can simulate all four types of motions relevant in knee replacements: anterior-posterior sliding, medial-lateral sliding, flexion-extension (rolling), and internal-external rotation. It simulates the complex *in vivo* contact conditions using an analogous yet much simpler ball-on-flat contact. This results in a similar Hertzian contact stress distribution and should enable similar lubrication film thicknesses. The location of the polymer component as the disk is analogous to an actual TKR and this subjects the polymer to a similar loading-unloading cycle. This type of contact also enables the simulation of realistic and specific kinematic parameters that can reproduce consistent and relevant values of cross-shear. This hybrid testing approach allows us to simulate realistic tribological conditions in a controlled environment and decouples the design of the implant and the performance of the material in a way that would not be possible with joint simulators.

The second major strength of this study is the number and type of cross-shear definitions that were analyzed: six different definitions for both total cross-shear and ratios of cross-shear, and all the parameters were re-formulated into the equivalent integral format. Even though the orthopaedic community has not yet agreed upon which parameters are most appropriate for evaluating UHMWPE wear, most studies only use one or two definitions. In this study, the most recent development in cross-shear modeling, the memory-based approach, was compared with the traditional, cycle-based approaches. The Matlab code that was developed to compute the cross-shear parameters was able to not only output the final magnitude and ratio of cross-shear but also compare the distribution of cross-shear within a cycle and across the contact zone to investigate how the type of motion and the definition used affected the final result. This type of comparison will also be useful in selecting motion parameters for future tests to will be able to differentiate between the definitions and test specific hypotheses.

The third major strength of this study was the image analysis used to minimize the subjective nature of examining microstructure. There can be a large amount of variation in the material itself just based on the processing technique and how a local area crystalized that small areas may display some degree of orientation naturally. Also, examining the microstructure by

eye can be unpredictable and subject that what the observer expects or what features happened to stand out. To reduce observer bias and the local variations in original microstructure, multiple images were taken for each sample at a wide range of magnifications and the orientation was quantified with three different methods using a custom LabVIEW image analysis code.

6.3 - Conclusions

The results from this study can be summarized in three main conclusions:

- The multidirectional tribo-system was able to simulate realistic contact conditions and show that cross-shear has a significant effect on the wear of UHMWPE in TKR, with more than an order of magnitude increase in wear factor between the smallest and the larger amounts of physiologically relevant cross-shear. The wear factors for the more complex motions were equal to neither the sum nor the product of the wear factors from the individual motions. The effect of motions on wear rates was only cumulative for combinations that had a low wear rate.
- For the kinematic parameters tested here, the traditional definition of cross-shear ($W_{\perp}$, the frictional work expended perpendicular to the primary molecular orientation), was not as good of a predictor of wear rate as the crossing intensity (σ) and the memory-based definitions of cross-shear (W_m and W_{ζ}). While many definitions of ratios of cross-shear showed good linear fits to wear factor, memory-based parameters such as Z^* appear to have the best combination of theoretical basis, robustness, and performance.
- The lamellar microstructure, revealed by etching away the amorphous phase, showed no consistent and significant evidence of texture development, either at the wear surface or below the wear surface. Other microstructure analysis methods, such TEM, SAXS, or FTIR, may be needed to fully analyze the wear mechanisms and phenomenologically explain the dependence of wear on cross-shear.

These results imply that cross-shear enhanced wear that results from TKR kinematics should not be neglected when considering the many design objectives of TKR. A better theoretical understanding of how kinematics contribute to wear can lead to better UHMWPE formulations, improved computer simulations of wear, and optimized TKR designs with longer life-spans.

6.4 - Suggestions for future work

This study was the first set of experiments to take advantage of the full capabilities of the multidirectional tribo-system. There are several other interesting and important questions that could be examined using this setup. These include further analysis that could be performed on the wear samples from this set of experiments, continued improvements and validation of the

tribo-system and testing methodology, expanding the sample size and range of testing parameters, and characterizing the testing conditions more completely.

Texture development of the wear samples from this set of experiments was thoroughly examined and little evidence was found of consistent trends. Additional SEM imaging of the etched surfaces may result in enough statistical significance to detect slight differences and trends, but further investigation into texture development of the available samples would likely require a new approach, such as TEM or X-ray scattering. Additionally, the surface features on a wear scar can yield important clues amount the sliding conditions and the wear mechanisms present. General features of the wear surfaces were examined, but a more detailed analysis of a greater number of samples for all types of motion could be performed. This would lead to trends in the frequency of occurrence for the folds, surface cracks, and scratches, as well as things like fold wavelength and orientation. These trends could yield insights as to how the dominant wear mechanisms change under different cross-shear conditions.

One surface feature that should be investigated to more fully validate the testing methodology is the retention of the some of the features of the original surface finish. Examining the creep and plastic behavior of the polyethylene disk under the same loading conditions but without the motions would help differentiate the contributions of material removal and material deformation in final wear scar profile. Running tests on polyethylene disks with different surface finishes, such as leaving them as machined, and other wear measurement techniques, such as gravimetric or wear particle analysis (although they come with their own set of challenges) may be useful in this endeavor as well. Also, running some tests to a much higher number of cycles may be needed before the role of fatigue on wear rate becomes apparent.

The motion parameters for this set of experiments were chosen based on the extremes of *in vivo* kinematics, and many of the cross-shear measures were not significantly different enough under these conditions to conclusively demonstrate superiority of a particular method. Different values of motion, such as “figure 8” paths with narrower crossing angles, fully rolling motion, and greater rotation rates, should be tested to better fill out the plots of cross-shear ratio and wear factor. In order to differentiate between some of the cross-shear definitions, some parameters outside the range of what is physiologically relevant may need to be tested. Kinematic settings should first be evaluated with the cross-shear calculation code in order to confirm that the chosen motion parameters will result in an appropriate differentiation between the definitions. The motion parameters should also be chosen such that the same level of cross-shear is reach by different combinations of motion (1D sliding + rotation and 2D sliding, for example). This tribo-tester should also be used to improve upon the existing definitions by more fully investigating the role of load and the wear mechanisms present at different contact pressures, and test if the distance needed for alignment in the memory-based parameters is dependent on load. Evaluating the effect of cross-shear on other materials, such as cross-linked polyethylene and polycarbonate-urethane (Khan et al. 2005; Geary et al. 2008), would be very useful for guiding further improvements in joint replacement longevity and performance. Of course, as with all tribological testing, the time needed to run a wear test can be a significant limiting factor.

In order to better guide future testing and aide in interpreting results, the contact conditions, specifically the contact pressure, shear stress, friction, and lubrication film thickness, should be studied further. The static contact pressure has been modeled using finite element analysis, but software complications prevented successful analysis of sliding contact under the presence of friction. Friction from sliding would tend to increase the tensile forces behind the point of contact and move the maximum sub-surface shear stresses closer to the surface (Barbour et al. 1997). A different distribution in contact pressure and friction force would affect the prediction of frictional work expended during sliding and the calculations of cross-shear. The cross-shear calculations are also dependent on the coefficient of friction itself. Creating a Stribeck curve for this contact condition by measuring the coefficient of friction as function of load and sliding velocity would give more insight into the frictional work model. For this set of experiments a constant coefficient of friction was assumed but the friction forces may vary throughout the contact zone because of differences in the fluid film layer. Fluid film thicknesses of two-dimensional rolling or sliding contact with Newtonian fluids have been well studied and can be modeled using the Reynolds equation or numerical models (Kennedy et al. 2007). However, three-dimensional models of non-Newtonian fluids (such as synovial fluid) under sphere-on-flat compliant contact with a range of slide-roll ratios and rotation speeds have not been well studied. Recently, some experimental studies have investigated film thicknesses of synovial fluid and bovine serum lubrication in a metal-on-metal sphere-on-flat contact under pure sliding and pure rolling (Mavraki & P M Cann 2009; Mavraki & P.M. Cann 2011), as well water and other lubricants in polymer-on-metal, sphere-on-flat contact under rolling and sliding (Connor Myant, Fowell, et al. 2010; C. Myant, Spikes, et al. 2010). Computational fluid dynamics models of the tribological conditions simulated by the multidirectional tribo-system would enable more accurate cross-shear calculations and aid in the evaluation of wear mechanisms. The would also enable the wear rate to be evaluated individually across the entire wear surface instead of an average wear rate at the middle cross-section of the wear scar.

Appendix A: A Case Report

Delamination of a Cross-linked Polyethylene Liner Associated with Titanium Deposits on the CoCr Femoral Head Following Dislocation

Abstract

Retrieval studies of total hip replacements with cross-linked ultra-high molecular weight polyethylene (cross-linked ultra-high) liners have shown much less surface damage than conventional ultra-high molecular weight polyethylene (conventional ultra-high) liners. A recent revision surgery for a hip replacement with frequent dislocations revealed a cross-linked ultra-high liner with a large area of delamination. To determine the cause of this unusual surface damage, we analyzed the bearing surfaces of the CoCr femoral head and cross-linked ultra-high liner with scanning electron microscopy, energy dispersive x-ray spectroscopy, and optical profilometry. We concluded that the titanium acetabular shell scraped against the CoCr femoral head during the dislocations and not only roughened the femoral head but also transferred many deposits of titanium. The largest deposits were 1.6-4.3 μm higher than the surrounding surface and could lead to increased stresses, and therefore increased wear and damage, in the cross-linked ultra-high liner. This case illustrates that dislocations can leave titanium deposits on CoCr femoral heads and that cross-linked ultra is still susceptible to surface damage.

Introduction

Cross-linked and thermally stabilized ultra-high molecular weight polyethylene (cross-linked ultra-high) has been replacing conventional (gamma barrier) ultra-high molecular weight polyethylene (conventional ultra-high) as the bearing material of choice for acetabular liners since 1998 (Kurtz et al. 1999). Many studies have shown that cross-linked ultra-high wears much less than conventional ultra-high under both smooth (McKellop, F. W. Shen, et al. 1999; Muratoglu, Bragdon, D. O. O'Connor, Perinchief, et al. 2001) and roughened conditions (McKellop, F.-W. Shen, et al. 1999; Saikko et al. 2002). Retrieval studies of cross-linked ultra-high liners have shown comparatively little damage (Salineros et al. 2007; Muratoglu, Greenbaum, et al. 2004), although surface cracking and small delamination has been reported on some retrievals (Bradford et al. 2004).

Recently, a cross-linked ultra-high liner and CoCr femoral head were retrieved after dislocating five times and sent to our lab for analysis. The implant was only *in vivo* for five months, but the damage to the liner included an area of delamination substantially larger than any previously-reported surface damage for cross-linked ultra-high used in the hip. Delamination is a fatigue wear process characterized by removal of sheet-like pieces of material and is associated with subsurface crack growth. Areas of delamination decrease the conformity further and can lead to accelerated failure (Muratoglu, Burroughs, et al. 2004). Delamination of ultra-high is more common when used for tibial inserts where contact stresses are higher than in the

hip, and the hertzian contact results in a maximum subsurface stress (Kennedy et al. 2003). This delamination has historically been secondary to radiation-induced oxidation. This retrieved hip implant was investigated to determine the source of its early surface damage.

Although roughening of CoCr femoral heads can occur with routine *in vivo* use (Ito et al. 2010), dislocations may cause more severe damage to the femoral head because of contact between the femoral head and metal acetabular shell (Bowsher et al. 2008; Kop et al. 2007; Jaffe et al. 2009). It was hypothesized that the damage to the liner was due to titanium transfer deposits and roughening of the femoral head from contact with the rim of the acetabular shell during the dislocations. The retrieval was analyzed using optical microscopy, scanning electron microscopy (SEM), and energy dispersive x-ray spectroscopy (EDX) to characterize damage and material transfer. Additionally, the topography of the femoral head was characterized with an optical profilometer.

Case Report

A 52-year-old woman (BMI: 31), who had undergone resurfacing hip arthroplasty in October 2004, developed loosening and underwent a revision total hip arthroplasty in January 2008. The implant was an Alloclassic® stem (Zimmer, Warsaw, IN) with a 36 mm Co-28Cr-6Mo femoral head and Longevity® highly cross-linked ultra-high liner (10 Mrad of e-beam radiation, re-melted above 135°C) with a 58 mm Trabecular metal™ shell (tantalum porous coating on Ti-6Al-4V backing). One month after surgery, the patient dislocated posteriorly, and within the following three-month period dislocated four more times. All dislocations were closed reduced in the emergency room within two to three hours. In June, 2008, (five months after implantation) the hip was revised for instability. During the revision surgery, it was determined that the components were well positioned and that the dislocations were a result of soft tissue instability. The head and liner were removed and a constrained socket implanted. Microscopic examination of the periarticular soft tissue cultures showed no signs of acute inflammation and cultures were negative.

The liner and femoral head were examined visually using optical microscopy (Sony XCD-SX910, Tokyo, Japan) and scanning electron microscopy (SEM) (Hitachi TM-1000, Schaumburg, Illinois). To determine if material had transferred, both components were also analyzed using SEM (FEI Company, XL-30 ESEM-FEG Hillsboro, Oregon) in combination with EDX (EDAX, EDS Detector, Mahwah, NJ).

The topography of the CoCr femoral head was quantified using a Wyko NT3300 profiling system (Veeco, Plainview, NY). This profiling system is a white-light interferometer that can measure surface heights with a 10-30 nm resolution and measure in the surface plane with micron-scale resolution. The topography data was analyzed using the accompanying Vision32 post-processing software (Veeco, Plainview, NY). For each measurement site, small areas of missing data were interpolated, and tilt and curvature were removed based on the adjacent un-scraped area. Accuracy of the interferometer measurements was confirmed using a stylus profilometer (Dektak IID, Sloan Technology Co., Santa Barbara, CA).

Analysis of the Acetabular Liner

Damage was prevalent on the liner bearing surface (Figure 66A). The greatest damage to the cross-linked ultra-high liner was a 4x6 mm area of delamination on the anterosuperior region (Figure 66B). Pitting, scratching, and abrasion (Figure 67) were prominent over approximately 30%, 50%, and 90% of the bearing surface, respectively. One instance of third-body CoCr debris (about 10 µm thick and 40 µm in diameter) was also found embedded in the cross-linked ultra-high liner.

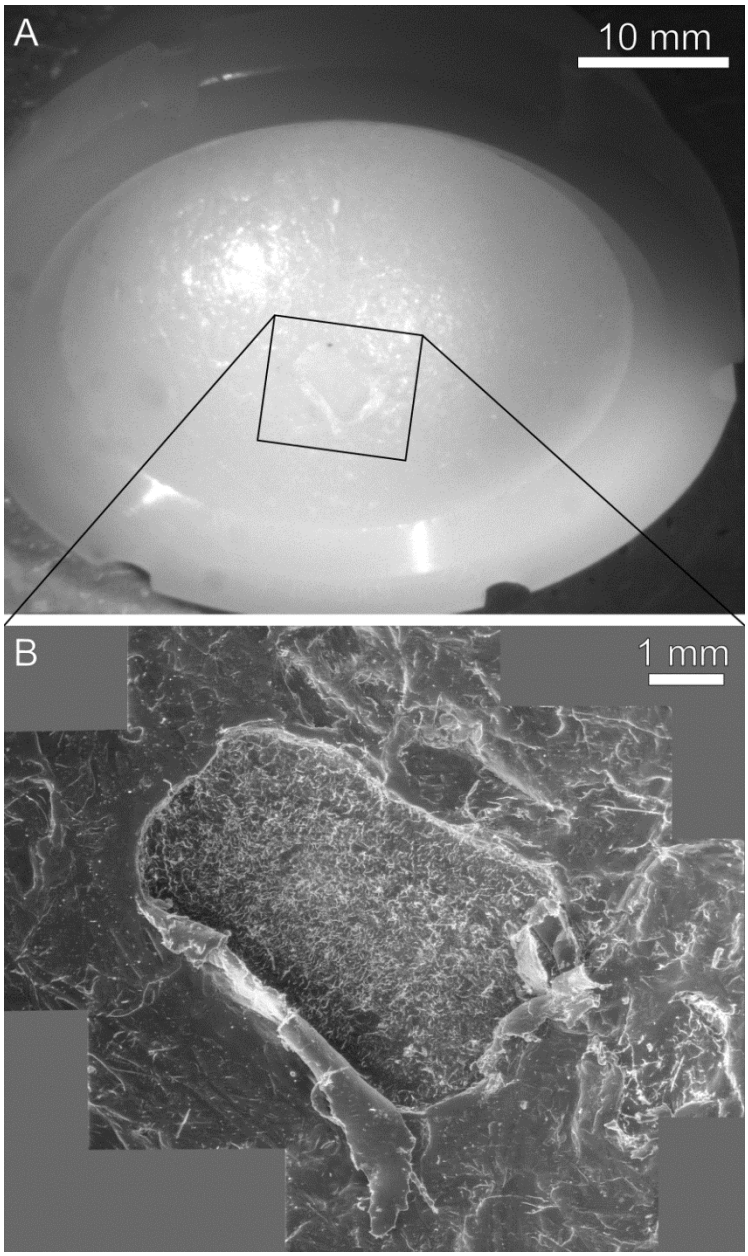

Figure 66: Delamination of the cross-linked ultra-high liner after only five months *in vivo*. A) Pitting, scratching, and abrasion were prevalent on the bearing surface and are visible in the portion of the figure with reflected light. B) Composite SEM image of the large area of delamination.

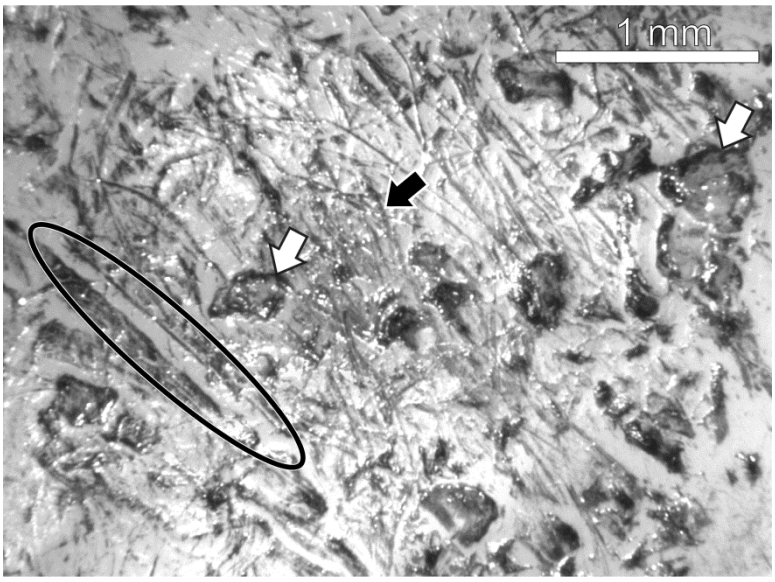

Figure 67: Damage to the cross-linked ultra-high liner, including scratching (black oval), pitting (white arrows), and abrasion (black arrow). Black ink was used to make surface features more visible.

Analysis of the Femoral Head

The femoral head exhibits readily visible markings over a 10x25 mm area on the articulating portion (Figure 68). The marks are 200-500 μm wide and 2-10 mm long, and are likely from the femoral head scraping against the acetabular shell during the dislocations and reductions.

EDX analysis of the scrapes reveal many areas of titanium deposited on the CoCr surface (Figure 69 and Figure 70). SEM images indicate that the typical deposits are oblong with a length scale of 15-50 μm. Many small deposits have length scales in the 3-7 μm range and the largest deposits have length scales of 100-300 μm.

Topography analysis of the scrapes corroborates the presence of raised deposits and roughening (Figure 68: I-III), but also reveals that some portions of the scrapes have an average surface level lower than that of the adjacent un-scraped surface. The scraped surfaces are 0.5-0.75 μm below the un-scraped surface and the tallest transfer peaks are 1.6-4.3 μm above the local scraped surface.

To quantify the change in topography, three measurement sites (Figure 68: I-III) were divided into scraped and un-scraped regions. Four area roughness parameters from each region were calculated (Figure 71): average roughness (Ra), total roughness (Rt), peak height (R_p), and skew (R_{sk}). All roughness parameters in the scrapes, except the skew, were greater than their neighboring un-scraped areas (Figure 72).

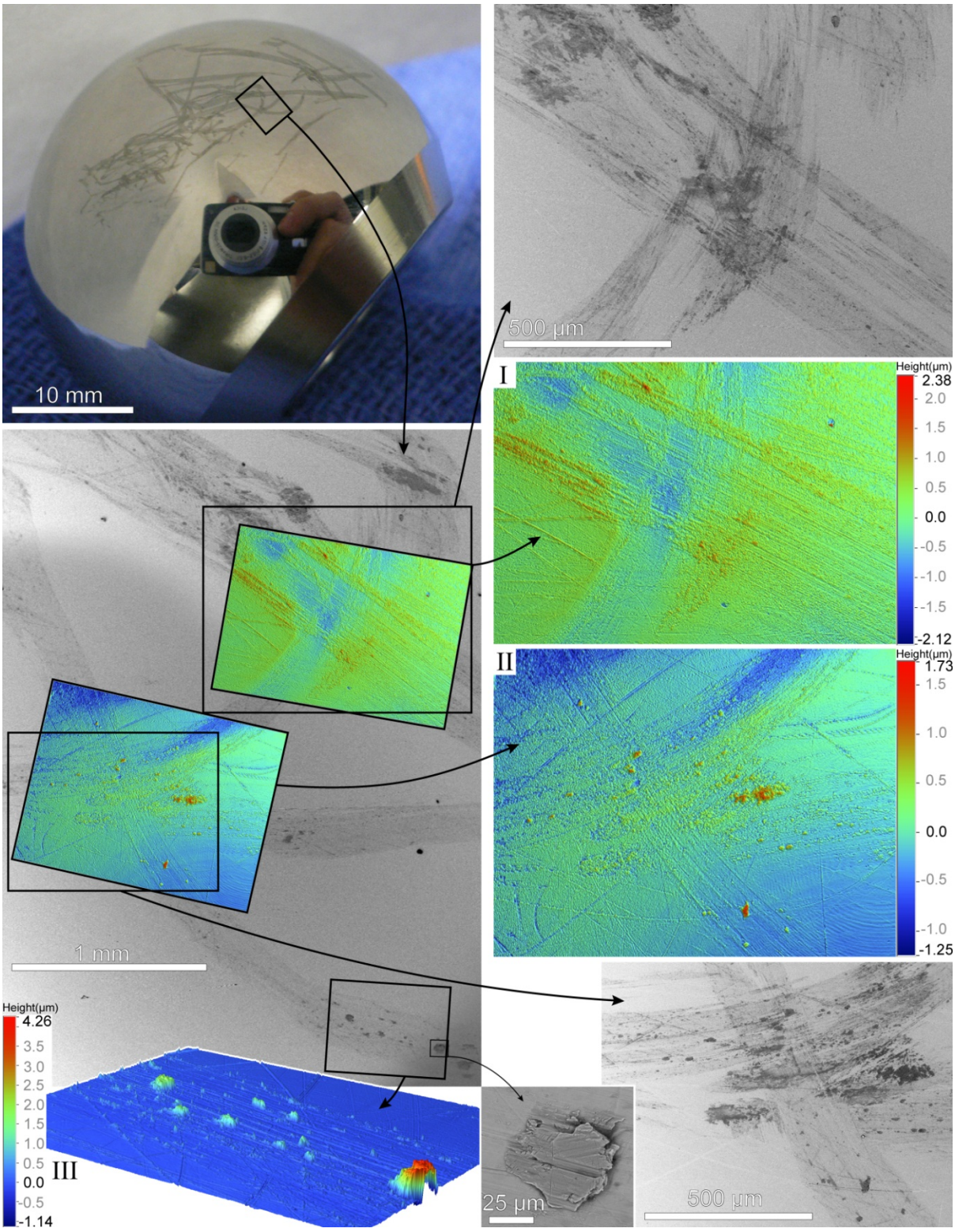

Figure 68: Optical, SEM and profilometry analysis of the damage to the CoCr femoral head. Several marks are easily visible; macroscopically they appear to be scratches. I-III) However, topography maps of scraped regions on the femoral head show increased roughness from scratching into the surface as well as from deposits on top of the surface. The heights on the legends are measured from the un-scraped areas at each location. Note: the height-axis for image III is magnified compared to the horizontal axes.

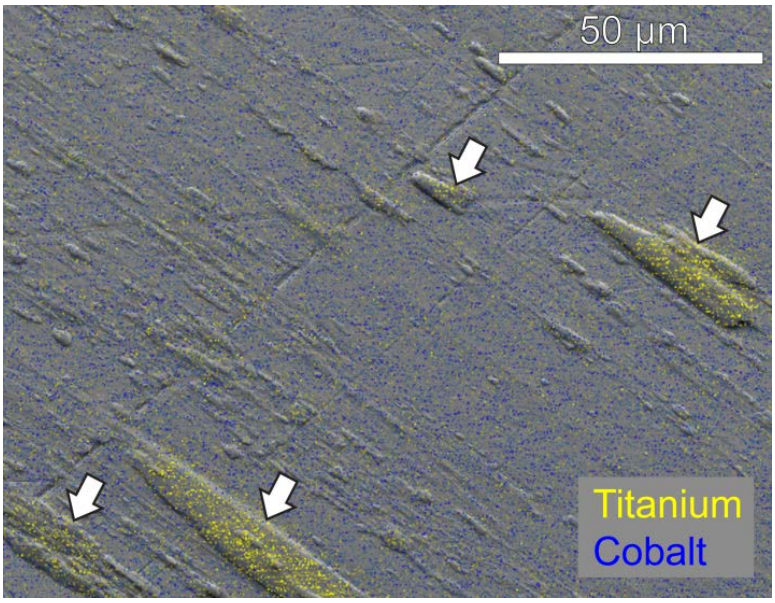

Figure 69: An SEM image with overlaid EDX field map shows the raised areas are titanium deposits (arrows) on top of the CoCr surface. Yellow pixels represent areas where titanium was detected and the blue pixels are where cobalt was detected. A previous scratch, presumably from normal use before the dislocation, runs underneath these deposits.

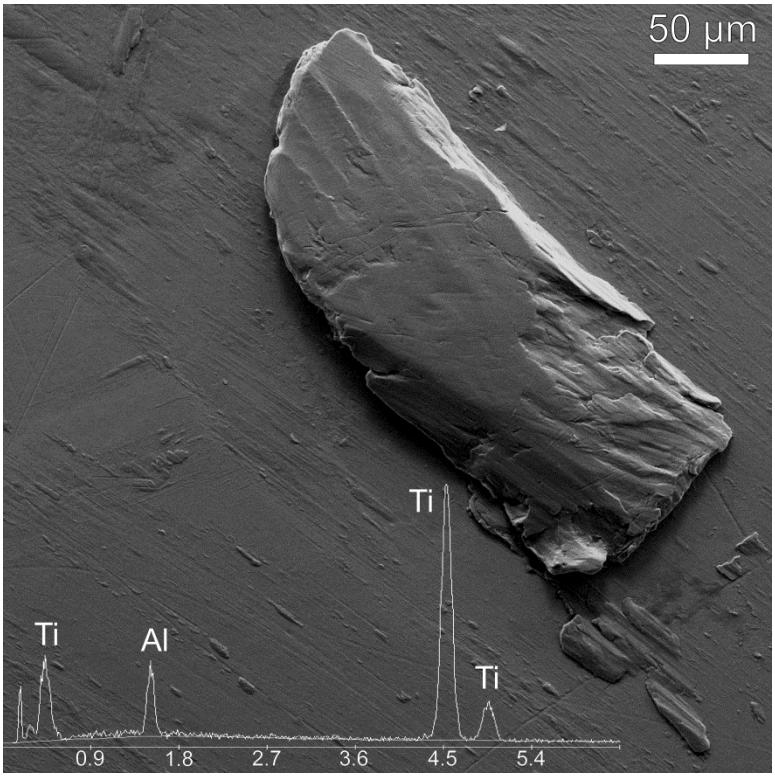

Figure 70: SEM image and EDX analysis of a large titanium deposit (120 µm x 300 µm) on the femoral head.

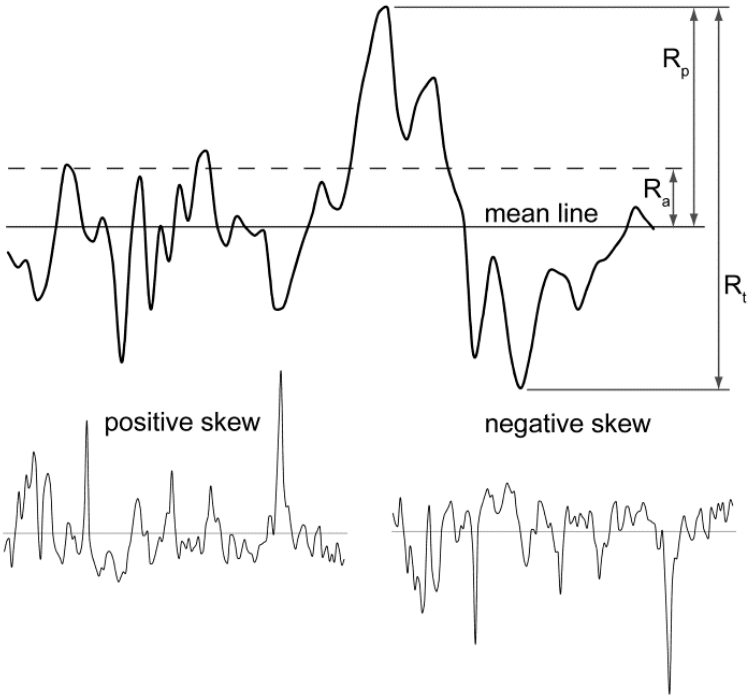

Figure 71: Schematic illustrations describing the roughness parameters used to describe the topography of the femoral head surface. Average roughness (R_a) is the average deviation from the average surface level. Total roughness (R_t) is the height difference between the highest peak and lowest valley within one sample. Peak height (R_p), is the highest point within one sample. Skew (R_{sk}) is a measure of how many peaks there are compared to valleys. See Hall et al. (Hall et al. 1997) for more detailed descriptions.

In addition to the change in roughness, the size of the deposits was also characterized. Deposits were isolated by defining continuous areas with a greater height than a threshold height above the un-scraped surface. Threshold heights were chosen for each measurement site as the minimum height that would isolate the main peaks. Four size parameters were calculated for each deposit: peak height, area, volume, and aspect ratio (peak height divided by half-width). These parameters measure the size of the deposit above the adjacent un-scraped surface. The sizes of the five deposits with the greatest volume from each of the three measurement sites are illustrated in Figure 73. Deposit volume is directly related to peak height and area, and so correlates with both (r^2 = 0.83, 0.75, respectively). However, the other parameters did not correlate strongly with each other (r^2 = 0.005-0.39). For example, the peak from measurement site II with the most area also has a large volume, but the lowest aspect ratio and only a moderate height.

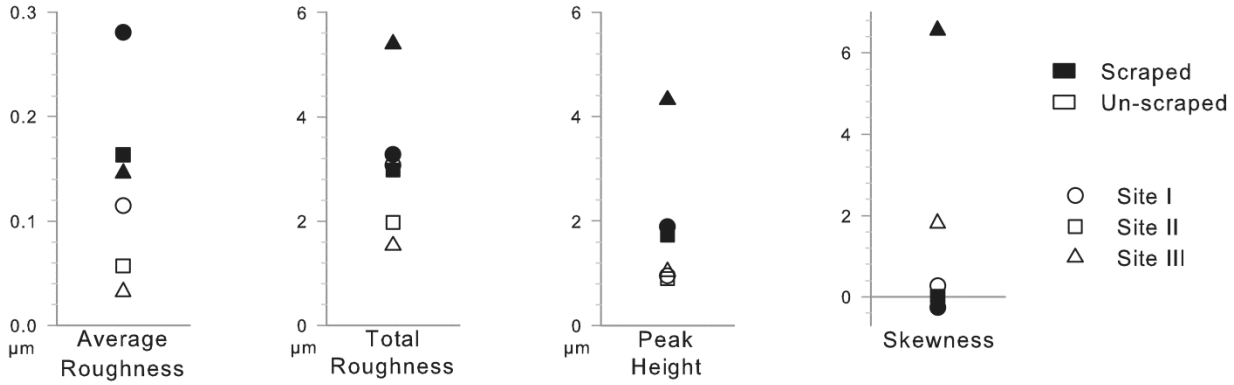

Figure 72: Roughness measurements of the scraped and un-scraped regions of three measurement sites. The peak heights are measured from the un-scraped average surface height.

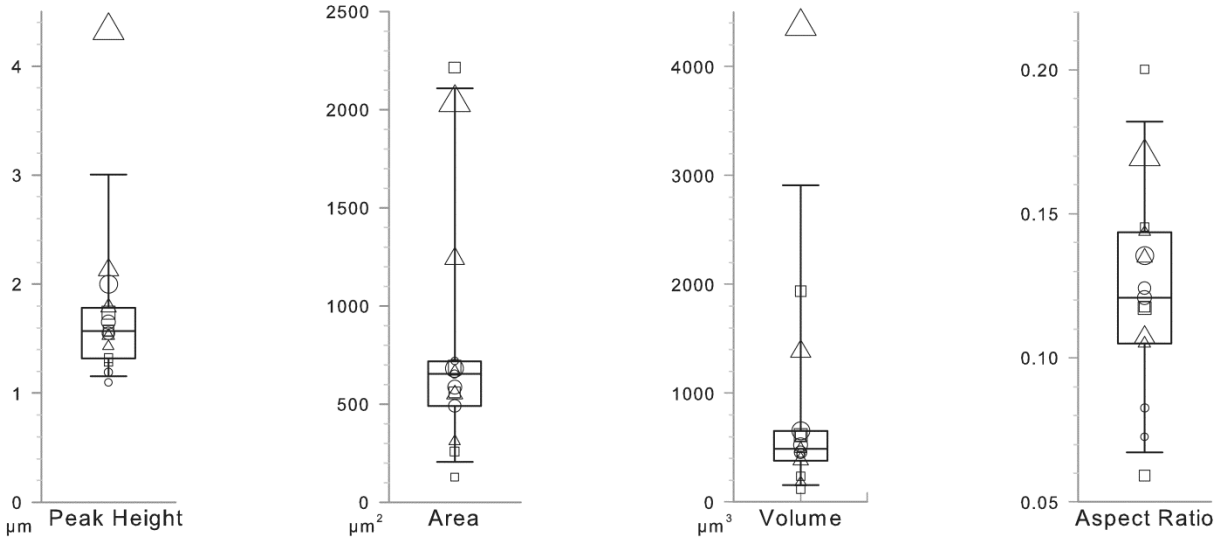

Figure 73: Size of the five peaks with the largest volume within each of the three sample sites (15 peaks total). The boxes mark the median and inner quartiles and the whiskers mark the 10th and 90th percentiles. The size of the marker for each peak corresponds to its height, and the shape shows which of the three sample sites the peak was from (see legend in Figure 72).

Discussion

The findings in this case indicate that as the acetabular shell made contact with the femoral head during the dislocations and reductions, it scraped across the bearing surface, leaving behind roughened areas and deposits of titanium. These damaged areas of the femoral head then articulated against the liner and likely caused the large amount of surface damage and delamination seen on the liner.

The titanium deposits would be expected to increase damage to the cross-linked ultra-high more than an increase in the average surface roughness associated with routine *in vivo* use, since the deposits are much higher than the surrounding material. McNie et al. (McNie et al. 2000) found that asperities with higher aspect ratios increase the magnitude of plastic strain in conventional ultra-high. Also, asperities with a larger cross-sectional area (which correlates with asperity volume in Figure 73, $r^2 = 0.97$) increase the amount of conventional ultra-high wear debris more than asperities with smaller cross-sectional areas.

It should be noted that using a single roughness parameter to compare surfaces can be misleading. Average measurements, such as R_a, describe the average feature size and are relatively easy to use, but misrepresent non-uniform topographies and do not describe the distribution of the roughness. Extremity measurements, such as R_p or R_t, only describe the most extreme points and may not distinguish between peaks and valleys. Skewness, R_{Sk}, (a relative parameter) better correlates with wear (Hall et al. 1997; Affatato et al. 2006) by describing the distribution of peaks and valleys on the surface, but does not describe the size scale of the features. While all parameters can be sensitive to the location and size of measurement sites (Que & Topoleski 1999), three-dimensional profilometry is better than two-dimensional profilometry for capturing information about deposits (Jiang et al. 1999). A combination of roughness parameters measured at several sites using 3D techniques is likely the most appropriate method to characterize and compare bearing surfaces for orthopaedic joint replacements. For example, although measurement site I had the greatest average roughness, the skewness reveals that this roughness is mainly from valleys and that site III, which had the lowest average roughness, has the highest peak. This study is a step toward reporting multiple roughness parameters in retrieval analysis.

The sizes of the deposits and roughness measurements in this retrieval are comparable to previous reports in the literature. Ito et al. (Ito et al. 2010) measured mean peak-to-valley heights (R_z) of 3.72±0.64 μm and roughness measurements (R_a) of 0.54±0.1 μm on CoCr heads after recurrent dislocations. Bowsher et al. (Bowsher et al. 2008) reported titanium transfer deposits of up to 1 μm high and 25 μm across on dislocated metal-on-metal hip implants and roughness measurements (R_a) of up to 0.304 μm. On dislocated ceramic heads, titanium deposit heights of 3 μm have been reported by Kim, Ritchie, and Hardaker (Y.-H. Kim et al. 2005) and 5 μm by Luchetti et al. (Luchetti et al. 1998).

From this case report, clinical implications can be drawn relevant to three areas: wear of cross-linked ultra-high, fatigue behavior of cross-linked ultra-high, and dislocation damage to metal heads. The significant amount of damage present and short time *in vivo* mean that most of

the total volume of wear is likely from the delamination. Often, surface damage is only evident because there has been little wear (McKellop 2007; Muratoglu et al. 2003). However, the wear volume would likely be much larger than it would for a smooth head had it been *in vivo* for a longer time, due to the raised peaks of the titanium deposits. Fisher et al., McNie et al., and Dowson, Taheri, and Wallbridge have demonstrated that the build-up of material at the edges of scratches greatly increased the wear of conventional ultra-high during uni-directional pin-on-disk wear tests (Fisher et al. 1995; McNie et al. 2000; Dowson et al. 1987).

Although cross-linked ultra-high has demonstrated improved adhesive and abrasive wear, it has sacrificed resistance to fatigue crack propagation in the bulk material and is more susceptible to fracture in the presence of flaws than conventional ultra-high (Baker et al. 2003; Furmanski et al. 2009). Asperities, such as the titanium deposits with large volumes or high aspect ratios, can increase the plastic strain of the sub-surface bulk material (McNie et al. 2000). This increases fatigue wear that can lead to delamination and pitting, which may explain the increased damage observed in this case.

Metallic transfer is often reported in studies of dislocated ceramic heads (Y.-H. Kim et al. 2005; Yoo et al. 2004; Della Valle et al. 2004), but the majority of studies on dislocated metallic heads only describe the damage as visible stripes or surface roughening (Ito et al. 2010; Schuh et al. 2006; Verioti et al. 2009). Titanium transfer to metallic heads has been reported in one other case (Bowsher et al. 2008) and in one *in vitro* study (Chang et al. 2008). This difference in reporting may be related to the similar appearance between scratching on a metal head and metal deposits on a metal head. This case retrieval shows the severity of damage to a cross-linked ultra-high liner that can occur in association with metal transfer deposits on a CoCr femoral head.

Metallic deposits on ceramic heads have been shown to increase the damage and wear to cross-linked ultra-high liners (Jaffe et al. 2009; Y.-H. Kim et al. 2005; Della Valle et al. 2004). Caution and close monitoring has been recommended following dislocation of ceramic femoral heads (Jaffe et al. 2009; Schuh et al. 2006), and this case illustrates that similar monitoring is appropriate for metallic femoral heads.

References

AAOS, 2000a. What design factors influence wear behavior in total knee replacement? In T. M. Wright & S. B. Goodman, eds. *Implant Wear in Total Joint Replacement: Clinical and Biologic Issues, Material and Design Considerations*. pp. 303-312. Available at: http://web.archive.org/web/20020605163356/http://www3.aaos.org/implant/implant.cfm.

AAOS, 2000b. What specific features of wear particles are most important in determining the adverse biologic reactions? In T. M. Wright & S. B. Goodman, eds. *Implant Wear in Total Joint Replacement: Clinical and Biologic Issues, Material and Design Considerations*. pp. 94-105. Available at: http://web.archive.org/web/20020605163356/http://www3.aaos.org/implant/implant.cfm.

AMTI, Advanced Mechanical Technology Technology, Inc. Available at: amti.biz.

ASTM, 2006. *F 732-00: Standard Test Method for Wear Testing of Polymeric Materials Used in Total Joint*,

Affatato, S. et al., 2006. The Predictive Power of Surface Profile Parameters on the Amount of Wear Measured In Vitro on Metal-On-Polyethylene Artificial Hip Joints. *Proceedings of the Institution of Mechanical Engineers, Part H: Journal of Engineering in Medicine*, 220(3), p.457-464. Available at: http://journals.pepublishing.com/openurl.asp?genre=article&id=doi:10.1243/09544119JEIM95.

Affatato, S. et al., 2008. Tribology and total hip joint replacement: current concepts in mechanical simulation. *Medical engineering & physics*, 30(10), p.1305-17. Available at: http://www.ncbi.nlm.nih.gov/pubmed/18774742.

Archard, J., 1953. Contact and rubbing of flat surfaces. *Journal of applied physics*, (3). Available at: http://link.aip.org/link/?JAPIAU/24/981/1 [Accessed September 23, 2010].

Argon, A.S., Galeski, a. & Kazmierczak, T., 2005. Rate mechanisms of plasticity in semi-crystalline polyethylene. *Polymer*, 46(25), p.11798-11805. Available at: http://linkinghub.elsevier.com/retrieve/pii/S0032386105013960 [Accessed March 14, 2012].

Atwood, S.A., 2010. *Microstructure, Mechanical Behavior, and Clinical Trade-offs in Ultra-High Molecular Weight Polyethylene for Total Joint Replacement*. University of California, Berkeley.

Atwood, S.A. et al., 2011. Tradeoffs amongst fatigue, wear, and oxidation resistance of cross-linked ultra-high molecular weight polyethylene. *Journal of the mechanical behavior of biomedical materials*, 4(7), p.1033-45. Available at:

http://linkinghub.elsevier.com/retrieve/pii/S1751616111000579 [Accessed October 12, 2011].

Baker, D.A., Bellare, A & Pruitt, L.A., 2003. The effects of degree of crosslinking on the fatigue crack initiation and propagation resistance of orthopedic-grade polyethylene. *Journal of biomedical materials research. Part A*, 66(1), p.146-54. Available at: http://www.ncbi.nlm.nih.gov/pubmed/12833441.

Banks, S.A. & Hodge, W.A., 2004. Implant Design Affects Knee Arthroplasty Kinematics during Stair-stepping. *Clinical Orthopaedics and Related Research*, 426(426), p.187-193. Available at: http://content.wkhealth.com/linkback/openurl?sid=WKPTLP:landingpage&an=00003086-200409000-00030 [Accessed September 23, 2010].

Barbour, P.S.M., Barton, D.C. & Fisher, J., 1995. The influence of contact stress on the wear of UHMWPE for total replacement hip prostheses. *Wear*, 181-183(1), p.250-257. Available at: http://linkinghub.elsevier.com/retrieve/pii/0043164895900314.

Barbour, P.S.M., Barton, D.C. & Fisher, J., 1997. The influence of stress conditions on the wear of UHMWPE for total joint replacements. *Journal of materials science: Materials in medicine*, 8(10), p.603–611. Available at: http://www.springerlink.com/index/PGN4H71065315168.pdf.

Bartel, D.L., Bicknell, V.L. & Wright, T.M., 1986. The effect of conformity, thickness, and material on stresses in ultra-high molecular weight components for total joint replacement. *The Journal of bone and joint surgery. American volume*, 68(7), p.1041-51. Available at: http://www.ncbi.nlm.nih.gov/pubmed/3745241.

Bhushan, B., 2001. Surface Roughness Analysis and Measurement Techniques. In *Modern Tribology Handbook*. CRC Press.

Boontongkong, Y. et al., 1998. Orientation of plane strain-compressed ultra- high-molecular-weight polyethylene. *Polymer*, 39(25), p.6391-6400.

Bowsher, J.G. et al., 2008. Surface damage after multiple dislocations of a 38-mm-diameter, metal-on-metal hip prosthesis. *The Journal of arthroplasty*, 23(7), p.1090-6. Available at: http://www.ncbi.nlm.nih.gov/pubmed/18534503.

Bozic, K.J. et al., 2010. The epidemiology of revision total knee arthroplasty in the United States. *Clinical orthopaedics and related research*, 468(1), p.45-51. Available at: http://www.pubmedcentral.nih.gov/articlerender.fcgi?artid=2795838&tool=pmcentrez&rendertype=abstract [Accessed September 20, 2010].

Bradford, L. et al., 2004. Wear and surface cracking in early retrieved highly cross-linked polyethylene acetabular liners. *The Journal of bone and joint surgery. American volume*, 86-A(6), p.1271-82. Available at: http://www.ncbi.nlm.nih.gov/pubmed/15173302.

Bragdon, C.R. et al., 2001. A new pin-on-disk wear testing method for simulating wear of polyethylene on cobalt-chrome alloy in total hip arthroplasty. *The Journal of arthroplasty*, 16(5), p.658-65. Available at: http://www.ncbi.nlm.nih.gov/pubmed/11503127.

Bragdon, C.R. et al., 1996. The importance of multidirectional motion on the wear of polyethylene. *Proceedings of the Institution of Mechanical Engineers, Part H: Journal of Engineering in Medicine*, 210(3), p.157-65. Available at: http://www.ncbi.nlm.nih.gov/pubmed/8885652.

Brown, T.D. & Bartel, D.L., 2008. What design factors influence wear behavior at the bearing surfaces in total joint replacements? *The Journal of the American Academy of Orthopaedic Surgeons*, 16 Suppl 1, p.S101-6. Available at: http://www.ncbi.nlm.nih.gov/pubmed/18612003 [Accessed July 9, 2010].

Callister, W.D., 2003. *Material Science and Engineering, an Introduction* 6th ed., John Wiley & Sons, Inc.

Campbell, P. et al., 1995. Isolation of predominantly submicron-sized UHMWPE wear particles from periprosthetic tissues. *Journal of biomedical materials research*, 29(1), p.127-31. Available at: http://www.ncbi.nlm.nih.gov/pubmed/7713952.

Chang, C.B. et al., 2008. Transfer of metallic debris from the metal surface of an acetabular cup to artificial femoral heads by scraping: comparison between alumina and cobalt-chrome heads. *Journal of biomedical materials research. Part B, Applied biomaterials*, 85(1), p.204-9. Available at: http://www.ncbi.nlm.nih.gov/pubmed/17854069.

Citters, D.W. Van et al., 2004. A Multi-Station Rolling/Sliding Tribotester for Knee Bearing Materials. *Journal of Tribology*, 126(2), p.380. Available at: http://link.aip.org/link/JOTRE9/v126/i2/p380/s1&Agg=doi.

Citters, D.W. Van, 2006. *An Investigation Of The Microstructure, Mechanical Properties, And Tribological Performance Of Ultra High Molecular Weight Polyethylene For Applications In Total Joint Arthroplasty*. Dartmouth College.

Citters, D.W. Van, Kennedy, F.E. & Collier, J.P., 2007. Rolling sliding wear of UHMWPE for knee bearing applications. *Wear*, 263(7-12), p.1087-1094. Available at: http://linkinghub.elsevier.com/retrieve/pii/S0043164807003602.

Cornwall, G.B., Bryant, J.T. & Hansson, C.M., 2001. The effect of kinematic conditions on the wear of ultra-high molecular weight polyethylene (UHMWPE) in orthopaedic bearing applications. *Proceedings of the Institution of Mechanical Engineers. Part H, Journal of engineering in medicine*, 215(1), p.95-106. Available at: http://www.ncbi.nlm.nih.gov/pubmed/11323990.

Crane, D.J., 1998. *TEM Evaluation and Correlation of Morphological Evolution Induced From Aging, Fatigue, and Wear of UHMWPE*. University of California, Berkeley.

Currier, B.H. et al., 2007. In vivo oxidation of gamma-barrier-sterilized ultra-high-molecular-weight polyethylene bearings. *The Journal of arthroplasty*, 22(5), p.721-31. Available at: http://www.ncbi.nlm.nih.gov/pubmed/17689783 [Accessed September 14, 2010].

Currier, J.H. et al., 1998. In vitro simulation of contact fatigue damage found in ultra-high molecular weight polyethylene components of knee prostheses. *Proceedings of the Institution of Mechanical Engineers. Part H, Journal of engineering in medicine*, 212(4), p.293-302. Available at: http://link.aip.org/link/JOTRE9/v122/i1/p332/s1&Agg=doi [Accessed August 19, 2011].

Davey, S.M. et al., 2004. Measurement of Molecular Orientation in Retrieved Ultra-high-molecular-weight Polyethylene (UHMWPE) Hip Sockets using Fourier-transform Infrared Spectroscopy. *Strain*, 40(4), p.203-210. Available at: http://doi.wiley.com/10.1111/j.1475-1305.2004.00166.x.

Della Valle, A.G. et al., 2004. Wear of a highly cross-linked polyethylene liner associated with metallic deposition on a ceramic femoral head. *The Journal of arthroplasty*, 19(4), p.532-6. Available at: http://www.ncbi.nlm.nih.gov/pubmed/15188120 [Accessed August 4, 2010].

Dowson, D., Taheri, S. & Wallbridge, N., 1987. The role of counterface imperfections in the wear of polyethylene. *Wear*, 119(3), p.277-293. Available at: http://linkinghub.elsevier.com/retrieve/pii/0043164887900366.

Dressler, M.R. et al., 2011. Predicting Wear of UHMWPE: Decreasing Wear Rate Following a Change in Direction. *Wear*, 271(11-12), p.2879-2883. Available at: http://linkinghub.elsevier.com/retrieve/pii/S0043164811004467 [Accessed September 22, 2011].

Edidin, A.A. et al., 1999. Plasticity-induced damage layer is a precursor to wear in radiation-cross-linked UHMWPE acetabular components for total hip replacement. *The Journal of Arthroplasty*, 14(5), p.616-627. Available at: http://linkinghub.elsevier.com/retrieve/pii/S0883540399900864.

Elfick, A.P.D. et al., 2000. A novel technique for the detailed size characterization of wear debris. *Journal of materials science. Materials in medicine*, 11(5), p.267-71. Available at: http://www.ncbi.nlm.nih.gov/pubmed/15348022 [Accessed May 2, 2012].

Elfick, A.P.D. et al., 2001. The quantitative assessment of UHMWPE wear debris produced in hip simulator testing: the influence of head material and roughness, motion and loading. *Wear*, 249(5-6), p.517-527. Available at: http://linkinghub.elsevier.com/retrieve/pii/S0043164801005890 [Accessed May 2, 2012].

Fisher, J. et al., 1995. The influence of scratches to metallic counterfaces on the wear of ultra-high molecular weight polyethylene. *Proceedings of the Institution of Mechanical Engineers, Part H: Journal of Engineering in Medicine*, 209(48), p.263-264. Available at:

http://archive.pepublishing.com/openurl.asp?genre=article&id=doi:10.1243/PIME_PROC_1995_209_353_02.

Furmanski, J. et al., 2009. Clinical fracture of cross-linked UHMWPE acetabular liners. *Biomaterials*, 30(29), p.5572-82. Available at: http://www.ncbi.nlm.nih.gov/pubmed/19643471.

Galeski, A. et al., 1992. Morphological alterations during texture-producing plastic plane strain compression of high-density polyethylene. *Macromolecules*, 25(21), p.5705-5718. Available at: http://pubs.acs.org/doi/abs/10.1021/ma00047a023.

Galvin, A.L. et al., 2009. Effect of conformity and contact stress on wear in fixed-bearing total knee prostheses. *Journal of biomechanics*, 42(12), p.1898-902. Available at: http://www.ncbi.nlm.nih.gov/pubmed/19524245.

Galvin, A.L. et al., 2006. Wear of crosslinked polyethylene under different tribological conditions. *Journal of materials science: Materials in medicine*, 17(3), p.235-43. Available at: http://www.ncbi.nlm.nih.gov/pubmed/16555115.

Geary, C., Birkinshaw, C. & Jones, E., 2008. Characterisation of Bionate polycarbonate polyurethanes for orthopaedic applications. *Journal of materials science. Materials in medicine*, 19(11), p.3355-63. Available at: http://www.springerlink.com/content/4286r776t2l1675x/ [Accessed March 4, 2012].

Gevaert, M.R. et al., 2005. The Quantification of Physiologically Relevant Cross-Shear Wear Phenomena on Orthopaedic Bearing Materials Using the MAX-Shear Wear Testing System. *Journal of Tribology*, 127(4), p.740. Available at: http://link.aip.org/link/JOTRE9/v127/i4/p740/s1&Agg=doi.

Goodfellow, J. & O'Connor, J., 1978. The mechanics of the knee and prosthesis design. *The Journal of bone and joint surgery. British volume*, 60-B(3), p.358-69. Available at: http://www.ncbi.nlm.nih.gov/pubmed/581081.

Grimm, B., Tonino, A.J. & Heyligers, I.C., 2012. 14yrs Long-term Performance of Crosslinked PE: Sustained Wear Reduction and less Osteolysis ? In *Orthopaedic Research Society Annual Meeting*. San Francisco, CA, USA, p. Paper No. 0314.

Gupta, S.K. et al., 2007. Osteolysis after total knee arthroplasty. *The Journal of arthroplasty*, 22(6), p.787-99. Available at: http://www.ncbi.nlm.nih.gov/pubmed/17826267 [Accessed September 14, 2010].

Hall, R.M. et al., 1997. The effect of surface topography of retrieved femoral heads on the wear of UHMWPE sockets. *Medical engineering & physics*, 19(8), p.711-9. Available at: http://www.ncbi.nlm.nih.gov/pubmed/9450255.

Hall, R.M. et al., 1996. The surface topography of retrieved femoral heads. *Journal of Materials Science: Materials in Medicine*, 7(12), p.739-744. Available at: http://www.springerlink.com/index/10.1007/BF00121409.

Hamilton, M.A. et al., 2005. Quantifying Multidirectional Sliding Motions in Total Knee Replacements. *Journal of Tribology*, 127(2), p.280. Available at: http://link.aip.org/link/JOTRE9/v127/i2/p280/s1&Agg=doi.

International Standards Organization, 2004. *ISO 14243-3, Implants For Surgery - Wear of total knee-joint prostheses - Part 3: Loading and displacement parameters for wear-testing machines with displacement control and corresponding environmental conditions for test*,

Ito, H. et al., 2010. In vivo femoral head damage and its effect on polyethylene wear. *The Journal of arthroplasty*, 25(2), p.302-8. Available at: http://www.ncbi.nlm.nih.gov/pubmed/19201153 [Accessed April 27, 2012].

Jacobs, C.A. et al., 2007. Clinical performance of highly cross-linked polyethylenes in total hip arthroplasty. *The Journal of bone and joint surgery. American volume*, 89(12), p.2779-86. Available at: http://www.ncbi.nlm.nih.gov/pubmed/18056513.

Jaffe, W.L. et al., 2009. Surface oxidized zirconium total hip arthroplasty head damage due to closed reduction effects on polyethylene wear. *The Journal of arthroplasty*, 24(6), p.898-902. Available at: http://www.ncbi.nlm.nih.gov/pubmed/18848427.

Jasty, M., Rubash, H.E. & Muratoglu, O.K., 2005. Highly cross-linked polyethylene: the debate is over--in the affirmative. *The Journal of arthroplasty*, 20(4 Suppl 2), p.55-8. Available at: http://www.ncbi.nlm.nih.gov/pubmed/15991131 [Accessed September 2, 2010].

Jiang, X.Q., Blunt, L. & Stout, K.J., 1999. Three-dimensional surface characterization for orthopaedic joint prostheses. *Proceedings of the Institution of Mechanical Engineers, Part H: Journal of Engineering in Medicine*, 213(1), p.49-68. Available at: http://www.ncbi.nlm.nih.gov/pubmed/10087904.

Jin, Z.M., Fisher, J. & Ingham, E., 2006. Biotribology: Material Design, Lubrication, and Wear in Artificial Hip Joints. In G. E. Totten, ed. *Handbook of Lubrication and Tribology: Volume I, Application and Maintenance*. CRC Press 2006.

Kang, L., Galvin, A.L., Brown, T.D., Jin, Z.M., et al., 2008. Quantification of the effect of cross-shear on the wear of conventional and highly cross-linked UHMWPE. *Journal of biomechanics*, 41(2), p.340-6. Available at: http://www.ncbi.nlm.nih.gov/pubmed/17936763.

Kang, L., Galvin, A.L., Brown, T.D., Fisher, J., et al., 2008. Wear simulation of ultra-high molecular weight polyethylene hip implants by incorporating the effects of cross-shear and contact pressure. *Proceedings of the Institution of Mechanical Engineers, Part H: Journal of Engineering in Medicine*, 222(7), p.1049-1064. Available at:

http://journals.pepublishing.com/openurl.asp?genre=article&id=doi:10.1243/09544119JEIM431.

Kato, K. & Adachi, K., 2001. Wear Mechanisms. In B. Bhushan, ed. *Modern Tribology Handbook*. CRC Press. Available at: http://www.crcnetbase.com/isbn/978-0-8493-8403-5.

Kennedy, F.E. et al., 2007. Lubrication and Wear of Artificial Knee Joint Materials in a Rolling⁄Sliding Tribotester. *Journal of Tribology*, 129(2), p.326. Available at: http://link.aip.org/link/JOTRE9/v129/i2/p326/s1&Agg=doi.

Kennedy, F.E. et al., 2003. Oxidation of Ultra-High Molecular Weight Polyethylene and Its Influence on Contact Fatigue and Pitting of Knee Bearings. *Tribology Transactions*, 46(1), p.111-118. Available at: http://www.informaworld.com/openurl?genre=article&doi=10.1080/10402000308982607&magic=crossref||D404A21C5BB053405B1A640AFFD44AE3.

Khan, I. et al., 2005. Analysis and evaluation of a biomedical polycarbonate urethane tested in an in vitro study and an ovine arthroplasty model. Part II: in vivo investigation. *Biomaterials*, 26(6), p.633-43. Available at: http://www.ncbi.nlm.nih.gov/pubmed/15282141 [Accessed March 4, 2012].

Kilgour, A. & Elfick, A.P.D., 2009. Influence of crosslinked polyethylene structure on wear of joint replacements. *Tribology International*, 42(11-12), p.1582-1594. Available at: http://linkinghub.elsevier.com/retrieve/pii/S0301679X08002533.

Kim, Y.-H., Ritchie, A. & Hardaker, C., 2005. Surface roughness of ceramic femoral heads after in vivo transfer of metal: correlation to polyethylene wear. *The Journal of bone and joint surgery. American volume*, 87(3), p.577-82. Available at: http://www.ncbi.nlm.nih.gov/pubmed/15741625.

Klapperich, C.M., Komvopoulos, K. & Pruitt, L.A., 1999. Tribological properties and microstructure evolution of ultra-high molecular weight polyethylene. *Journal of Tribology*, 121(April), p.394. Available at: http://link.aip.org/link/?JOTRE9/121/394/1.

Kop, A.M., Whitewood, C. & Johnston, D.J.L., 2007. Damage of oxinium femoral heads subsequent to hip arthroplasty dislocation three retrieval case studies. *The Journal of arthroplasty*, 22(5), p.775-9. Available at: http://www.ncbi.nlm.nih.gov/pubmed/17689792.

Kurtz, S.M. et al., 1999. Advances in the processing, sterilization, and crosslinking of ultra-high molecular weight polyethylene for total joint arthroplasty. *Biomaterials*, 20(18), p.1659-88. Available at: http://www.ncbi.nlm.nih.gov/pubmed/10503968.

Kurtz, S.M., Ong, K.L., Schmier, J., et al., 2007. Future clinical and economic impact of revision total hip and knee arthroplasty. *The Journal of bone and joint surgery. American volume*, 89 Suppl 3, p.144-51. Available at: http://www.ncbi.nlm.nih.gov/pubmed/17908880.

Kurtz, S.M. et al., 2012. Material Performance and Reasons for Revision of 1st and 2nd Generation Highly Crosslinked Polyethylenes Used in Total Hip Arthroplasty. In *Orthopaedic Research Society Annual Meeting*. San Francisco, CA, USA, p. Poster No. 2024.

Kurtz, S.M., Ong, K.L., Lau, E., et al., 2007. Projections of primary and revision hip and knee arthroplasty in the United States from 2005 to 2030. *The Journal of bone and joint surgery. American volume*, 89(4), p.780-5. Available at: http://www.ncbi.nlm.nih.gov/pubmed/17403800.

Kurtz, S.M. et al., 2000. The relationship between the clinical performance and large deformation mechanical behavior of retrieved UHMWPE tibial inserts. *Biomaterials*, 21(3), p.283-91. Available at: http://www.ncbi.nlm.nih.gov/pubmed/10646945.

Kurtz, S.M., 2009. *UHMWPE Biomaterials Handbook* 2nd ed. S. M. Kurtz, ed., Academic Press.

Lachiewicz, P.F. & Geyer, M.R., 2011. The use of highly cross-linked polyethylene in total knee arthroplasty. *The Journal of the American Academy of Orthopaedic Surgeons*, 19(3), p.143-51. Available at: http://apps.webofknowledge.com/full_record.do?product=UA&search_mode=GeneralSearch&qid=12&SID=X2lOng2NLCBnGjGDJgK&page=2&doc=67 [Accessed August 19, 2011].

Lancaster, J.K., 1969. Abrasive Wear of Polymers. *Wear*, 14, p.223-239.

Lin, L. & Argon, A.S., 1994. Structure and plastic deformation of polyethylene. *Journal of Materials Science*, 29(2), p.294-323. Available at: http://www.springerlink.com/index/10.1007/BF01162485.

Liu, F. et al., 2011. A new formulation for the prediction of polyethylene wear in artificial hip joints. *Proceedings of the Institution of Mechanical Engineers, Part H: Journal of Engineering in Medicine*, 225(1), p.16-24. Available at: http://journals.pepublishing.com/openurl.asp?genre=article&id=doi:10.1243/09544119JEIM819 [Accessed August 18, 2011].

Luchetti, W.T. et al., 1998. Drain entrapment and titanium to ceramic head deposition: two unique complications following closed reduction of a dislocated total hip arthroplasty. *The Journal of arthroplasty*, 13(6), p.713-7. Available at: http://www.ncbi.nlm.nih.gov/pubmed/9741451.

MacDonald, D.W. et al., 2012. Material and Clinical Performance of Remelted Highly Crosslinked Polyethylene Used in Total Knee Arthroplasty. In *Orthopaedic Research Society Annual Meeting*. San Francisco, CA, USA, p. Poster No. 1999.

Mavraki, a & Cann, P M, 2009. Friction and lubricant film thickness measurements on simulated synovial fluids. *Proceedings of the Institution of Mechanical Engineers, Part J: Journal of*

Engineering Tribology, 223(3), p.325-335. Available at: http://pij.sagepub.com/lookup/doi/10.1243/13506501JET580 [Accessed April 25, 2012].

Mavraki, a. & Cann, P.M., 2011. Lubricating film thickness measurements with bovine serum. *Tribology International*, 44(5), p.550-556. Available at: http://linkinghub.elsevier.com/retrieve/pii/S0301679X10001775 [Accessed April 18, 2012].

Mazzucco, D. & Spector, M., 2003. Effects of contact area and stress on the volumetric wear of ultrahigh molecular weight polyethylene. *Wear*, 254, p.514-522. Available at: http://linkinghub.elsevier.com/retrieve/pii/S0043164803001352.

McEwen, H.M.J. et al., 2005. The influence of design, materials and kinematics on the in vitro wear of total knee replacements. *Journal of biomechanics*, 38(2), p.357-65. Available at: http://www.ncbi.nlm.nih.gov/pubmed/15598464.

McGloughlin, T.M. & Kavanagh, A.G., 1998. The influence of slip ratios in contemporary TKR on the wear of ultra-high molecular weight polyethylene (UHMWPE): An experimental review. *Journal of Biomechanics*, 31(S1), p.8.

McKellop, H.A., Shen, F.W., et al., 1999. Development of an extremely wear-resistant ultra high molecular weight polyethylene for total hip replacements. *Journal of orthopaedic research : official publication of the Orthopaedic Research Society*, 17(2), p.157-67. Available at: http://www.ncbi.nlm.nih.gov/pubmed/10221831.

McKellop, H.A., 2007. The lexicon of polyethylene wear in artificial joints. *Biomaterials*, 28(34), p.5049-57. Available at: http://www.ncbi.nlm.nih.gov/pubmed/17706766.

McKellop, H.A., Shen, F.-W., et al., 1999. Wear of gamma-crosslinked polyethylene acetabular cups against roughened femoral balls. *Clinical orthopaedics and related research*, (369), p.73-82. Available at: http://www.ncbi.nlm.nih.gov/pubmed/10611862.

McNie, C.M. et al., 2000. The prediction of polyethylene wear rate and debris morphology produced by microscopic asperities on femoral heads. *Journal of materials science: Materials in medicine*, 11(3), p.163-74. Available at: http://www.ncbi.nlm.nih.gov/pubmed/15348045.

Michael Doerner, BA, U.S. et al., 2012. Multi-Center Minimum Five-year Wear Analysis of Large Femoral Heads on Highly-Crosslinked Polyethylene. In *American Academy of Orthopaedic Surgeons*. San Francisco, p. #358. Available at: http://www.abstractsonline.com/Plan/ViewAbstract.aspx?mID=2841&sKey=6e892f4d-3762-4b7d-8a3e-38fe6b530009&cKey=25eb6dc5-a9cf-4164-a1bc-16d1ffd6a048&mKey=BA8AA154-A9B9-41F9-91A7-F4A4CB050945 [Accessed March 19, 2012].

Morra, E.A. & Greenwald, A.S., 2005. Polymer insert stress in total knee designs during high-flexion activities: a finite element study. *The Journal of bone and joint surgery. American volume*, 87 Suppl 2, p.120-4. Available at: http://www.ncbi.nlm.nih.gov/pubmed/16326731.

Muratoglu, O.K., Bragdon, C.R., O'Connor, D.O., Jasty, M., et al., 2001. A novel method of cross-linking ultra-high-molecular-weight polyethylene to improve wear, reduce oxidation, and retain mechanical properties. Recipient of the 1999 HAP Paul Award. *The Journal of arthroplasty*, 16(2), p.149-60. Available at: http://www.ncbi.nlm.nih.gov/pubmed/11222887.

Muratoglu, O.K., Merrill, E.W., et al., 2003. Effect of radiation, heat, and aging on in vitro wear resistance of polyethylene. *Clinical orthopaedics and related research*, (417), p.253-62. Available at: http://www.ncbi.nlm.nih.gov/pubmed/14646724 [Accessed July 2, 2010].

Muratoglu, O.K., Burroughs, B.R., et al., 2004. Knee Simulator Wear of Polyethylene Tibias Articulating against Explanted Rough Femoral Components. *Clinical Orthopaedics and Related Research*, 428(428), p.108-113. Available at: http://content.wkhealth.com/linkback/openurl?sid=WKPTLP:landingpage&an=00003086-200411000-00018.

Muratoglu, O.K., Bragdon, C.R., O'Connor, D.O., Perinchief, R.S., et al., 2001. Larger diameter femoral heads used in conjunction with a highly cross-linked ultra-high molecular weight polyethylene: A new concept. *The Journal of Arthroplasty*, 16(8), p.24-30. Available at: http://linkinghub.elsevier.com/retrieve/pii/S0883540301414811 [Accessed July 14, 2010].

Muratoglu, O.K. et al., 2003. Optical analysis of surface changes on early retrievals of highly cross-linked and conventional polyethylene tibial inserts. *The Journal of arthroplasty*, 18(7 Suppl 1), p.42-7. Available at: http://www.ncbi.nlm.nih.gov/pubmed/14560410.

Muratoglu, O.K., Mark, A., Vittetoe, D.A., et al., 2003. Polyethylene damage in total knees and use of highly crosslinked polyethylene. *The Journal of bone and joint surgery. American volume*, 85-A Suppl, p.S7-S13. Available at: http://www.ncbi.nlm.nih.gov/pubmed/12540663.

Muratoglu, O.K., Greenbaum, E.S., et al., 2004. Surface analysis of early retrieved acetabular polyethylene liners: a comparison of conventional and highly crosslinked polyethylenes. *The Journal of Arthroplasty*, 19(1), p.68-77. Available at: http://linkinghub.elsevier.com/retrieve/pii/S0883540303005011.

Muratoglu, O.K. et al., 1999. Unified wear model for highly crosslinked ultra-high molecular weight polyethylenes (UHMWPE). *Biomaterials*, 20(16), p.1463-70. Available at: http://www.ncbi.nlm.nih.gov/pubmed/10458559.

Myant, C., Spikes, H. a. & Stokes, J.R., 2010. Influence of load and elastic properties on the rolling and sliding friction of lubricated compliant contacts. *Tribology International*, 43(1-

2), p.55-63. Available at: http://linkinghub.elsevier.com/retrieve/pii/S0301679X09001145 [Accessed April 27, 2012].

Myant, Connor, Fowell, M., et al., 2010. An Investigation of Lubricant Film Thickness in Sliding Compliant Contacts. *Tribology Transactions*, 53(5), p.684-694. Available at: http://www.tandfonline.com/doi/abs/10.1080/10402001003693109 [Accessed April 27, 2012].

Neu, C.P., Komvopoulos, K. & Reddi, A.H., 2008. The interface of functional biotribology and regenerative medicine in synovial joints. *Tissue engineering. Part B, Reviews*, 14(3), p.235-47. Available at: http://www.pubmedcentral.nih.gov/articlerender.fcgi?artid=2761828&tool=pmcentrez&rendertype=abstract [Accessed September 1, 2010].

Oleinik, E.F., 2003. Plasticity of semicrystalline flexible-chain polymers at the microscopic and mesoscopic levels. *POLYMER SCIENCE SERIES C*, 45, p.17-117. Available at: http://cat.inist.fr/?aModele=afficheN&cpsidt=16203252 [Accessed March 14, 2012].

Olley, R.H. & Bassett, D.C., 1982. An improved permanganic etchant for polyolefines. *Polymer*, 23(12), p.1707-1710. Available at: http://linkinghub.elsevier.com/retrieve/pii/0032386182901100 [Accessed April 24, 2012].

Olley, R.H., Hodge, a. M. & Bassett, D.C., 1979. A permanganic etchant for polyolefines. *Journal of Polymer Science: Polymer Physics Edition*, 17(4), p.627-643. Available at: http://doi.wiley.com/10.1002/pol.1979.180170406 [Accessed April 24, 2012].

Omar, M.K., Atkins, A.G. & Lancaster, J.K., 1986. The role of crack resistance parameters in polymer wear. *Journal of Physics D: Applied Physics*, 19(2), p.177-196. Available at: http://iopscience.iop.org/0022-3727/19/2/007 [Accessed September 23, 2010].

Omori, G. et al., 2009. The effect of geometry of the tibial polyethylene insert on the tibiofemoral contact kinematics in Advance Medial Pivot total knee arthroplasty. *Journal of orthopaedic science : official journal of the Japanese Orthopaedic Association*, 14(6), p.754-60. Available at: http://www.ncbi.nlm.nih.gov/pubmed/19997823 [Accessed September 23, 2010].

Oñate, J.I. et al., 2001. Wear reduction effect on ultra-high-molecular-weight polyethylene by application of hard coatings and ion implantation on cobalt chromium alloy, as measured in a knee wear simulation machine. *Surface and Coatings Technology*, 142-144, p.1056-1062. Available at: http://linkinghub.elsevier.com/retrieve/pii/S025789720101074X [Accessed August 19, 2011].

Patten, E.W. et al., 2010. Delamination of a highly cross-linked polyethylene liner associated with titanium deposits on the cobalt-chromium modular femoral head following dislocation. *The Journal of bone and joint surgery. British volume*, 92(9), p.1306-11. Available at: http://www.ncbi.nlm.nih.gov/pubmed/20798454 [Accessed September 2, 2010].

Patten, E.W., 2008. *Multi-Axial Tribo-System: Rolling, Sliding, and Rotation of UHMWPE in Total Joint Replacements*. University of California, Berkeley.

Petrella, A.J. et al., 2011. A novel cross-shear metric for application in computer simulation of ultra-high molecular weight polyethylene wear. *Computer methods in biomechanics and biomedical engineering*, (February 2012), p.37-41. Available at: http://www.ncbi.nlm.nih.gov/pubmed/22136186 [Accessed February 6, 2012].

Postak, P.D., Heim, C.S. & Greenwald, A.S., 1998. TIBIAL PLATEAU SURFACE STRESS IN TKA: A FACTOR INFLUENCING POLYMER DAMAGE Series VI. In *American Academy of Orthopaedic Surgeons*.

Premnath, V. et al., 1996. Gamma sterilization of UHMWPE articular implants: an analysis of the oxidation problem. Ultra High Molecular Weight Poly Ethylene. *Biomaterials*, 17(18), p.1741-53. Available at: http://www.ncbi.nlm.nih.gov/pubmed/8879511.

Pruitt, L.A., 2005. Deformation, yielding, fracture and fatigue behavior of conventional and highly cross-linked ultra high molecular weight polyethylene. *Biomaterials*, 26(8), p.905-15. Available at: http://www.ncbi.nlm.nih.gov/pubmed/15353202.

Pruitt, L.A. & Chakravartula, A., 2011. *Mechanics of Biomaterials: Fundamental Principles for Implant Design*, Cambridge: Cambridge University Press.

Que, L. & Topoleski, L.D., 1999. Surface roughness quantification of CoCrMo implant alloys. *Journal of biomedical materials research*, 48(5), p.705-11. Available at: http://www.ncbi.nlm.nih.gov/pubmed/10490686.

Reinholz, A. et al., 1998. Analysis of the coefficient of friction as a function of the slide/roll ratio in total knee replacement. *Journal of Biomechanics*, 31(S1), p.8.

Ries, M.D., 2005. Highly cross-linked polyethylene: the debate is over--in opposition. *The Journal of arthroplasty*, 20(4 Suppl 2), p.59-62. Available at: http://www.ncbi.nlm.nih.gov/pubmed/15991132 [Accessed September 2, 2010].

Ries, M.D. & Pruitt, L.A., 2005. Effect of Cross-linking on the Microstructure and Mechanical Properties of Ultra-High Molecular Weight Polyethylene. *Clinical Orthopaedics and Related Research*, 440(&NA;), p.149-156. Available at: http://content.wkhealth.com/linkback/openurl?sid=WKPTLP:landingpage&an=00003086-200511000-00027.

Rose, R. et al., 1982. Exploratory investigations on the structure dependence of the wear resistance of polyethylene. *Wear*, 77(1), p.89-104. Available at: http://linkinghub.elsevier.com/retrieve/pii/0043164882900485.

Rostoker, W. & Galante, J.O., 1979. Contact pressure dependence of wear rates of ultra high molecular weight polyethylene. *Journal of biomedical materials research*, 13(6), p.957-64. Available at: http://www.ncbi.nlm.nih.gov/pubmed/511863.

Saikko, V.O., 1998. A multidirectional motion pin-on-disk wear test method for prosthetic joint materials. *Journal of biomedical materials research*, 41(1), p.58-64. Available at: http://www.ncbi.nlm.nih.gov/pubmed/9641624.

Saikko, V.O., 2006. Effect of contact pressure on wear and friction of ultra-high molecular weight polyethylene in multidirectional sliding. *Proceedings of the Institution of Mechanical Engineers, Part H: Journal of Engineering in Medicine*, 220(7), p.723-731. Available at: http://journals.pepublishing.com/openurl.asp?genre=article&id=doi:10.1243/09544119JEIM146.

Saikko, V.O. & Ahlroos, T., 2000. Wear simulation of UHMWPE for total hip replacement with a multidirectional motion pin-on-disk device: effects of counterface material, contact area, and lubricant. *Journal of biomedical materials research*, 49(2), p.147-54. Available at: http://www.ncbi.nlm.nih.gov/pubmed/10571900.

Saikko, V.O., Ahlroos, T. & Calonius, O., 2001. A three-axis knee wear simulator with ball-on-flat contact. *Wear*, 249(3-4), p.310-315. Available at: http://linkinghub.elsevier.com/retrieve/pii/S0043164801005671.

Saikko, V.O. & Calonius, O., 2002. Simulation of wear rates and mechanisms in total knee prostheses by ball-on-flat contact in a five-station, three-axis test rig. *Wear*, 253(3-4), p.424-429. Available at: http://linkinghub.elsevier.com/retrieve/pii/S0043164802001540.

Saikko, V.O., Calonius, O. & Keränen, J., 2002. Wear of conventional and cross-linked ultra-high-molecular-weight polyethylene acetabular cups against polished and roughened CoCr femoral heads in a biaxial hip simulator. *Journal of biomedical materials research*, 63(6), p.848-53. Available at: http://www.ncbi.nlm.nih.gov/pubmed/12418033.

Salineros, M.J. et al., 2007. Analysis of retrieved acetabular components of three polyethylene types. *Clinical orthopaedics and related research*, 465(465), p.140-9. Available at: http://www.ncbi.nlm.nih.gov/pubmed/17632415.

Sambasivan, S. et al., 2004. Molecular orientation of ultrahigh molecular weight polyethylene induced by various sliding motions. *Journal of biomedical materials research. Part B, Applied biomaterials*, 70(2), p.278-85. Available at: http://www.ncbi.nlm.nih.gov/pubmed/15264310 [Accessed July 26, 2010].

Sawyer, W.G. et al., 2003. Analysis of in vivo crossing mtotion in total knee replacements. In *2003 Summer Bioengineering Conference*. Key Biscayne, Florida, p. 0549.

Schuh, A. et al., 2006. Severe damage of the femoral head after dislocation and difficult reduction maneuvers after total hip arthroplasty. *Archives of orthopaedic and trauma surgery*, 126(2), p.134-7. Available at: http://www.ncbi.nlm.nih.gov/pubmed/16402198.

Schwenke, T. et al., 2008. Experimental Determination of Cross-Shear Dependency in Polyethylene Wear. In *54th Annual Meeting of the Orthopaedic Research Society*. San Francisco, CA, USA, p. Poster No . 1890.

Schwenke, T. et al., 2005. The influence of slip velocity on wear of total knee arthroplasty. *Wear*, 259(7-12), p.926-932. Available at: http://linkinghub.elsevier.com/retrieve/pii/S0043164805001018.

Shadrake, L.G. & Guiu, F., 1979. Elastic line energies and line tensions of dislocations in polyethylene crystals. , (March 2012), p.37-41.

Sherrington, I., 1998. Tribology: Surface Topography. In E. H. Smith, ed. *Mechanical Engineer's Reference Book*. Elsevier. Available at: http://www.knovel.com/web/portal/basic_search/display?_EXT_KNOVEL_DISPLAY_bookid=676.

Strickland, M.A., Dressler, M.R. & Taylor, M., 2012. Predicting implant UHMWPE wear in-silico: A robust, adaptable computational–numerical framework for future theoretical models. *Wear*, 274-275, p.100-108. Available at: http://linkinghub.elsevier.com/retrieve/pii/S0043164811005643 [Accessed February 18, 2012].

Suh, N.P., 1977. An overview of the delamination theory of wear. *Wear*, 44(1), p.1–16. Available at: http://linkinghub.elsevier.com/retrieve/pii/0043164877900813 [Accessed September 17, 2010].

Suh, N.P., 1973. The delamination theory of wear. *Wear*, 25(1), p.111-124. Available at: http://linkinghub.elsevier.com/retrieve/pii/0043164873901257.

Séguéla, R., 2002. Dislocation approach to the plastic deformation of semicrystalline polymers: Kinetic aspects for polyethylene and polypropylene. *Journal of Polymer Science Part B: Polymer Physics*, 40(6), p.593-601. Available at: http://doi.wiley.com/10.1002/polb.10118 [Accessed March 14, 2012].

Turell, M., Wang, A. & Bellare, Anuj, 2003. Quantification of the effect of cross-path motion on the wear rate of ultra-high molecular weight polyethylene. *Wear*, 255(7-12), p.1034-1039. Available at: http://linkinghub.elsevier.com/retrieve/pii/S0043164803003570 [Accessed October 13, 2011].

Vassiliou, K. & Unsworth, A., 2004. Is the wear factor in total joint replacements dependent on the nominal contact stress in ultra-high molecular weight polyethylene contacts?

Proceedings of the Institution of Mechanical Engineers. Part H, Journal of engineering in medicine, 218(2), p.101-7. Available at: http://www.ncbi.nlm.nih.gov/pubmed/15116897.

Verioti, C. et al., 2009. Surface Roughness of Femoral Head Prostheses After Dislocation. In *2009 Annual Meeting of the American Academy of Orthopaedic Surgeons*. Las Vegas, NV, USA, p. P001. Available at: http://www3.aaos.org/education/anmeet/anmt2009/poster/poster.cfm?Pevent=P001 [Accessed August 4, 2010].

Walker, P.S., Blunn, G.W. & Lilley, P.A., 1996. Wear testing of materials and surfaces for total knee replacement. *Journal of biomedical materials research*, 33(3), p.159-75. Available at: http://www.ncbi.nlm.nih.gov/pubmed/8864888.

Wang, A., 2001. A unified theory of wear for ultra-high molecular weight polyethylene in multi-directional sliding. *Wear*, 248(1-2), p.38-47. Available at: http://linkinghub.elsevier.com/retrieve/pii/S0043164800005226.

Wang, A. et al., 1998. Lubrication and wear of ultra-high molecular weight polyethylene in total joint replacements. *Tribology International*, 31(1-3), p.17-33. Available at: http://linkinghub.elsevier.com/retrieve/pii/S0301679X9800005X.

Wang, A., Sun, D.C., et al., 1997. Orientation softening in the deformation and wear of ultra-high molecular weight polyethylene. *Wear*, 203-204, p.230-241. Available at: http://linkinghub.elsevier.com/retrieve/pii/S0043164896073620.

Wang, A., Polineni, V.K., et al., 1997. The Significance of Nonlinear Motion in the Wear Screening of Orthopaedic Implant Materials. *Journal of Testing and Evaluation*, 25(2), p.239. Available at: http://www.astm.org/DIGITAL_LIBRARY/JOURNALS/TESTEVAL/PAGES/JTE11485J.htm.

Wang, A., Sun, D.C., et al., 1995. Wear mechanisms of UHMWPE in total joint replacements. *Wear*, 181-183(1), p.241-249. Available at: http://linkinghub.elsevier.com/retrieve/pii/0043164895900306.

Wang, A., Essner, A.P. & Klein, R., 2001. Effect of contact stress on friction and wear of ultra-high molecular weight polyethylene in total hip replacement. *Proceedings of the Institution of Mechanical Engineers, Part H: Journal of Engineering in Medicine*, 215(2), p.133-9. Available at: http://www.ncbi.nlm.nih.gov/pubmed/11382072.

Wang, A., Stark, C. & Dumbleton, J.H., 1995. Role of cyclic plastic deformation in the wear of UHMWPE acetabular cups. *Journal of biomedical materials research*, 29(5), p.619-26. Available at: http://www.ncbi.nlm.nih.gov/pubmed/7622547.

Williams, P.A. et al., 2007. Highly Crosslinked Polyethylenes in Hip Replacements: Improved Wear Performance or Paradox? *Tribology Transactions*, 50(2), p.277-290. Available at:

http://www.informaworld.com/openurl?genre=article&doi=10.1080/10402000701325204&magic=crossref||D404A21C5BB053405B1A640AFFD44AE3.

Willing, R.T. & Kim, I.Y., 2009a. A holistic numerical model to predict strain hardening and damage of UHMWPE under multiple total knee replacement kinematics and experimental validation. *Journal of biomechanics*, 42(15), p.2520-7. Available at: http://www.ncbi.nlm.nih.gov/pubmed/19647828 [Accessed October 18, 2011].

Willing, R.T. & Kim, I.Y., 2011. Design optimization of a total knee replacement for improved constraint and flexion kinematics. *Journal of biomechanics*, 44(6), p.1014-20. Available at: http://www.ncbi.nlm.nih.gov/pubmed/21367425 [Accessed August 18, 2011].

Willing, R.T. & Kim, I.Y., 2009b. Three dimensional shape optimization of total knee replacements for reduced wear. *Structural and Multidisciplinary Optimization*, 38(4), p.405-414. Available at: http://www.springerlink.com/index/10.1007/s00158-008-0281-0 [Accessed October 18, 2011].

Woo, S.L.-y et al., 1999. Biomechanics of Knee Ligaments. *The American Journal of Sports Medicine*, 27(4), p.533-543.

Yim, C.I. et al., 1999. Wear resistance of some modified ultra-high molecular weight polyethylenes and its correlation with tensile properties. *Polymer Bulletin*, 42(4), p.433-440. Available at: http://www.springerlink.com/openurl.asp?genre=article&id=doi:10.1007/s002890050486 [Accessed September 15, 2010].

Yoo, J.J., Kim, H.J. & Kim, Y.-M., 2004. Damage of an alumina-on-alumina bearing surface from a difficult reduction of a total hip arthroplasty. A report of three cases. *The Journal of bone and joint surgery. American volume*, 86-A(2), p.376-8. Available at: http://www.ncbi.nlm.nih.gov/pubmed/14960686.

Zhou, J. et al., 2004. Tribological and Nanomechanical Properties of Unmodified and Crosslinked Ultra-High Molecular Weight Polyethylene for Total Joint Replacements. *Journal of Tribology*, 126(2), p.386. Available at: http://link.aip.org/link/JOTRE9/v126/i2/p386/s1&Agg=doi.

Zhou, J. & Komvopoulos, K., 2005. Wear Mechanisms of Untreated and Gamma Irradiated Ultra-High Molecular Weight Polyethylene for Total Joint Replacements. *Journal of Tribology*, 127(2), p.273. Available at: http://link.aip.org/link/JOTRE9/v127/i2/p273/s1&Agg=doi.

eOrthopod, 2003. Artificial Joint Replacement of the Knee. Available at: http://www.eorthopod.com/content/revision-arthroplasty-knee [Accessed October 5, 2011].